ÇUKUROVA UNIVERSITY
INSTITUTE OF NATURAL AND APPLIED SCIENCES

PhD THESIS

Harun ZONTUL

INVESTIGATION OF HEAT TRANSFER IN CORRUGATED CHANNEL WITH PULSATING FLOW

DEPARTMENT OF MECHANICAL ENGINEERING

ADANA-2021

ÇUKUROVA UNIVERSITY
INSTITUTE OF NATURAL AND APPLIED SCIENCES

INVESTIGATION OF HEAT TRANSFER IN CORRUGATED CHANNEL WITH PULSATING FLOW

Harun ZONTUL

PhD THESIS

DEPARTMENT OF MECHANICAL ENGINEERING

We certify that the thesis titled above was reviewed and approved for the award of the degree of the Philosophy of Doctorate by the board of jury on 07/09/2021.

………………………	…………………………	………………………….
Prof. Dr. Beşir ŞAHİN	Prof. Dr. Hüseyin AKILLI	Prof. Dr. Mehmet BİLGİLİ
SUPERVISOR	MEMBER	MEMBER
………………………….	………………………...	
Prof. Dr. Coşkun ÖZALP	Prof. Dr. Ünal AKDAĞ	
MEMBER	MEMBER	

This PhD thesis was prepared at the Department of Mechanical Engineering of the Institute of Natural and Applied Sciences of Çukurova University
Registration Number:

Prof. Dr. Sadık DİNÇER
Director
Institute of Natural and Applied Sciences

This thesis was supported by the Scientific Research Project Office of Çukurova University under Contract no: FDK-2016-6952.

ABSTRACT

PhD THESIS

INVESTIGATION OF HEAT TRANSFER IN CORRUGATED CHANNEL WITH PULSATING FLOW

Harun ZONTUL

UNIVERSITY OF CUKUROVA
INSTITUTE OF NATURAL AND APPLIED SCIENCES
DEPARTMENT OF MECHANICAL ENGINEERING

Supervisor : Prof. Dr. Beşir ŞAHİN
Year: 2021, Pages:127
Jury : Prof. Dr. Beşir ŞAHİN
: Prof. Dr. Hüseyin AKILLI
: Prof. Dr. Mehmet BİLGİLİ
: Prof. Dr. Coşkun ÖZALP
: Prof. Dr. Ünal AKDAĞ

This study presents hydrodynamics and heat transfer of steady and pulsating flow in a rectangular grooved channel for the Reynolds number range of $2x10^3 \leq Re \leq 6.5x10^3$. Three different grooved channel configurations are created by shifting the bottom wall. The Particle Image Velocimetry (PIV) method is employed for hydrodynamic investigation. Streamlines, velocity vectors, vorticity contours are plotted to reveal massive flow motions and flow patterns. Results showed that groove and mainstream interaction is poor at low Reynolds numbers, but it gets better as the Reynolds number increased. Flow pulsation significantly empowers the penetration of mainstream into the groove section; however, pulsation frequency has an important effect on this phenomenon. Moreover, Reynolds stress and root mean square of the fluctuations are presented to document turbulence statistics. In the heat transfer experiments, the positive effects of the improvement of the groove mainstream interaction and an increase of the turbulence mixing are observed. Heat transfer enhancement, pressure drop trade-off are considered by calculating the thermal performance factor. Pulsating flow caused additional heat transfer enhancement. However, it is a more effective method in low Reynolds numbers. Shifting the bottom wall of the channel does not have an important effect on flow and heat transfer. In addition to the experimental part, a numerical study is carried out to examine the effect of groove aspect ratio and optimum aspect ratio for steady flow.

Key words: Grooved channel, hydrodynamics, heat transfer, PIV, pulsating flow

ÖZ

DOKTORA TEZİ

OLUKLU KANALDA SALINIMLI AKIŞTA ISI TRANSFERİNİN İNCELENMESİ

Harun ZONTUL

ÇUKUROVA ÜNİVERSİTESİ
FEN BİLİMLERİ ENSTİTÜSÜ
MAKİNE MÜHENDİSLİĞİ ANABİLİM DALI

Danışman : Prof. Dr. Beşir ŞAHİN
Yıl: 2021, Sayfa:127
Jüri : Prof. Dr. Beşir ŞAHİN
: Prof. Dr. Hüseyin AKILLI
: Prof. Dr. Mehmet BİLGİLİ
: Prof. Dr. Coşkun ÖZALP
: Prof. Dr. Ünal AKDAĞ

Bu çalışma, dikdörtgen oluklu bir kanalda sabit ve salınmlı akışın, Reynolds sayısının $2x10^3 \leq Re \leq 6.5x10^3$ aralığı için hidrodinamiğini ve ısı transferini sunmaktadır. Alt duvar kaydırılarak üç farklı oluklu kanal konfigürasyonu oluşturulmuştur. Parçacık Görüntülemeli Hız Ölçümü (PIV) yöntemi hidrodinamik inceleme için kullanılmıştır. Akım çizgileri, hız vektörleri, girdap konturları, kütlesel akış hareketlerini ve akış yapılarını ortaya çıkarmak için çizilmiştir. Sonuçlar, oluk ve ana akım etkileşiminin düşük Reynolds sayılarında zayıf olduğunu, ancak Reynolds sayısı arttıkça daha iyi hale geldiğini göstermiştir. Salınımlı akış, ana akımın oluk içine nüfuz etmesini önemli ölçüde güçlendirmiştir, ancak salınım frekansı bu fenomen üzerinde önemli bir etkiye sahiptir. Ayrıca, türbülans istatistiklerini belgelemek için Reynolds gerilimi ve çalkantıların karelerinin karekök ortalamaları sunulmuştur. Isı transferi deneylerinde, oluk ana akım etkileşiminin iyileştirilmesinin ve türbülans karışımının artmasının olumlu etkileri gözlenmiştir. Isı transferi iyileştirilmesi ve basınç düşüşü arasındaki ilişki, termal performans faktörü hesaplanarak dikkate alımıştır. Salınımlı akış, ek ısı transferi artışına neden olmuştur. Ancak bu yöntem düşük Reynolds sayılarında daha etkilidir. Kanalın alt duvarının kaydırılmasının akış ve ısı transferi üzerinde önemli bir etkisi yoktur. Deneysel bölüme ek olarak, sabit akışta oluk en boy oranının etkisini incelemek için sayısal bir çalışma yapılmıştır ve optimum en boy oranı sunulmuştur.

Anahtar Kelimeler: Oluklu kanal, hidrodinamik, ısı transferi, PIV, salınımlı akış

EXTENDED ABSTRACT

Hydrodynamics and heat transfer of steady and pulsating flow passing through a channel with periodic grooves placed top and bottom walls investigated in this study. Reynolds number, Re is varied between $2x10^3$ and $6.5x10^3$ for both steady and pulsating flow cases. The pulsation frequency, F is increased to a maximum value of 5 Hz. Three different channel configurations are created by shifting the bottom wall. Flow hydrodynamics is investigated by using Particle Image Velocimetry (PIV) method. Flow patterns in the channel are showed by using streamlines and velocity vectors. Utilizing the ability of the PIV that enables to capture instantaneous flow data, massive fluid flow motions between grooves and mainstream also the evolution of the circulation regions inside the grooves in time are visualized. Results indicate that groove-mainstream interaction is poor at low Reynolds numbers, Re of the steady flow. As the Reynolds number, Re increases, interaction is enhanced so that significant flow transfer occurs between grooves and the mainstream. Fluid flow that enters the groove near the downstream corner circulates inside the groove and then rejoins to the mainstream. Pulsating flow improves the ability of mainstream to penetrate groove sections. During the successive variation of the flow velocity, individual phases occurs that facilitate the fluid transfer from the mainstream to the groove section or vice versa. The acceleration phase of the pulsation period creates favorable conditions for the fluid flow to enter the groove area, and the deceleration phase is suitable to rejoin of fluid flow inside the groove to the mainstream. The frequency of the pulsation, F is an important parameter affecting this phenomenon.

Turbulence statistics are documented by plotting the averaged Reynolds stress, root mean square of the fluctuating components in streamwise, $\overline{u'_{rms}}$ and transverse $\overline{v'_{rms}}$ directions. Results show that regions of high Reynolds stress appear over the mouth of each groove where separated shear layers are located.

This indicates grooves have a function of generation of turbulence fluctuations which also means the enhancement of the mixing in the channel. The intensity of the Reynolds stress increases as the Reynolds number rises. The distribution of the Reynolds stress patterns is different for each phases of the pulsation. Phase averaged Reynolds stress contours are presented for low, medium (acceleration), and peak velocity phases. The low-velocity phase of the pulsation is the phase that higher Reynolds stresses are seen in a larger region inside the channel. During the acceleration phase, areas with the high Reynolds stresses get smaller and at the peak velocity phase, high Reynolds stress levels are only seen in a small Region at the separated shear layers. Moreover, the contours of $\overline{u'_{rms}}$ and $\overline{v'_{rms}}$ indicate that high $\overline{u'_{rms}}$ values are intensified at shear layers, but, $\overline{v'_{rms}}$ levels with medium and high values spread over a larger area. Also the $\overline{v'_{rms}}$ variation is more dramatic than $\overline{u'_{rms}}$ variaton through the period of the pulsation. The frequency of the pulsation has a prominent influence on the levels of turbulence fluctuations.

Convective heat transfer and pressure drop through the channel are presented non-dimensionally by Nusselt number, *Nu,* and friction factor *f* respectively. The positive effect of enhancing turbulent mixing by using the grooved channel is seen in heat transfer experiments for steady flow. Significantly higher Nusselt number, *Nu* values are obtained in the grooved channel than the straight channel. However, pressure drop caused by the grooved channel also becomes higher than the straight channel. The trade-off between heat transfer enhancement and pressure drop increase is considered by calculating the thermal performance factor, *TPF*. *TPF* is greater than unity for all investigated cases, which indicates that despite the increase in pressure drop, the total energy gain of the system is positive. Increase of the Reynolds number, *Re* provided better heat transfer but thermal performance factor, *TPF* reaches a peak at a certain value of the Reynolds number, *Re* and then starts to decrease for higher values of the Reynolds number, *Re*.

Implementation of the flow pulsation caused additional heat transfer enhancement in the grooved channel. However, pulsating flow is more effective in low Reynolds numbers. Since interactions between groove and mainstream as well as turbulent flow mixing are quite poor in low Reynolds numbers, perturbation of the flow by pulsation causes a substantial increase in heat transfer for these Reynolds numbers. The amount of the heat transfer enhancement showed strong dependence on the pulsation frequency. An optimum value of the frequency provides the best heat transfer enhancement, and its value changes with the Reynolds number, *Re*. Shifting the bottom wall does not cause a considerable difference in heat transfer for both steady and pulsating flows.

In addition to experiments, a numerical study is carried out to investigate the effect of the groove aspect ratio on heat transfer and pressure drop for steady flow. Six different groove aspect ratios are tested for the investigation and the aspect ratio that gives optimum heat transfer and pressure drop is presented.

GENİŞLETİLMİŞ ÖZET

Bu çalışmada üst ve alt duvarlara periyodik oluklar yerleştirilmiş bir kanaldan geçen sabit ve salınımlı akışın hidrodinamiği ve ısı transferi incelenmiştir. Reynolds sayısı, hem sabit hem de salınımlı akış durumları için $2x10^3$ ile $6.5x10^3$ arasında değişmektedir. Salınım frekansı maksimum 5 Hz'e kadar yükseltilmiştir. Alt duvar kaydırılarak üç farklı kanal konfigürasyonu oluşturulmuştur. Hidrodinamik, Parçacık Görüntülemeli Hız Ölçümü (PIV) yöntemi kullanılarak incelenmiştir. Kanaldaki hız dağılımları, akım çizgileri ve hız vektörleri eşdeğer erğrileri ile gösterilmiştir. PIV' nin anlık akış verilerini yakalama imkanını kullanılarak, oluklar ve ana akım arasındaki büyük anlık akış hareketleri, aynı zamanda oluklar içindeki sirkülasyon bölgelerinin zaman içindeki değişimi görselleştirilmiştir. Sonuçlar, oluk ile ana akım etkileşiminin, daimi akışın düşük Reynolds sayılarında zayıf olduğunu göstermektedir. Reynolds sayısı, *Re* arttıkça etkileşim artmış, böylece oluklar ve ana akış bölgesi arasında önemli akışkan aktarımı meydana gelmiştir. Oluk boşluklarına giren akışkan, bu kesit alanında sirküle etmiş ve ana akıma yeniden katılmıştır. Salınımlı akış, ana akımın oluk iç derinliklerine nüfuz etme yeteneğini geliştirmiştir. Akış hızının art arda değişmesi sırasında, ana akımdan oluğa veya tersi yönde akış transferini kolaylaştıran ayrı fazlar meydana gelmiştir. Salınım periyodunun hızlanma fazı, akışkanın oluk boşluğuna girmesi için uygun koşullar yaratmaktadır. Yavaşlama fazı ise oluk içindeki akışkanın ana akıma tekrar katılması için uygun ortam yaratmaktadır. Salınım frekansı, bu akış olayını etkileyen önemli bir parametredir.

Türbülans istatistikleri, ortalama Reynolds gerilimi, çalkantı bileşenlerinin akım yönünde, $\overline{u'_{rms}}$ ve enine yönde $\overline{v'_{rms}}$ karelerinin karekök ortalamalarını eşdeğer eğrileri çizilerek belgelenmiştir. Sonuçlar, yüksek Reynolds gerilimine sahip bölgelerin, her oluk ağzı üzerindeki ayrılmış akış bölgelerinde yeraldığını göstermektedir. Bu, olukların türbülans çalkantıları oluşturma işlevine sahip olduğunu gösterir ve aynı zamanda kanal içerisindeki karışımın arttığı anlamına

gelmektedir. Reynolds sayısı, *Re* arttıkça Reynolds geriliminin şiddeti artar. Reynolds gerilim eşdeğer eğrilerinin dağılımı, salınımın her bir fazı için farklıdır. Faz ortalamalı Reynolds gerilim eşdeğer eğrileri, düşük, orta (ivmelenme) ve tepe hız fazları için sunulmuştur. Salınımın düşük hızlı fazı, kanalın içinde daha büyük bir bölgede daha yüksek Reynolds gerilimlerinin görüldüğü fazdır. İvmelenme fazı sırasında, yüksek Reynolds gerilmelerine sahip alanlar küçülür ve tepe hız fazında, yüksek Reynolds gerilme seviyeleri yalnızca ayrılmış akış alanında küçük bir bölgede görülür. Ayrıca, $\overline{u'_{rms}}$ ve $\overline{v'_{rms}}$ eşdeğer eğrileri göstermiştir ki, yüksek $\overline{u'_{rms}}$ değerleri kayma tabakasında yoğunlaşmıştır. Ancak, orta ve yüksek değerli $\overline{v'_{rms}}$ seviyeleri daha fazla alana yayılmıştır ve, $\overline{v'_{rms}}$'in salınım periyodu boyunca değişimi, $\overline{u'_{rms}}$' den daha dramatiktir. Sonuç olarak, salınım frekansı türbülans çalkantılarının seviyeleri üzerinde önemli bir etkiye sahiptir.

Kanal boyunca taşınımla ısı transferi ve basınç düşüşü boyutsuz olarak sırasıyla Nusselt sayısı, *Nu* ve sürtünme faktörü *f* ile temsil edilmiştir. Oluklu kanal kullanılarak türbülans karışımının arttırılmasının olumlu etkisi, sabit akış için ısı transferi deneylerinde görülmektedir. Oluklu kanalda, düz kanala göre önemli ölçüde daha yüksek Nusselt, *Nu* değerleri elde edilmiştir. Ancak oluklu kanalın neden olduğu basınç düşüşü de düz kanala göre daha yüksektir. Isı transferindeki iyileştirme ile basınç düşüşündeki artış arasındaki denge, termal performans faktörü *TPF* hesaplanarak göz önünde bulundurulmuştur. *TPF*, araştırılan tüm durumlar için birden büyüktür, bu da basınç düşüşündeki artışa rağmen sistemin toplam enerji kazancının pozitif olduğunu gösterir. Reynolds sayısının artması, *Re* daha iyi ısı transferi sağlamış ancak termal performans faktörü, *TPF*, Reynolds sayısının belirli bir değerinde zirveye ulaşır ve daha sonra Reynolds sayısının, *Re* daha yüksek değerleri için azalmaya başlar.

Salınımlı akışın uygulanması, oluklu kanalda ek ısı transfer artışına neden olmuştur. Bununla birlikte, düşük Reynolds sayılarında, *Re* salınımlı akış daha etkilidir. Düşük Reynolds sayılarında oluk-ana akım etkileşimi ve türbülans karışımı oldukça zayıf olduğundan, salınım ile akışın rahatsız edilmesi, bu Reynolds sayıları için ısı transferinde önemli bir artışa neden olur. Isı transferi artışının miktarı, salınım frekansına güçlü bir şekilde bağlıdır. En iyi ısı transferi iyileştirmesini sağlayan optimum bir frekans değeri vardır ve değeri Reynolds sayısı Re ile değişmektedir. Alt duvarın kaydırılması, hem sabit hem de titreşimli akış için ısı transferinde önemli bir farka neden olmamıştır.

Deneylere ek olarak, sabit akış için oluk en-boy oranının ısı transferi ve basınç düşüşü üzerindeki etkisini araştırmak için sayısal bir çalışma yapılmıştır. Araştırma için altı farklı oluk en boy oranı test edilmiş ve optimum ısı transferi ve basınç düşüşü sağlayan en boy oranı sunulmuştur.

ACKNOWLEDGMENTS

I would like to express my special thanks and gratitude to my supervisor Prof. Dr. Beşir ŞAHİN for his counseling, motivational support and encouragement.

I would also thank the head of the Mechanical Engineering Department and the staff to provide me technical infrastructure and their support.

My sincere thanks also go to Sefa MERAL for his assistance with the manufacturing and assembling of the experimental setup.

Further, I am also thankful to the to the Scientific Research Project Office of Çukurova University for the financial support (Project Number: FDK-2016-6952).

Last but not least, I would like to thank my family for supporting me spiritually throughout my life.

CONTENTS **PAGE**

LIST OF TABLES **PAGE**

LIST OF FIGURES **PAGE**

NOMENCLATURE

A_p : Pulsation amplitude

A_s : Outer surface area of the heated wall

b : Bulk

C_p : Specific Heat (j/Kg.K)

f : Friction factor

H : The channel height (mm)

h : Convection coefficient (W/m^2K)

I : Current applied to the wall heaters (Ampere)

k : Turbulence kinetic energy

L : Lenght of the groove period (mm)

l : Depth of the groove (mm)

Nu : Nusselt number

n : Groove aspect ratio

P : Pressure (Pascal)

$\dot{q}$: Heat flux (W/m^2)

q : Heater power (W)

q_{loss} : Heat loss from the wall heaters (W)

Pr : Prandtl number

Re : Reynolds number

S : Total lenght between pressure measurement locations (m)

T : Temperature (K)

TPF : Thermal performance factor

t : time (s)

u : Velocity in x direction (m/s)

u_{mag}......: Velocity magnitude (m/s)

v : Velocity in y direction (m/s)

V : Voltage applied to the wall heaters (Volt)

w : Width of the channel

Greek Letters

F : Pulsation frequency (Hz)

ρ : Density of the water (kg/m^3)

μ : Dynamic viscosity of the water (kg/m.s)

λ : Thermal conductivity (W/m K)

ε : Turbulence dissipation rate

Γ : Thermal diffisuvity

Δ : Difference

Subscripts

g : Grooved section

s : Straight section

0 : Inlet

w : Wall

i : x-component

j : y-component

t : Turbulent

rms : Root mean square of the quantity

Superscripts

‘ : Fluctuation component

— : Time average

1. INTRODUCTION

Energy has become an indispensable necessity for modern life after the industrial revolution. However, due to limited resources, costs, environmental factors, and increasing demand over time, the efficiency of energy production, consumption, and transformation processes have become more critical. According to the U.S. Energy Information Administration (2020), the world's energy demand will increase by nearly 50% over 2050. The rapid increase in the global market is the primary motivation for researches on the efficiency of energy-containing processes. Studies to increase energy efficiency are within the scope of many different disciplines. However, efforts to improve heat transfer have an essential impact on energy efficiency from the production level to the end-user consumption level since most of these processes somehow involve heat transfer.

Approximately 77 percent of the world's electricity production in 2018 includes processes that transform thermal energy into electrical energy (International Energy Agency (2020)). Besides electricity generation, thermal energy is a resource that can be used directly in the manufacturing, chemical and food industries. It is also a resource that can be recovered in intense heat industries like metal and cement production. Moreover, the electirical consumption of home appliances like refrigerators and air-conditioners is directly related to their ability to transfer heat between source and sink. Computing performance of microprocessors is affected by their temperature, so they need to be cooled to keep them efficient. In all the examples above, heat exchangers play a significant role and they are an important determinant of the overall efficiency of the system. Therefore, increasing the efficiency of heat exchangers has been an issue that has got the attention of researchers for a long time. Increasing convective heat transfer in internal flow is done by increasing the mixing between flow near heat transfer surfaces and core flow. Methods that is used for this purpose are classified under three topics. The classification is based on whether extra energy is required or not.

If an enhancement is achieved without consuming additional energy than pumping power, the method is called the passive enhancement method. However, if there is an external energy usage the method is called the active method. Some times active and passive methods are used together; these cases are called compound methods.

1.1. Passive Heat Transfer Enhancement Methods

In passive methods, heat transfer enhancement is obtained by modifying surface geometry or using fluid additives. Surface modification aims to enlarge the area where heat transfer occurs and to enhance the convective heat transfer by increasing the mixing of fluid. The surface pattern of a typical plate heat exchanger shown in Figure 1.1 is an excellent example of this method. Ribs, grooves, surface roughness, guide vanes, vortex generators are common geometry modifications used as a passive heat transfer enhancement method. The type of the method that is used depends on the type of the heat exchanger, the Reynolds number, and size constraints. The most significant disadvantage of the methods which increase heat transfer by interfering with the surface geometry is that they also increase the pressure loss. For this reason, researchers try to find the optimum geometry configuration that provides better heat transfer enhancement with reasonable pumping power.

Heat exchanger performance can also be enhanced by increasing the thermal conductivity of the working fluid. This can be done by the addition of high thermal conductive solid materials in to the base fluid. The use of micro and larger-sized solid particles for this purpose has been a known method for a long time. However, since the use of particles of this size has some disadvantages like corrosion, clogging, and sedimentation, it could not find much application area in practice. Advancement in the nanotechnology has enabled to the production of particles in nanometer size so sedimentation and clogging problem has become less prominent and use of fluid additives as a heat transfer improvement method got the attention of researchers. Nanofluids cause considerable enhancement in heat transfer; however, this does not mean they provide gain without any cost. The addition of nanoparticles into the working fluid increaseses the shear stress, which means higher pumping power. Therefore care must be taken when determining the percentage of nanoparticles in the base fluid (Gosselin and Da Silva (2004)).

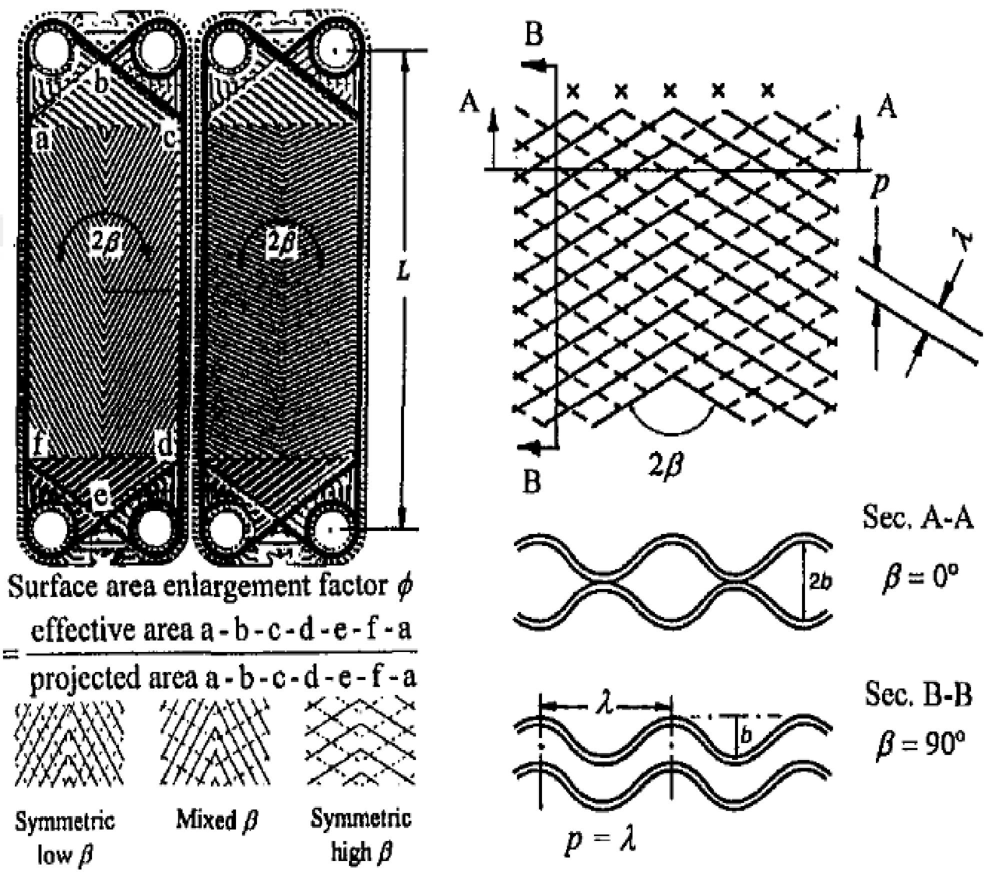

Figure 1.1. An example for surface geometry of plate heat exchanger. *(From Muley, A., and R. M. Manglik. "Experimental study of turbulent flow heat transfer and pressure drop in a plate heat exchanger with chevron plates." (1999): 110-117.)*

1.2. Active Heat Transfer Enhancement Methods

Enhancement of mixing can be achieved by disturbing the flow by external forces. These methods can be more aggressive than passive methods in the creation of disturbance. The most popular active heat transfer enhancement methods used in researches are as follows;

Magnetic and Electrostatic Fields: Magnetic and electrostatic fields behave as external body forces on flow. Controlling the flow with electrostatic forces is done by applying a low current and high voltage to the dielectric fluid. However, the control performed by magnetic forces is done by applying a magnetic field to conductive liquids. In these two methods, the flow control can be used to obtain a better mixing. In addition, the purpose of flow control is to eliminate the situations that can adversely affect the heat transfer, such as flow separation. Magnetic forces are more effective at low Reynolds numbers and natural convection conditions where momentum forces are less effective.

Mechanical Aid: Heat transfer enhancement by mechanical aids is based on either movement of heat transfer surface or move/rotation of other objects in the vincinity of the heat transfer surface. Rotating cylinders near heat transfer surface or rotating tubes being cooled are such common examples of this method.

Pulsating Flow: Periodic variation of the flow rate over time is a phenomenon that significantly affects the mixing. The frequency and amplitude of pulsation are two main parameters in this type of flow. Moreover, variation of flow rate can be sine wave form or square wave form. If necessary, reverse flow can be obtained during pulsation depending on its effectiveness in application. For example, pulsating flow is more effective in enhancing heat transfer when it is used together with corrugated surfaces than flat surfaces.

Acoustic Waves: Acoustic waves enhance heat transfer in two ways; they produce acoustically-induced streams and cause acoustic cavitation. Acoustically induced stream is only effective for low Reynolds numbers and natural convection. In acoustic cavitation, the implosion of the bubbles creates a disturbence in flow and enhances the mixing process. However, the method also causes erosion on surfaces.

Synthetic Jets: Synthetic jets are created by sucking surrounding fluid in the flow domain and ejecting it from the small cavity. Heat transfer is enhanced by directing the jet to the heat transfer surface. Since the method does not require an extra fluid source, it is practical to use in heat transfer improvement applications.

1.3. Compound Heat Transfer Enhancement Methods

Better results in heat transfer improvement can be achieved by using active and passive methods together. Passive methods are more preferred since they are easier to implement. However, their heat transfer enhancement capability is limited. For example, in corrugated channels surfaces in corrugations are poor locations for heat transfer due to low flow velocity. Employing an active method makes it possible to interact with the high flow velocity region to the surface area of corrugations so the frailty of the corrugated channel is eliminated and heat transfer beyond the limit of the passive method is achieved.

2. LITERATURE SURVEY

2.1. Preliminary Stuides About Grooved and Ribbed Channels

Ribbs and grooves are the most widely researched passive heat transfer improvement methods in channels. By examining different rib and groove geometries, the researchers aimed to obtain the best heat transfer for the least pressure loss under certain conditions. The literature emerging as a result of these studies is given in the section below.

Surface modifications are known to create instability in laminar flow. An early study investigating the unsteadiness created by ribs placed at the bottom wall of the channel was published by Labbe and Lê (1970). They reported heat transfer enhancement as a result of unsteady flow. Gahaddar et al. (1986) presented the mechanism of self-sustained flow oscillations in the rectangular grooved channel and found the critical Reynolds number which unsteadiness starts. Numerical study of Nigen and Amon (1994) presented the distribution of local Nusselt number and skin friction coefficient along a period of a groove for different Reynolds numbers at the laminar and transitional regime. Iyer et al.(1997) studied the effect of various groove lengths for geometry defined by Gahaddar et al. (1986). They found an optimum groove length that provides the best heat transfer without a significant increase in pressure drop penalty. Grenier et al.(1998) performed a direct numerical simulation to detect the onset of unsteadiness for a channel with triangular grooves at the bottom wall. Another numerical study to detect critical Reynolds number for unsteadiness was conducted by Stone and Vanka (1999) for the wavy corrugated walls. Ghaddar and El-Haji (2000) found the natural frequency of unsteady flow in the corrugated channel and reported that investigated corrugated channel geometry causes substantial heat transfer enhancement compared to the straight channel. Adachi and Uehara (2001) numerically investigated the effect of groove depth on heat transfer and pressure drop. Herman and Kang (2002) experimentally investigated cooling of periodically placed hot blocks in a channel. They used curved vanes to direct the high-velocity stream into the groove between blocks and obtained a considerable increase in heat transfer. Ridouane and Campo(2007) obtained significant heat transfer enhancement by placing hemi-circle cavities to both the upper and lower walls of the channel. Their results showed that small cavity depth is more favorable in terms of heat transfer. L. Li et al(2008) reported that flow entering rectangular grooved channels starts to oscillate after several grooves, the amplitude of oscillation reaches a certain value in a few groove periods and time-averaged Nusselt numbers vary periodically along the channel. Guzmán et al.(2009) investigated flow birufication and transition from laminar to the transitional regime for three different aspect ratios of the wavy channel and two Prandtl numbers. Better heat transfer results were reported for the transitional regimes in the study. Sun et al.(2010) investigated the characteristic of flow oscillations induced by grooves. They stated that the amplitude of oscillation is related to the length of the groove and wave amplitudes are stronger near the first and last groove periods. A study by Ahmed et al. (2012) revealed that increasing the amplitude of wavy wall increases skin-friction coefficient however it was also reported that volume fraction of nanoparticles is a more important parameter than wave amplitude for heat transfer. Yang et al.(2014) carried out an optimization study for convective heat transfer and pressure drop in the wavy channel. Reynolds number, the amplitude of the wavy channel, number of wave periods, type, and volume fraction of nanofluids are investigated parameters in the study. Another optimization study was performed which is considering the depth, tip length, pitch, position, and type of the grooves for micro channel heat sinks by H.E. Ahmed and M.I. Ahmed(2015). Rostami et al.(2015) showed that wavy walls gives better heat transfer than straight walls for micro channel and offered optimum wavy channel geometry by investigating different wavelenght, wave amplitude, aspect ratio and wall thickness. Bahnemiri et al.(2015) used the Artificial Bee Colony algorithm to optimize heat transfer from a wavy channel under laminar flow conditions. Zhu et al.(2016) obtained better heat transfer from a heat sink by using wavy fins instead of plain fins. Study of Ramgadia and Saha (2016) revealed that 0 degree phase shift between upper and lower walls is better for creating fluctuation in flow than other configurations. Also, it causes the highest heat transfer rate and pressure drop. Mills et al. (2016) carried out Lattice Boltzman Simulation for pressure-driven flow and heat transfer in the asymmetric wavy channel. Results of simulations showed that heat transfer severely depends on pressure difference after a critical Reynolds number than the amplitude of wavy wall. Akberzadeh et al. (2017) numerically simulated flow and heat transfer in wavy, trapezoidal, and triangular corrugated channels and reported the performance coefficient and entropy generation of these channel types for different Reynolds numbers in the laminar regime. Aliabadi (2017) used a non-uniform wavy wall where the wavelength differed along channel and configuration with wavelenght value changes from low to high along streamwise direction gave better performance than uniform and other non-uniform wavy wall configurations. According to the work of Mehta and Pati (2018), amplitude and wave length strongly affect heat transfer and pressure drop in the triangular corrugated channel. In addition, total entropy generation increases until critical Reynolds number, but it remains constant for higher Reynolds numbers. Singh et al. (2019) visualized the temperature field in a sinusoidal wavy channel by using a Mach-Zehnder interferometer for laminar flow conditions. Their results showed a periodic variation of the thermal boundary layer along the channel and a decrease of its thickness with increasing nanofluid volume fraction. D. Vo et al. (2019) used an unusual type of nanofluid in their numerical study for the wavy channel. They tested different shapes of boehmite alumina particles and modelled nanofluid by a two phase mixture model. The study showed that nanoparticle shapes cause different enhancement values with increasing Reynolds numbers, and brick-shaped nanoparticles provide the best thermal enhancement factor. It is evident from the studies shown above that, geometrical modifications such as grooves and ribs have a significant effect, in converting the flow from steady-state to unsteady state in laminar conditions. However since pressure drop also increased, researchers aimed to find the best geometrical configurations in certain flow conditions, and optimization studies were presented for some typical geometries. Moreover, emerge of nanofluids caused additional capability in terms of heat transfer enhancement.

In turbulent flow, surface modifications have the function of increasing turbulent mixing. Studies about turbulent flow in ribbed and grooved channels report considerable heat transfer enhancement. In turbulent flow, the eddy flow structure provides a faster and more excellent transfer of mass, momentum, and heat to other parts of the flow than molecular diffusion. As a result of this situation, friction, heat transfer, and mass transfer coefficients become much more significant in turbulent flow

J. C. Han (1988) achieved two to three times better heat transfer on ribbed walls than smooth walls. Heat transfer enhancement was not limited to ribbed walls but it was also increased on side walls. J. C. Han et al. (1991) studied the effect of various rib angles on heat transfer and found out that 60 degree V-shaped rib provides the best heat transfer but 60 degree crossed ribs cause the lowest pressure drop. Liou et al. (1992) investigated the flow and heat transfer in a channel with a different pitch to rib-height ratios numerically and experimentally. They used LDA and documented local velocity and turbulence kinetic energy in the channel. Temperature distribution on the grooved bottom wall of a channel was measured by Lorenz et al.(1995) using infrared thermography. The temperature field showed that heat transfer is high near the front edge of the rib and it is low at the bottom surface of the groove. Chandra et al.(1997) created different cases by using ribs on upper, lower and side walls. They state that heat transfer enhancement gets better as the number of ribbed walls increases. Habib et al. (1998) performed numerical simulations for turbulent flow and heat transfer through the sinusoidally wavy walled channel. Results of simulations revealed considerable heat transfer enhancement but also an increase in pressure drop. Choi and Suzuki (2005) used Large Eddy Simulation (LES) model in their numerical study and showed the instantaneous vorticity field near the wavy bottom wall and its relation with heat transfer from the surface. Ahn et al.(2005) also used the LES method to model turbulent flow in ribbed channels and conducted experiments to validate the simulation results. The underlying mechanism in heat transfer enhancement was explained by demonstrating the entrainment of cold flow to the hot surfaces by vortical structures in the study. Maurer et al.(2007) conducted experiments and numerical simulations for heat transfer through a channel with V-shaped ribs. They obtained considerable heat transfer enhancement using the ribs and reported enhancement level out around Re = $2x10^5$. Kamali and Binesh (2008) examined the effect of four different types of ribs on heat transfer and reported the types that providing the highest heat transfer enhancement andthe lowest friction factor. Eimsa-Ard and Promvonge (2008) determined the groove width that provides a better thermal performance factor by numerically simulating the forced convection in a channel with a grooved bottom wall. In another study performed by Eimsa-Ard and Promvonge (2009) the combined effect of ribs and grooves on heat transfer was investigated. They tested three different cases by changing rib and groove geometry and concluded that thermal enhancement is best for triangular rib-triangular groove combination. Rallabandi et al. (2009) developed correlations as a function of rib spacing, rib height and Reynolds number to predict Nusselt number and friction factor in channels with 45 degree ribs placed on top and bottom walls of the channel. Mohammed et al. (2010) presented a comprehensive study that considers nine types of rib-groove combinations, four different nanofluid types with various nano particle sizes and particle volume fractions, and finally different aspect ratios of the channel. Eimsa-Ard and Changcharoen (2011) tried new rib profiles and found that ribs with a concave surface both upstream and downstream side cause the highest heat transfer and friction factor. Study of Manca et al. (2012) reported that nanofluid use provides considerable heat transfer enhancement for turbulent flow through ribbed channels however, it causes an increase in pumping power too. Xie et al. (2013) used angled ribs in the dimpled channel and reported that a combination of ribs and dimples provides better heat transfer with an admissible increase in pressure drop. Vanaki et al. (2014) numerically studied the effect of phase shift between upper and lower walls of the wavy channel for turbulent nanofluid flow. They concluded that a 30-degree phase shift gives the highest thermal performance factor with ethylene glycol-based SiO_2 nanofluid. Manavi et al. (2014) employed a two phase mixture model in their CFD study about Al_2O_3–water flow in the wavy channel and detected higher Nusselt numbers with mixture model than single-phase model. Yang et al. (2015) also used the mixture model for simulating the flow in a channel with periodic ribs and grooves placed bottom wall. Their results showed that geometrical ratios of rib and groove have an important influence on the heat transfer rate and pressure drop. In addition, they found out that agreement between the single-phase model and mixture model strongly depends on geometrical configuration. Liu et al. (2015) obtained similar heat transfer enhancement with the conventional ribbed channel by using cylindrical grooves without high pressure drop penalty. Moreover, they improved the performance of conventional cylindrical grooves by modifying them. Rashidi et al. (2017) analyzed thermal-hydraulic performance and entropy generation of wavy channels for turbulent flow conditions and reported that lower wave amplitude is more beneficial for both thermal and viscous entropy generation. But, wavelenght cause opposite behaviour in those parameters. Tokgöz et al.(2017) presented a detailed hydraulic behavior of turbulent flow in a rectangular grooved channel with different channel aspect ratios and phase shifts by using PIV. They also numerically investigated thermal performance for the same conditions. Harikrishnan and Tiwari (2018) turned two-dimensional flow in the wavy channel into three-dimensional by applying skewness to the corrugations. Results of the study showed that heat transfer is increased up to 35o skewness angle. Promthaisong and Eimsa-Ard (2019) enhanced heat transfer in solar air heater by using periodic triangular ribs. The promotion of turbulence kinetic energy by ribs was demonstrated in the study. Ajeel et al. (2019) numerically studied turbulent flow and heat transfer in a channel with semi-circle grooves on upper and lower walls and reported that groove height to channel width ratio has much more influence on heat transfer than pitch to length ratio in this type of corrugated channel. Ebrahimi-Moghadam and Jabari Moghadam (2019) presented optimal geometrical parameters to design a corrugated heat exchanger by employing the genetic algorithm and entropy generation minimization approach. Kurtulmus et al. (2020) numerically and experimentally investigated turbulent flow and heat transfer in the wavy channel for various channel heights. Since small channel heights cause significant pressure drop, the best thermal enhancement factor was reported for the largest channel height.

As the above studies show, increasing heat transfer by surface modification is an effective method in the turbulent flow. Therefore, various types of grooves have been tried to discuss their performances. Some of these studies examine the hydrodynamics of flow and show enhancement of turbulence, but the main focus of the most works has been on the rate of heat transfer. Especially the number of experimental investigations on hydrodynamics is very few. The main motivation of the current study is to examine the heat transfer performance of periodically grooved channel with groove length is half of the non-grooved lenght in each period ($L_s/ L_g = 2$) and present detailed hydrodynamic information of flow in this channel.

2.2. Preliminary Stuides About Pulsating Flow in Channels

Pulsating flow has been used as an active heat transfer enhancement method for decades. Studies in the literature shows that its effectiveness may change dramatically in different geometries.

Keil and Baird (1971) applied flow pulsations to water flow in the tube side of a shell and tube heat exchanger and obtained considerable heat transfer enhancement. They also found out that the rate of heat transfer reduction takes place for low pulsation velocities in the theoretical part of the investigation. Faghri et al.(1979) performed a theoretical investigation for pulsating laminar flow and heat transfer through a pipe and reported that amplitude of pulsation has an important effect on the amount of heat transfer enhancement. A numerical study of Rabadi et al. (1982) showed Nusselt number increases with increasing pulsation frequency, but after a certain level, the Nusselt number is not affected by the frequency, in curved tubes. Krishnan and Sastri (1982) investigated the effect of pulsating laminar flow on heat transfer in a double pipe heat exchanger. They reported that heat transfer enhancement by pulsating flow occurs mostly in thermally developing regions, therefore, investigated pulsating flow conditions are not suitable for very long heat exchangers. Al-Haddad and Al-Binally (1989) developed an empirical correlation relating the combined effect of the Reynolds number and pulsation frequency to heat transfer for pulsating flow in the pipe. No significant heat transfer enhancement was detected up to the critical value of the new dimensionless parameter in the study. Cho and Hyun (1990) detected that depending on frequency, the pulsating flow might enhance or deteriorate heat transfer in pipes for laminar flow. Grenier (1991) experimentally showed that when the pulsation frequency is close to the most unstable mode of the flow in the rectangular grooved channel, the resonance effect occurs, which results in considerable heat transfer enhancement. Kim et al. (1993) reported that the effect of pulsating flow on heat transfer is more pronounced in the enterance region of the channel. Moreover, low and moderate pulsation frequencies are more favourable. Chung et al. (1993) numerically studied fully developed laminar pulsating flow and heat transfer in the curved tube. They found out that when Womersley number, Wo is small heat transfer is lower than the non-pulsating case and the Nusselt number converges to the non-pulsating flow Nusselt numbers with increasing Womersley number. According to Mackley and Stonestreet (1994) pulsating flow cause impressively higher heat transfer in baffled tubes than smooth tubes for laminar flow conditions. Moschandreou and Zamir (1997) conducted a numerical studyto reveal that pulsating flow is more effective on heat transfer with low Prandtl numbers for laminar flow through the tube. Valencia and Hinojosa (1997) obtained heat transfer enhancement from the lower wall of the channel located downstream of the backward-facing step using pulsating flow. Kim et al. (1998) investigated the cooling of two heated blocks placed in a channel and observed that flow pulsations has strongly infulence the seperated flow region downstream of the blocks. Also, heat transfer is enhanced with improved entrainment induced by pulsating flow. Gbadebo et al (1999) focused on the thermal enterance region of the pipe and obtained both heat transfer enhancement and detraction depending on the frequency of pulsating flow. Habib et al. (1999) conducted experiments for pulsating turbulent flow and heat transfer in a pipe. Their results showed that heat transfer enhancement is more pronounced at high Reynolds numbers and low pulsation frequencies. Hemida et al. (2002) presented an analytical study about pulsating laminar flow in the pipe. They considered thermal inertia of solid boundaries as a parameter and observed that the pulsation effect on time-avreaged heat transfer increases with higher Biot numbers. Wang and Zhang (2005) numerically investigated pulsating flow and heat transfer in a pipe for turbulent flow conditions and detected an optimum Womersley number which provides the best heat transfer enhancement. Moon et al. (2005) improved heat transfer from block array placed in a channel by imposing flow pulsation at the channel inlet. They reported inter-block spacing, pulsation frequency, and amplitude have a strong influence on heat transfer. Valuela (2005) considered the physical properties of the working fluid are temperature-dependent in simulations for pulsating turbulent flow through a pipe and observed that temperature dependence of properties does not make a significant difference in heat transfer but it cause higher friction on the wall. Liang and Papadakis (2005) used the Large Eddy Simulation model in their numerical study about pulsating flow over inline cylinder array. They showed the how vortex shedding and wake regions behind the cylinders are affected by flow pulsation and reported that no considerable heat transfer enhancement is detected after the third row of cylinders. Chattopadhyay et al.

(2006) reported that the pulsating laminar flow in the pipe does not provide an heat transfer enhancement in the investigated parameter range. Jin et al. (2007) increased heat transfer in a channel with an upper wall which has triangular corrugations by using pulsating flow. They also visualized the flow using PIV in this way revealed how the interaction between flow in groove and mainstream is affected by pulsating flow. According to Suksangpanomrung et al. (2007), pulsating flow reduces the size of the separation bubble at the edge of the bluff plate and augment the heat transfer from the plate. Numerical simulations of Velazquez et al. (2008) revealed that heat transfer from the horizontal wall located behind the backward-facing step reaches a maxiumum when flow pulsations are at the resonant frequency. Experiments conducted by Elshafei et al. (2008) for turbulent flow in pipe showed that pulsating flow might cause heat transfer enhancement or deterioration depending on the frequency and Reynolds number. Ji et al. (2008) performed experiments for a heated square cylinder located in a channel and detected lock-on phenomenon occurs for certain values of pulsation frequencies. They reported that the lock-on regime provides substantial heat transfer enhancement. Huang and Yang (2008) increased the heat transfer from two discrete heat sources with attached porous blocks in a channel by using flow pulsation. Olayiwola and Walzel (2008) conducted flow visualization and heat transfer experiments for the rectangular finned channel. They observed that flow pulsations increase fluid exchange between fins and mainstream; therefore, better heat transfer performance was obtained. In the study of Velaquez et al. (2009), pulsating flow penetrated wake regions in a cavity with inlet and outlet and improved the heat transfer at these locations. Persoons et al. (2009) enhanced the heat transfer performance of a microchannel heatsink by using pulsating flow. Rahgoshay et al. (2012) studied the pulsating laminar flow of nanofluid through a pipe and its effect on heat transfer. Results of the study showed that the effect of pulsation frequency and amplitude on the average heat transfer is not appreciable. However, the increase in pulsation amplitude cause also increases the amplitude of periodically varying instantaneous Nusselt numbers. Jafari et al. (2013) simulated laminar pulsating flow and heat transfer in a sinusoidal wavy channel using the Lattice Boltzmann Method and found that the highest heat transfer is obtained in a particular value of frequency which changes with the Reynolds number. Selimefendigil and Öztop (2014) placed a square obstacle downstream of a backward-facing step; in this way they, increased the heat transfer from the horizontal wall. Additionally, impose of flow pulsation caused an extra heat transfer enhancement in their setup. Akdağ et al. (2014) carried out a numerical investigation for pulsating laminar flow through wavy mini-channel and reported that nano-particle volume fraction and pulsation amplitude has significantly increased heat transfer. However, pulsation frequency has no prominent impact. Mehta and Khandekar (2015) stated that the effect of pulsating flow in a straight mini-channel is marginal. Wantha (2016) enhanced the performance of the finned tube heat exchanger using pulsating flow. Mikheev et al. (2017) conducted flow visualization and heat transfer experiments for pulsating flow around the cylinder. They observed four types of flow patterns that changed depending on pulsation amplitude in a fixed frequency and detected flow pattern that provides the highest heat transfer. Gao and Jun Li (2018) investigated the effect of flow pulsation on heat transfer for different rib angles and found that optimum pulsation frequency changes with rib angle. Naphon and Wiriyasart (2018) used pulsating flow and magnetic field together to enhance heat transfer from the helically corrugated tube. Molochnikov et al. (2019) applied flow pulsations to a tube bundle and achieved an increase in heat transfer. According to Blythman et al. (2019), instantaneous Nusselt number varies periodically in time under flow pulsation; however, averaged Nusslet number is lower than the steady case in the straight channel. Bizhaem et al. (2019) shown that flow pulsations increase heat transfer and pressure drop in helically coiled tubes. Nassar et al. (2019) used pulsating flow and magnetic field to improve the thermoelectric cooler's performance. Davletshin et al. (2020) experimentally investigated heat transfer in a channel with a rib placed before the heated wall for pulsating flow conditions. They found that the highest heat transfer enhancement occurs near the wake of the rib. Kurtulmuş and Şahin (2020) presented an experimental study for pulsating turbulent flow through the wavy channel and heat transfer. Their results show that pulsating flow has more impact on heat transfer for low Reynolds numbers. Xu et al. (2020) stated that the use of pulsating flow together with nanofluid increases the efficiency of the micro channel heat sink. Pan et al. (2020) experimentally and numerically investigated pulsating flow in rectangular grooved channels at low Reynolds numbers. They reported that pulsating flow creates instability; therefore, heat transfer is increased due to improved mixing between the main flow and groove.

Previous studies show that pulsating flow is used as an active heat transfer enhancement method with various geometries and Reynolds numbers. The effectiveness of the method changes depending on the type of the geometry, frequency of the pulsation, and the Reynolds number. In the current study heat transfer from the rectangular grooved channel is investigated for pulsating flow conditions. The use of pulsation in grooved/corrugated channels is not a new idea, however, most of the studies are focused on low Reynolds numbers, and information about the hydrodynamics of pulsating flow in grooved/corrugated channels is limited. In this study heat, transfer enhancement ability of the pulsating flow is investigated for relatively higher Reynolds numbers than the studies in the literature. Moreover, hydrodynamic of the pulsating flow is documented by employing PIV which is a strong flow visualization method.

3. MATERIALS AND METHODS

3.1. Description of Experimental Setup

The schematic view of the test setup used for heat transfer and flow experiments is shown in Figure 3.1. The system is a closed-loop working between two reservoirs connected via two lines.

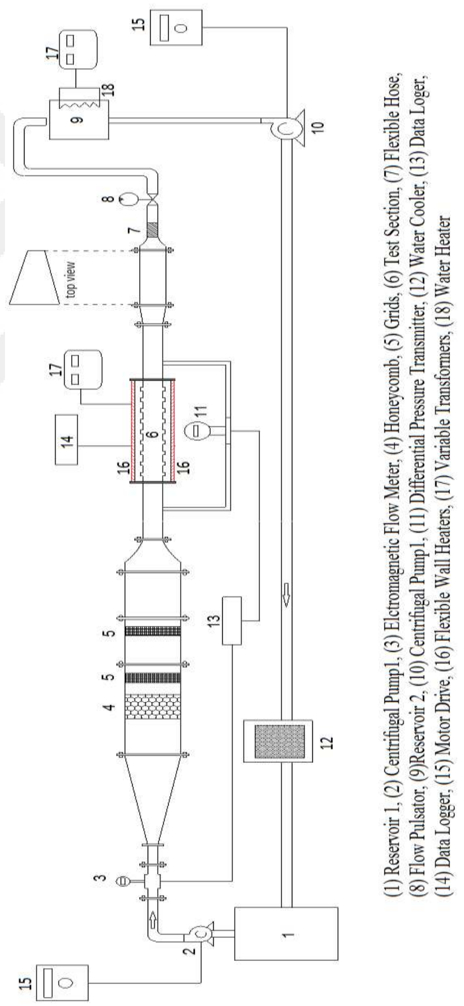

Figure 3.1. Schematic view of the experimental setup.

The first line is the one in which the test section is placed. Water is supplied to this line from reservoir 1(1) by using a centrifugal pump (2) with 0.65 kW motor power and the flow rate is adjusted by controlling the rotation speed of the pump motor with ABB AC355 drive (15). Flow rate is measured by an electromagnetic flowmeter (3) which has a 5Hz sampling rate. The connection between the pipe coming from the magnetic flow meter and the water channel is provided with a diffuser that has a 4^{o} inclined to avoid flow separation. The water channel and diffuser are manufactured from plexiglass with a thickness of 1 cm. Water leaving diffuser passes through a honeycomb(4) for flow straightening and two screens (5) are placed after the honeycomb. A contraction part shaped based on the fifth-order polynomial function (Nedyalkov, 2012; Bell and Mehta, 1988) reduces the height of the channel to the test section (6) height. Before and after the test section calming sections are placed, the length of the calming sections is 360mm. The test section consists of 6061 aluminum upper and lowers walls, and plexiglass side walls are connected to the water channel by using PVC flanges. Due to its low thermal conductivity, PVC provides thermal insulation between the test and the water channels. Constant heat flux is applied from the outer surface of upper and lower walls by using flexible heaters (16), and thermal paste is applied between the heater and the wall to reduce thermal resistance. A slit is opened in the middle of the heater used on the upper wall to enable the placement of thermocouples for wall temperature measurement. The amount of heating is determined by adjusting the applied voltage, V, and current, I to the flexible heaters via a variable transformer (17), and its value is calculated using measured voltage and current. Twelve layers of ceramic fiber paper cover heated walls and sidewalls, as shown in Figure 3.2, to reduce heat loss. These ceramic fiber papers have a 3-mm thickness, and their thermal conduction coefficient is 0.058 W/mK. The insulated test section is pressed from above and below to ensure heaters contact the surface everywhere. At the end of the water channel another contraction connects the channel to a pipe. A flow pulsator mechanism (8) is placed at 2m downstream of this pipe to modify flow rate according to Eqn. 1.

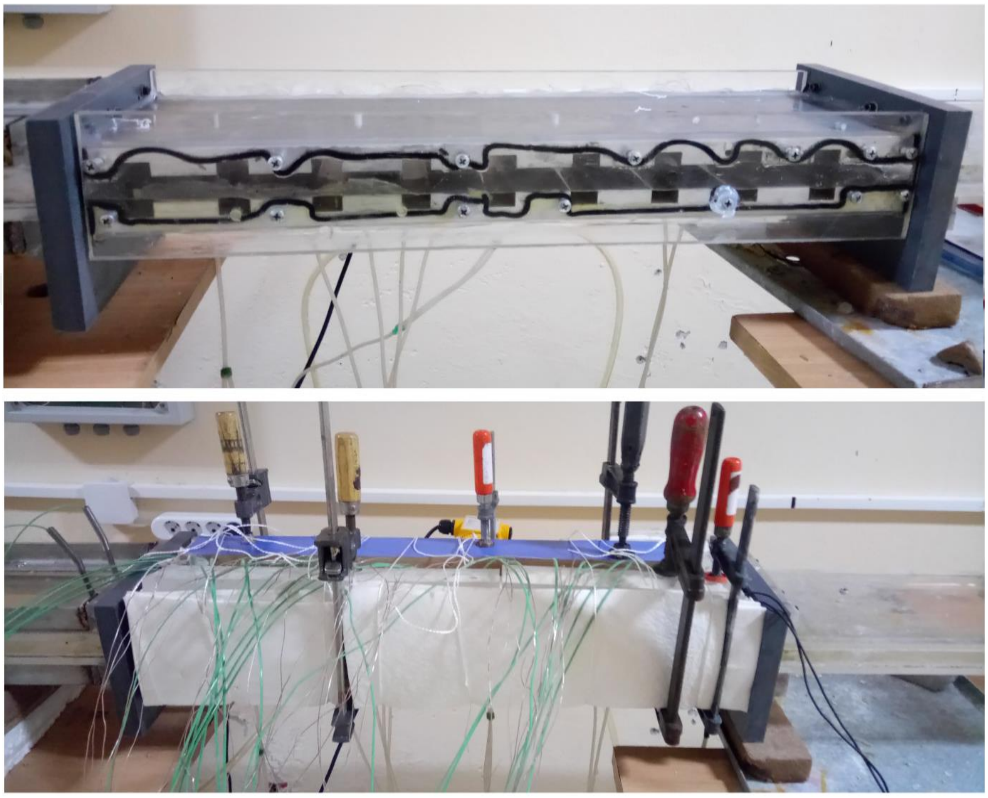

Figure 3.2. Bare and insulated views of the test section.

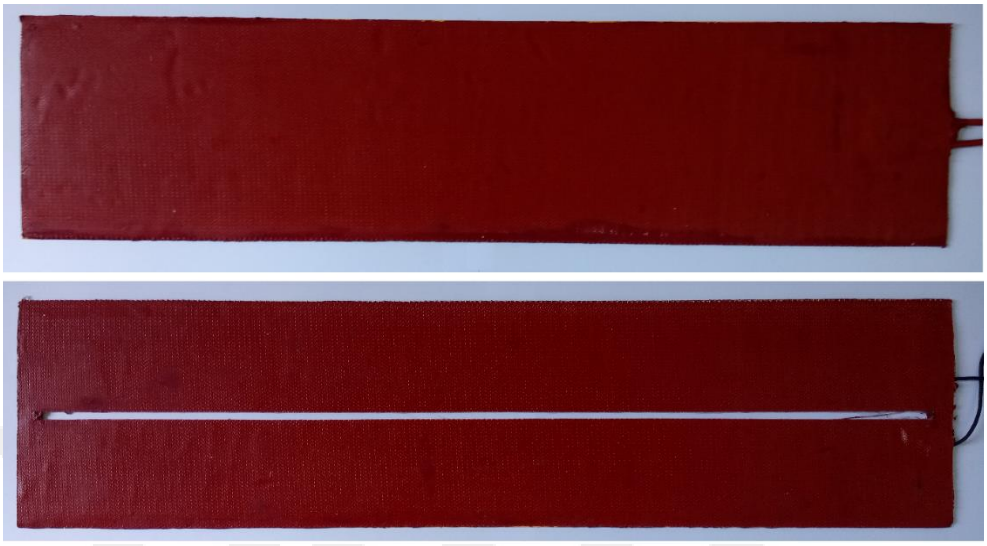

Figure 3.3. Flexible heaters are used to provide heat flux at test section walls.

Pulsator mechanism (see Figure 3.4) is consists of a rotating butterfly valve with the same diameter of the pipe, an electrical motor and a gearbox. The frequency of the pulsation is determined by the revolution of the valve disk per minutes. To isolate the water channel from the vibration created by an electrical motor, electrical motor and gearbox mounted on a support that has no contact with the table on which the water channel placed. A flexible coupling is used to connect the butterfly valve to the gearbox so that undesired bending forces caused by small deviations during assembly do not damage the valve and minimize the transmission of vibration to the pipe. In addition, the pipe is also connected to the water channel with a flexible hose(7).

$$u = \bar{u}\,(1 + A_p \sin(\Omega t)) \tag{3.1}$$

Here Ω represents angular frequency and it is equal to $2\pi F$. At the end of the line, water is collected at reservoir 2 (9), which is open to the atmosphere, and resent it back to reservoir 1 by using another centrifugal pump (10) located on the second line. A water cooler (12) is connected to the second line to remove the heat gain of water during the test section. However, since the cooler operates at a constant capacity that is higher than applied heat at the test section, a water heater (16) is placed in reservoir 2 to catch the thermal balance and obtaining constant temperature at the inlet of the test section.

Figure 3.4. Pulsator mechanism.

3.2. Grooved Channel Geometry and Temperature-Pressure Measurement

The schematic view periodically-grooved upper and lower walls are given in Figure 3.5. There are nine periods in each wall and a period with the length of L consisting of a groove section and a straight section that has the length of L_g and L_s

respectively. The depth of each groove is designated by *l*. The channel height designated by, *H* is 18mm, and the channel width designated by, *w* is 150mm. Three different test geometry configurations are created by shifting grooved walls. These configurations are symbolized as G_1, G_2, G_3 for no shifting, *L*/4 shifting, and *L*/2 shifting, respectively. Details about the sizes are given in Table 3.1. In the numerical part of the study, seven different groove aspect ratios are tested for no shifted wall configuration. The aspect ratio of grooves, n, is defined by dividing the groove depth, *l* to groove length, L_g, n= l/L_g. For six of them (n = 0.1, n = 0.2, n = 0.3, n = 0.4, n = 0.5, n = 0.6) groove length, Lg is constant but groove depth, *l* is changed however, for n = 0.1333 groove depth defined as equal the depth of n = 0.2 but groove length, L_g is extended by 50%.

Table 3.1. Parameters defining the grooved channel.

L/H	L_g/H	L_s/L_g	l/L_g
3.333	1.111	2	0.5

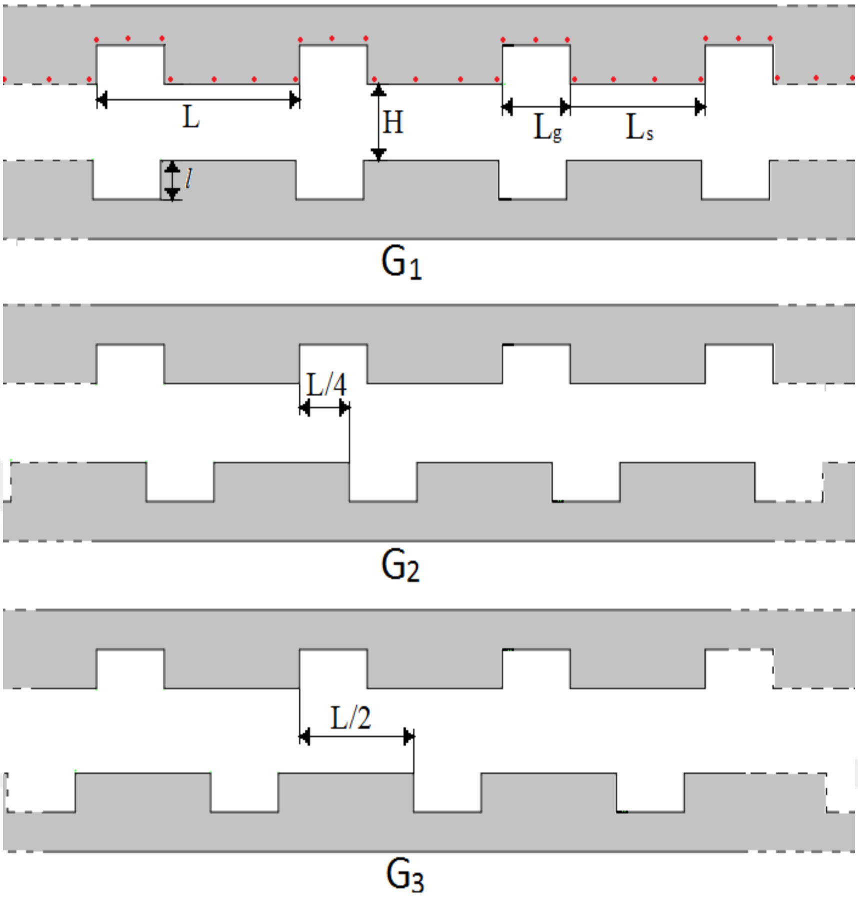

Figure 3.5. Illustration of the parameters defining the grooved channel.

K-type thermocouples measure wall temperature with 1 mm diameter placed in the drilled holes on the upper wall of the grooved channel and saved by the data logger (14). Locations of thermocouples are shown as red dots in Figure 3.5 for geometry G_1. Three thermocouples are located at the inlet of the test section in order to get the inlet temperature of the water. By adjusting the power of the water heater (16) in reservoir 2, the inlet temperature is set as 20^{o} C during all experiments. The temperature difference between the inner and outer surfaces of the insulation is also measured and heat loss from the test section is determined by calculating heat transfer through the insulation in order to check the validity of this heat loss determination method. A porous media placed at the outlet of the test section for uniformization of temperature profile and temperature of the water is measured at outlet thus heat gain of water passing through the test section is calculated. Finally, heat loss is determined by subtracting the heat gained by water from the adjusted wall heater power. By comparing the results, the validity of the first heat loss determination method is confirmed. However, since the calculation of heat loss from the temperature difference between inlet and outlet requires porous media at the outlet which means additional pressure drop and this method can be only used for low Reynolds numbers due to reducing inlet-outlet temperature difference. The first method is preferred for the determination of heat loss during experiments. Pressure drop through the grooved channel is obtained by using Aplisens APR-2000 ALW (11) differential pressure transmitter. Pressure taps with a diameter of 3 mm drilled at a location with1.5 cm away from the channel inlet and outlet. The pressure transmitter is connected to the taps by silicone hoses of the same length.

3.3. Data Reduction

Two times channel height H, and average inlet velocity, u_o are selected as reference length and velocity for the calculation of the Reynolds number, Re.

$$Re=\frac{\rho u_o 2H}{\mu} \tag{3.2}$$

Where "ρ" is density and "μ" is dynamic viscosity. Since temperature differentiation between inlet and outlet is not significant, thermophysical properties of water are determined according to inlet temperature 20^o C. The Prandtl number, Pr of water is equal to 7.01 at this temperature (Çengel and Cimbala). The average Nusselt number, Nu, is calculated as follows;

$$Nu=\frac{h\,2H}{\lambda} \tag{3.3}$$

Here h and λ correspond to the convection coefficient and thermal conductivity of water respectively. Convection coefficient, h is determined as;

$$h=\frac{\dot{q}}{T_w\text{-}T_o} \tag{3.4}$$

Where T_w is average wall temperature, T_o is the inlet water temperature and $\dot{q}$ represents heat flux.

$$\dot{q}=(q\text{-}q_{loss})/A_s \tag{3.5}$$

Where q is the adjusted power of the wall heater, and it is calculated by Eq. (6), q_{loss} is the heat loss to the environment, and A_s is the outer surface area of the heated wall.

$$q = V.I \tag{3.6}$$

The voltage and the current applied to the wall heaters are measured by voltmeter and ammeter during the experiments.The friction factor is determined by using equation (7).

$$f=\frac{2\,\Delta P\,2H}{\rho\,S\,u_o^2} \tag{3.7}$$

In equation (7), ΔP represents pressure drop across the test section, ρ is the density of the water, and S is the total length between inlet and outlet pressure measurement locations.

The thermal performance factor, TPF, is a parameter that considers heat transfer enhancement and pressure drop rise compared to the smooth channel together and gives information about the net energy gain of the system. In Eqn. (8), subscript 'o' represents the smooth channel.

$$TPF = \frac{Nu/Nu_s}{(f/f_s)^{1/3}} \tag{3.8}$$

3.4. Validation of Experimental Setup and Uncertainty Analysis

Heat transfer and pressure loss experiments are performed for a smooth channel for validation of the experimental setup. To this end, a test section with flat upper and lower walls is manufactured. Experiments are carried out for the same heating power and inlet water temperatures as grooved channel experiments. Wall temperature measurement is done at a location close to the outlet of the test section to ensure thermally fully developed conditions. Instead of inlet temperature, the bulk temperature is used as a reference temperature for calculation of the experimental Nusselt numbers during the validation to be able to compare it with Nusselts values calculated by the Gnielinski equation. The bulk temperature calculated as follows;

$$T_b = T_i + \frac{\dot{q}wS}{\dot{m}C_p} \tag{3.9}$$

In equation above $\dot{m}$ and C_p represents mass flow rate and specific heat capacity of water, respectively. S is the distance between the inlet of the channel and the location of where wall temperature measurement is done. Reynolds number, Re is varied between $4x10^3$ and $8x10^3$. Comparison of the results with the empirical equation of the Gnielinski (Eqn. (10)) is shown in Figure 3.6a. In addition, good agreement between friction factors calculated from measured pressure drop and values calculated from Petukhov equation (Eqn. (11)) is obtained as it is seen in Figure 3.6b.

$$\left(Nu = \frac{(f/8)Re\,Pr}{1.07 + 12.7(f/8)^{1/2}(Pr^{2/3} - 1)}\right) \tag{3.10}$$

$$f = (0.79\ \ln Re - 1.64)^{-2} \tag{3.11}$$

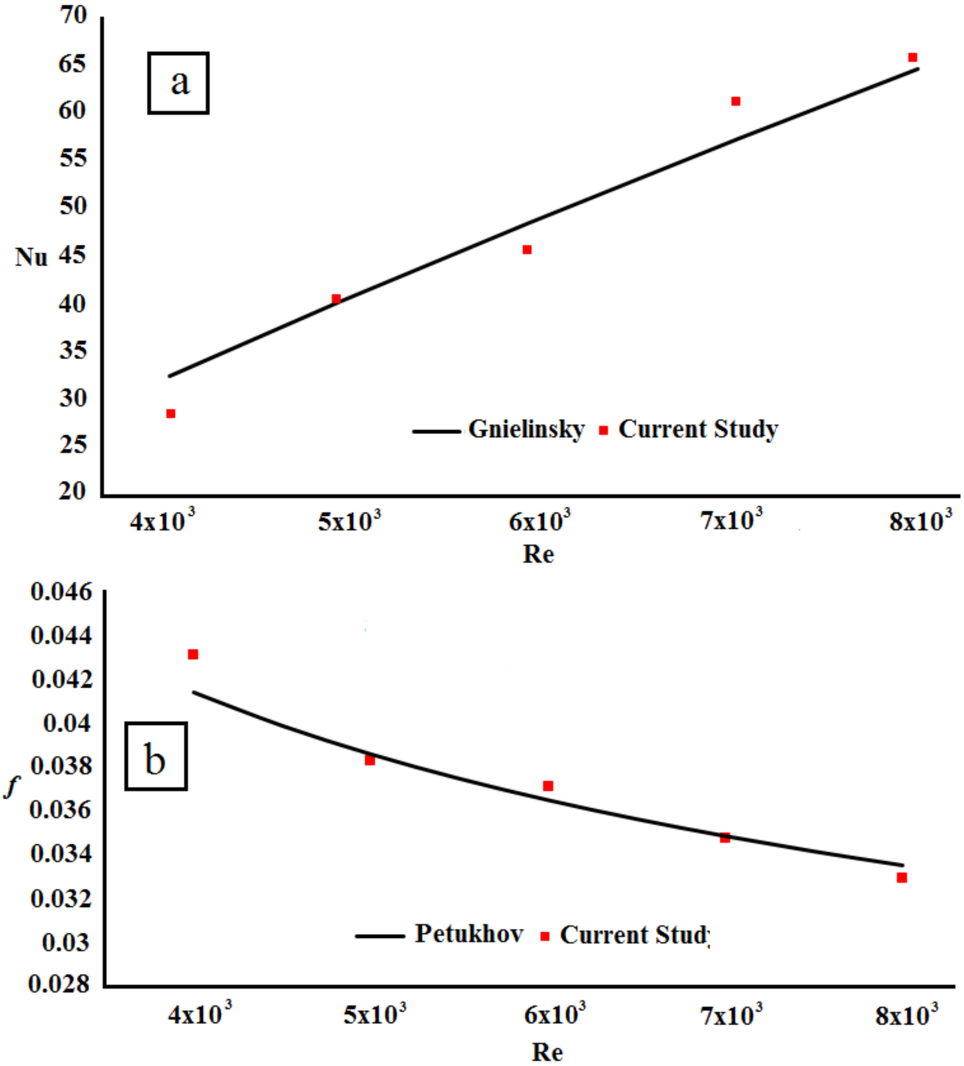

Figure 3.6. Comparison of the results with the empirical equation of the Gnielinski and Petukhov for validation.

Kurtulmus et al. (2020) carried out an uncertainity analysis by using the equations below for the same experimental setup. They found out that uncertainities are at a rate of 0.95%, 10.53%, 2.85% for Re, Nu_{avg} and f respectively.

$$\frac{\delta_{Re}}{Re}=\mp\sqrt{\left(\frac{\delta_U}{U}\right)^2+\left(\frac{\delta_H}{H}\right)^2} \tag{3.12}$$

$$\frac{\delta_{Nu_{avg}}}{Nu_{avg}}=\mp\sqrt{\left(\frac{\delta_{\dot{q}}}{\dot{q}}\right)^2+\left(\frac{\delta_H}{H}\right)^2+\left(-\frac{\delta_{T_w\text{-}T_i}}{T_w\text{-}T_i}\right)^2} \tag{3.13}$$

Here $\frac{\delta_{T_w\text{-}T_i}}{T_w\text{-}T_i}=\mp\sqrt{\left(\frac{\delta_{T_w}}{T_w\text{-}T_i}\right)+\left(\frac{\delta_{T_i}}{T_w\text{-}T_i}\right)^2}$

$$\frac{\delta_f}{f}=\mp\sqrt{\left(\frac{\delta_{\Delta P}}{\Delta P}\right)^2+\left(\frac{\delta_{L_S}}{L_S}\right)^2+\left(\frac{3\delta_H}{H}\right)^2+\left(\frac{2\delta_{Re}}{Re}\right)^2} \tag{3.14}$$

3.5. Flow Visualization Experiments

Hydrodynamics in the grooved channel is visualized non-intrusively by theparticle image velocimetry(PIV) method using the DANTEC PIV system. In order to illuminate the area of interest by the laser source below the channel, a test section with plexiglass grooved walls(Figure 3.7) is manufactured. The illuminated area is located in the middle of the channel width to avoid the effect of side walls. The area that includes both upper and lower grooves is determined as the field of view as it is shown in Figure 3.8 and the CCD camera equipped with a 105mm lens positioned to see this area perpendicularly(see Figure 3.9). In order to take data from different grooves, a traverse mechanism is used that enables the movement of the camera along the test section while keeping the distance between the camera and the channel constant. Two ND:Yag laser units create a double-pulsed laser. The time interval between each pulse is varied between 1800-3750 µs depending on the Reynolds number, and a synchronizer is used to match the timing of laser pulses and the CCD camera. Also 12 µm spherical particles coated with silver are seeded to water. Particle concentration in water is determined so that the number of particles in the interrogation window is between 15 and 20. These particles are naturally buoyant and move in accordance with flow motion in the grooved channel.

Figure 3.7. The test section made of transparent grooved walls.

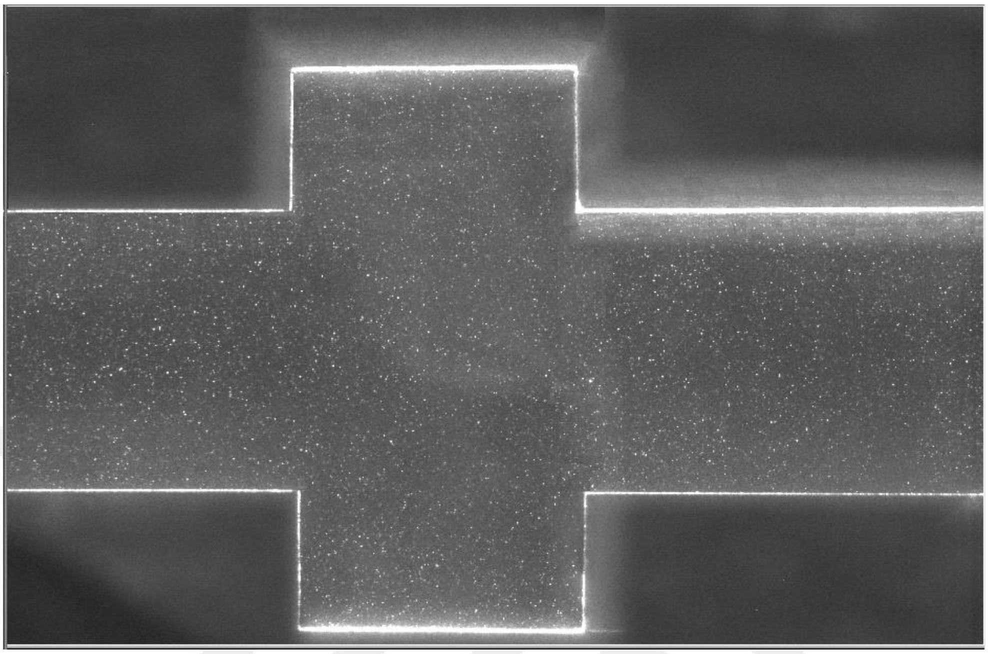

Figure 3.8. The raw image taken by a CCD camera.

Stokes number is a key parameter in terms of the capability of the seeded particles to track the vortical flow movement in the flow field correctly.The limit of Stokes number is dependent on the geometry in which flow passes through and sharp changes in flow velocity. The definiton of Stokes number is as follows;

$$S_t = \frac{\tau_p U_\infty}{d_{particle}} \qquad (3.15)$$

In this equation U_∞ is free-stream velocity, τ_p is the relaxation time for particles, and $d_{particle}$ is the diameter of particle. The relaxation time is given as;

$$\tau_p = \frac{\rho_{particle} d^2_{particle}}{18 \rho_{fluid} \varphi_{fluid}} \qquad (3.16)$$

Here, φ_{fluid}, is the kinematic viscosity of the fluid. When $S_t >> 1$, particles deviate around obstacles where streamlines bend; however, for $S_t << 1$, particles will track the streamlines with a 1% deviation.

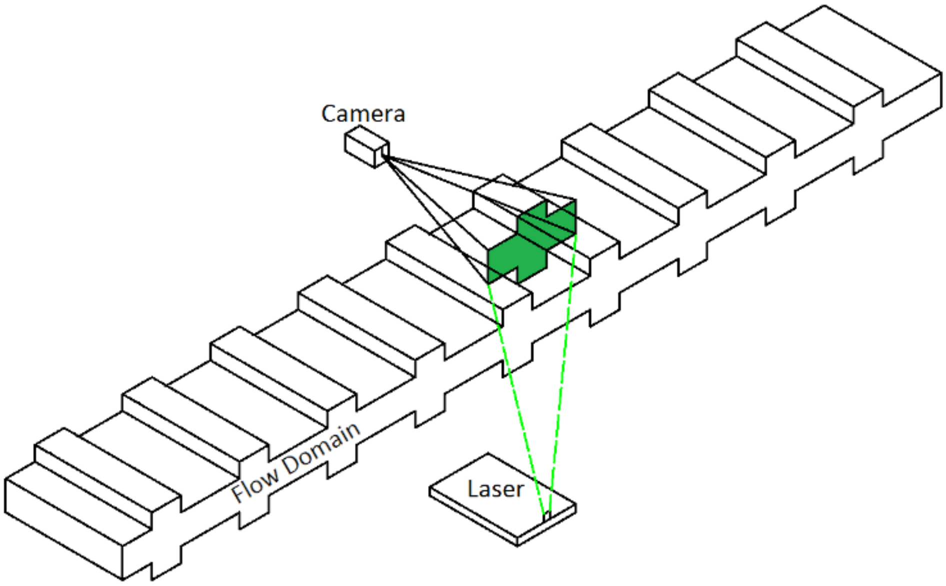

Figure 3.9. Schematic view of the test setup.

3.5.1. Correlation Process

Measurement with PIV is based on the determination of the distance that particles travel for a ceartain duration of time. Having the knowledge about particles displacement length and time passed during the displacement enables calculation of velocity vector. Obtaining velocity readings with PIV involves a procedure called the correlation process. Auto-correlation and cross-correlation are two different basic approaches for the correlation process. An ensemble of particles is exposed to laser light multiple times during a single record in the autocorrelation method. However, for the cross-correlation method, a pair of successive images are taken, and particles are exposed to laser light with a single time during each record. Cross-correlation is more advantageous than the auto-correlation since a pair of images contain larger information than a single image; therefore, spatial resolution is larger in the cross-correlation method. But its disadvantage is a requirement for the acquisition of two successive images in a very short time interval. This disadvantage has been remedied with the advent of CCD cameras and dual cavity Nd:YAG lasers. Therefore cross-correlation method is the preferable one in PIV systems. In cross-correlation analysis, images are subsampled using interrogation windows shown in Figure 3.10; and then interrogation areas in two frames are cross-correlated to each other pixel by pixel. As a result of this process, a signal peak was obtained which identifies common particle displacement, dx and dy. Finally, bu using calibration parameters, velocity is derived from displacement data, dx and dy .

Another correlation method called adaptive-correlation enhances the ability of the capturing a larger area with increased dynamic range and accuracy. In this method, an offset between interrogation windows of two frames is determined as an initial guess, and a vector field is calculated. After that, an obtained vector field is validated and used as a new gusess for window offset. The process runs iteratively, and the size of the interrogation area is reduced between each iterations. By using the shifted windows, it is possible to capture the particle images that left the interrogation area between two laser pulses. Those particle images are called “in-plane dropout” which reduces the signal’s strenght and succesful vectors. The use of adaptive-correlation strengthens the signal by capturing in-plane drop out. In addition, it provides a refinement for the interrogation area. Due to its advantages over cross-correlation, adaptive-correlation is applied in this study by using Dantec DynamicStudio Software.

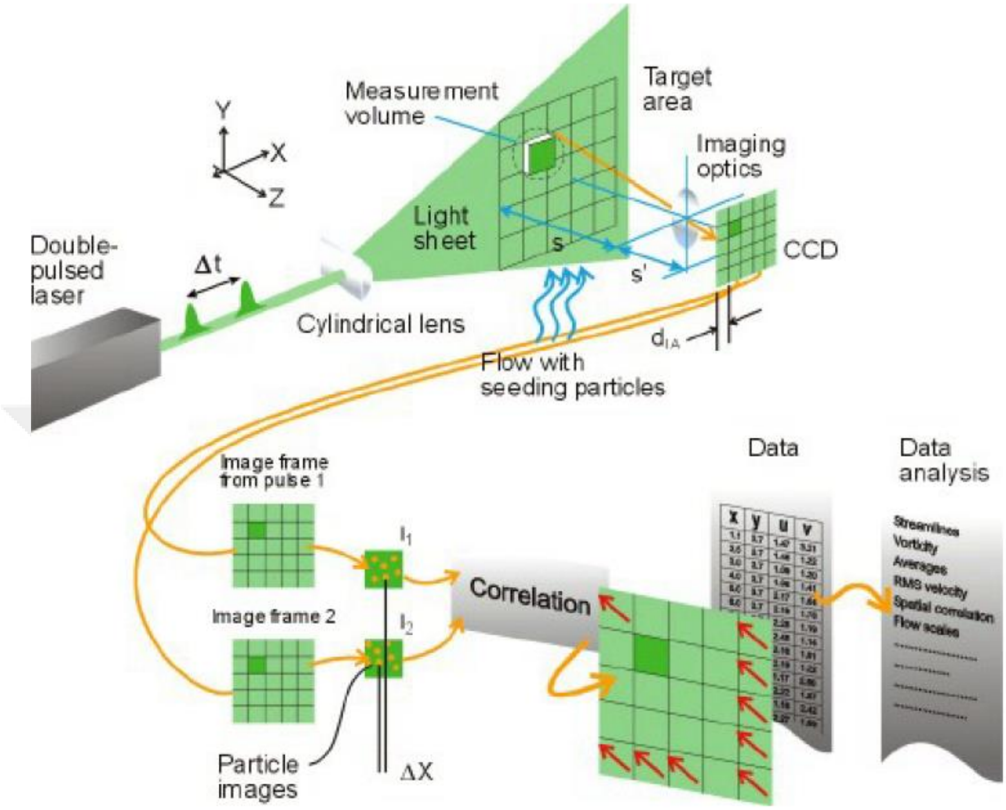

Figure 3.10. Schematic summary of PIV measurement process.

3.5.2. Post Processing

Raw vector field data obtained due to the adaptive correlation is post processed for removing inappropriate vecors. CLEANVEC software is employed for this purpose. CLEANVEC software uses Fourier statistical filters for removing bad vectors. These filters are;

- Absolute range filter
- RMS tolerance filter
- Magnitude difference filter
- Quality filter

The gaps in the vector field resulting in the cleaning process are filled with interpolated vectors by using the bilinear least-square fit method(Westerweel 1994). Finally, the smoothing process used in the study of (Landreth and Andrian 1989) is applied to the velocity field. The vorticity field is calculated by the circulation method. Time-averaged and RMS variables are calculated from PIV images as follows;

Streamwise and spanwise velocity:

$$\bar{u} = \frac{1}{N}\sum_{n=1}^{N} u_n(x,y) \tag{3.17}$$

$$\bar{v} = \frac{1}{N}\sum_{n=1}^{N} v_n(x,y) \tag{3.18}$$

Vorticity:

$$\bar{w} = \frac{1}{N}\sum_{n=1}^{N} \omega_n(x,y) \tag{3.19}$$

Averaged Reynolds stress:

$$\overline{u'v'} = \frac{1}{N}\sum_{n=1}^{N} [u_n(x,y)-\bar{u}(x,y)]\,[v_n(x,y)-\bar{v}(x,y)] \tag{3.20}$$

In the above equations, N represents the total number of images, and n is instantaneous images.

For the pulsating flow case since the mean velocity of the flow changes in time, the use of time-averaged velocity in the determination of fluctuating components will cause misleading results, i.e., as the instantaneous velocity of the flow diverges from the time averaged velocity, the fluctuating component calculated from $u' = u_n - \bar{u}$ increases. However, the fluctuation appears to be increased is because of the increase in the difference between the instantaneous velocities and time-average velocities due to the periodic velocity changes rather than increasing turbulence fluctuation. Therefore, different phases of the pulsation must be evaluated individually. For this purpose, mean velocity data of the flow along a vertical line is plotted with respect to time by using 1000 images. Images correspond to phases that will be investigated are picked out with the help of instantaneous velocity distributions. After images are re-grouped for each phases, averaged Reynolds stress contours are obtained by applying a post processing algortihm that employs the Eq. (18). For this calculation average velocity of each phase is used instead of time-averagde velocity. Phase averaging process is applied for three phases of the pulsation which are low velocity phase ($\Omega t = 3\pi/2$), acceleration phase ($\Omega t = 2\pi$) and peak velocity phase ($\Omega t = 5\pi/2$). In addition to turbulence statistics streamlines are also plotted for each phases.

3.5.3. Parameters Used in PIV Experiments

Laser units used in the experiment have 120 mJ maximum energy output and 532 nm wavelength.The resolution of an 8-bit CCD camera is 1600x1200 pixels, and 15 frames are captured per second. An interrogation area consists of 32x32 pixels is used for the frame to frame correlation with 50% overlap. A total of 3626 velocity vectors are obtained as a result of image processing. Westerweel reported 2% uncertainty for similar PIV configfurations used in this study.

3.6. Numerical Method

3.6.1. Governing Equations

Flow and convective heat transfer through the grooved channel are numerically simulated by using Ansys Fluent 17.2 CFD software. The flow domain including the calming inlet section, grooved channel, and calming outlet section, are modeled two-dimensionally according to identical sizes in experiments. Similar to experimental study, thermophysical properties of water set as constant also for numerical simulations. Moreover, it is assumed that there is no heat transfer

through thermal radiation, and the effect of gravity is neglected. Simulations are performed only for steady inlet velocity conditions and Reynolds numbers ranging from $3x10^3$ to $6.5x10^3$. Based on the assumptions above, governing equations in tensor form are as follows (Benim et al. (2011) & Farzad et al.(2011));
Continuity equation:

$$\frac{\partial}{\partial x_i}(\rho\bar{u}_i)=0 \qquad (3.21)$$

Momentum equation:

$$\frac{\partial}{\partial t}(\rho\bar{u}_i)+\frac{\partial}{\partial x_j}(\bar{u}_i\bar{u}_j)=-\frac{\partial\bar{p}}{\partial x_i}+\frac{\partial}{\partial x_j}\left[(\mu+\mu_t)\left(\frac{\partial\bar{u}_i}{\partial x_j}+\frac{\partial\bar{u}_j}{\partial x_i}\right)\right]-\rho\overline{u_i'u_j'} \qquad (3.21)$$

Energy equation:

$$\frac{\partial}{\partial t}\bar{T}+\frac{\partial}{\partial x_j}(\rho\bar{u}_i\bar{T})=\frac{\partial}{\partial x_j}\left[(\Gamma+\Gamma_t)\left(\frac{\partial\bar{T}}{\partial x_j}\right)\right] \qquad (3.23)$$

$$-\rho\overline{u_i'u_j'}=(\mu_t)\left(\frac{\partial u_i}{\partial x_j}+\frac{\partial u_j}{\partial x_i}\right) \qquad (3.24)$$

For the sake of keeping equations short Einstein summation convention is used in Eq. (19-26). In these equations $u_1 = u$, $x_1 = x$, $u_2 = v$, $x_2 = y$.

μ_t is expressed as;

$$\mu_t=\rho C_\mu\frac{k^2}{\varepsilon} \qquad (3.25)$$

where k is the turbulent kinetic energy and ε is the dissipation rate of turbulent kinetic energy, and they are modeled by Eqn. (17) and Eqn. (18). Eimsa-Ard and Promvonge (2008) tested four different two-equation turbulence models and reported that k- ε model provide provide more accurate results in grooved channel therefore k- ε is used in current study.

$$\frac{\partial}{\partial t}(\rho k) + \frac{\partial}{\partial x_i}(\rho k \acute{u}_i) = \frac{\partial}{\partial x_j}\left[\left(\mu + \frac{\mu_t}{\sigma_k}\right)\frac{\partial k}{\partial x_j}\right] + G_k - \rho\varepsilon \tag{3.26}$$

$$\frac{\partial}{\partial t}(\rho \varepsilon) + \frac{\partial}{\partial x_i}(\rho \varepsilon \acute{u}_i) = \frac{\partial}{\partial x_j}\left[\left(\mu + \frac{\mu_t}{\sigma_\varepsilon}\right)\frac{\partial \varepsilon}{\partial x_j}\right] + C_{1\varepsilon}\frac{\varepsilon}{k}G_k - C_{2\varepsilon}\rho\frac{\varepsilon^2}{k} \tag{3.27}$$

In the equations above, G_k represents the generation rate of the turbulent kinetic energy, and it is described as;

$$G_k = -\rho\overline{u_i' u_j'}\frac{\partial u_j}{\partial x_i} \tag{3.28}$$

Γ and Γ_t in Eqn.(14) corresponds molecular thermal diffusivity and turbulent thermal diffusivity and written as;

$$\Gamma = \frac{\mu}{Pr},\ \Gamma_t = \frac{\mu_t}{Pr_t} \tag{3.29}$$

The enhanced wall treatment method is used for near-wall modeling. Model constants used in the equations above are given in Table 3.2.

Table 3.2. Empirical constants for the standard k-ε model.

$C_{1\varepsilon}$	$C_{2\varepsilon}$	σ_k	σ_ε	Pr_t	$C\mu$
1.44	1.92	1.0	1.3	0.9	0.09

3.6.2. Boundary Conditions

The velocity profile of flow at the inlet of the solution domain is uniform ($u = u_{o,}$, $v = 0$), and its temperature is constant ($T = T_{in}$). No-slip condition($u = v = 0$) is available for all walls of the solution domain. Walls of the test section are subjected to constant heat flux$\left(\frac{\partial T}{\partial y}=\dot{q}\right)$ while calming sections walls are adiabatic $\left(\frac{\partial T}{\partial y}=0\right)$. Velocity and temperature gradients at the outlet of the domain are set as zero $\left(\frac{\partial u}{\partial x}=0, \frac{\partial v}{\partial X}=0, \frac{\partial T}{\partial x}=0\right)$.

3.6.3. Mesh Independence and Solution Procedure

Four different element numbers are tested for mesh independency study, and results are presented in Table 3.3. As it is seen from the table, increasing the element number beyond the 78933 does not cause significant variation in the Nusselt number and friction factor. Since the use of more element numbers increases solution time, there is no need to use more elements than 78933. Mesh density is higher near boundaries in order to fulfill the $y+ < 1$ requirement of enhanced wall treatment modeling. Structure of the mesh used in the study is shown in Figure 3.11.

Table 3.3. Results of mesh independency study.

Element Number	Nu	f
50129	57.34	0.1036
64692	61.13	0.1106
78933	65.58	0.1255
95114	66.49	0.1296

Second-order upwind scheme and least-squares cell-based method are used for discretization of convection and gradient terms, respectively. Additionally, the transient formulation is done by second-order implicit method. Coupling between pressure and velocity is obtained by the SIMPLE algorithm. Convergence criteria that stop iterations at each time step are set $1x10^{-8}$ for the energy equation and $1x10^{-5}$ for other variables. Simulations are stopped when observed temperature and velocity reach statistically steady.

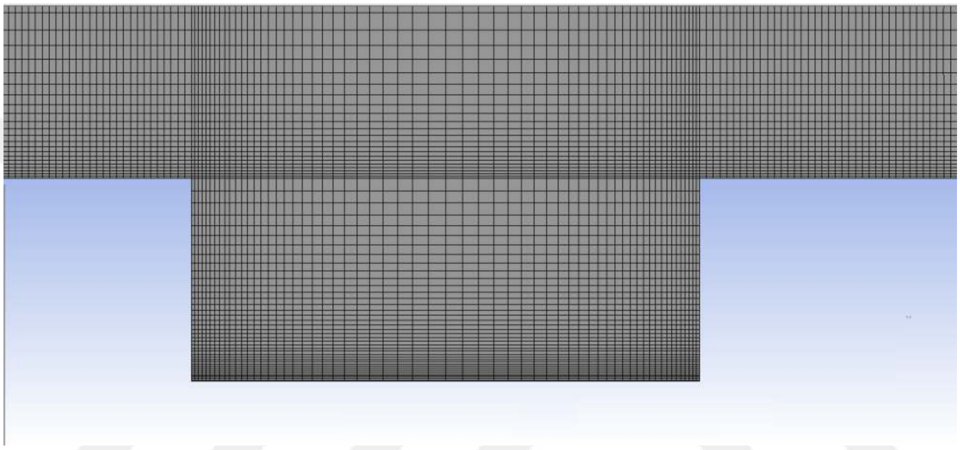

Figure 3.11. Structure of the mesh used in numerical study.

4. RESULTS AND DISCUSSION

4.1 Quantitative Analysis of Steady Flow

The data relating to the flow hydrodynamics obtained with the PIV technique are presented in this section. In addition, it was determined by using the PIV method that the current experimental setup caused 5.2 percent turbulence intensity at the entrance of the test section.

Time-averaged streamlines are presented in Figure 4.1 for the 2nd and 8th groove in order to show flow patterns in the grooved channel. The figure indicates recirculation eddies dominate the separated flow inside grooves. These eddies rotate clockwise and counterclockwise in lower and upper grooves respectively. Large-scale vorticities nearly cover the whole cross-sections of grooves, their focal points occur close to the downstream wall of grooves, and a region where the flow movement is very slow(almost stagnant) takes a place between the primary eddy and upstream wall of the groove for the Reynolds number, *Re* of $2x10^3$. A secondary recirculation eddy that rotate the opposite direction of the primary one get becomes more apparent for $Re = 4x10^3$ and a similar pattern is observed for $Re = 5.5\ x10^3$. The secondary eddy reduces the size of the main eddy, however, it also indicates an increase of the circulating flow velocity at the region where flow is almost stagnant, when the $Re = 2\ x10^3$. In addition, no significant difference in flow patterns is observed between the 2nd groove and the 8th groove. Quantitative information about the wake flow in the area of grooves and the mainstream can be obtained from Figure 4.2. In this figure time-averaged streamwise velocity, $\bar{u}$ profiles are plotted for three different locations inside the groove by using CFD and PIV data. Good agreement between PIV and CFD results is obtained for fully turbulent Reynolds numbers however selected turbulence model can not estimate the flow velocities in the laminar-turbulent transition regime well ($Re < 3x10^3$).

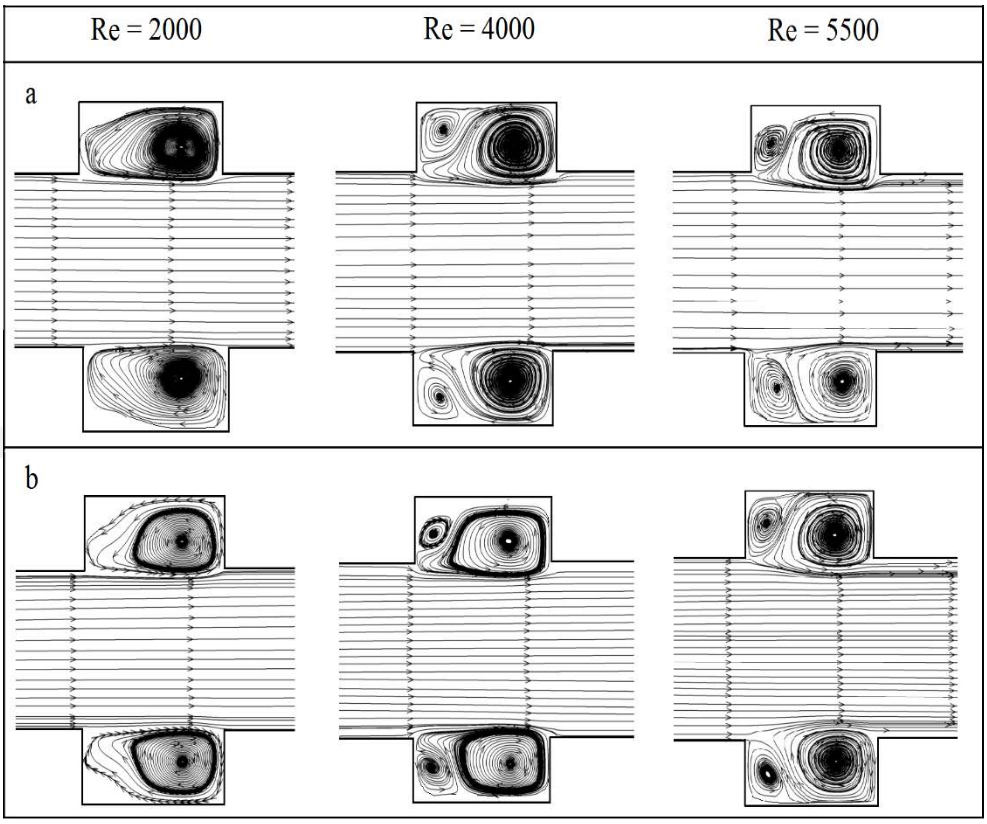

Figure 4.1. Time-averaged streamlines for different Reynolds numbers at a) groove 2 and b) groove 8.

As it is seen in Figure 4.2, there is a significant velocity magnitude difference between flow in the groove and the mainstream. Furthermore, negative velocity values are seen inside the groove because of the reverse flow motion as a part of the recirculation and the lowest negative velocity value is detected at $L_g/2$. Velocity profiles show different behavior at $L_g/5$ for *Re* = 2 x10^3 compared to higher Reynolds numbers, *Re*. The reason for this situation is the strengthening of secondary recirculation eddy in higher Reynolds numbers, *Re*. The rotational direction of the secondary recirculation eddy causes positive streamwise velocity values in a larger region near the groove wall. Like similarity in flow pattern shown in Figure 4.1, streamwise velocity profiles also indicate a well agreed quantitative similarity between 2nd and 8th grooves.

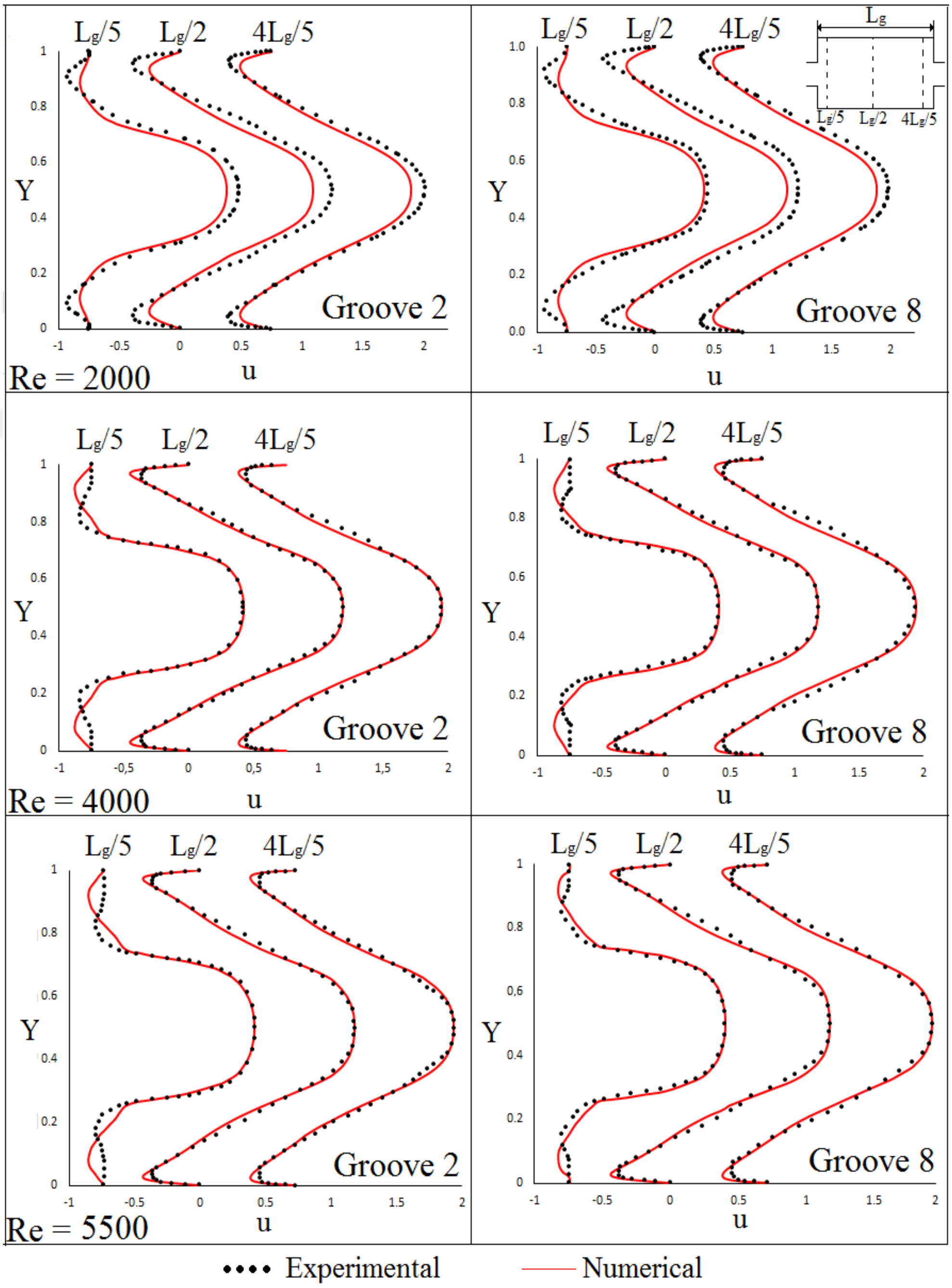

Figure 4.2. Comparisons of experimental and numerical time-averaged velocity profiles in the cross-section of grooves for different Reynolds numbers

The instantaneous velocity vector field and velocity magnitude contour are given for the 8th groove in Figure 4.3 to show the evolution of eddies in time and interaction between these eddies and mainstream. Here velocity magnitude is calculated as; $u_{mag} = \sqrt{u^2 + v^2}$. Since there is a significant magnitude difference between vectors at higher and lower velocity regions, the plotting area is focused on to lower groove to make small vectors in the groove clearly visible. An instant in which there is no mass transfer between recirculating flow in the groove and main flow is shown in Figure 4.3(a) for *Re* = $5.5\text{x}10^3$ and this instant is tagged as 't = 0'. When t is equal to 0 the shape of the primary recirculating eddy is looked like the one in Figure 4.1(c), in addition, the velocity of the secondary recirculating eddy is markedly lower than the primary recirculating eddy. Considering Δt is the time between two images taken by the camera, for t = 3Δt, the flow enters the groove near the trailing edge and deforms the primary recirculating eddy with its high velocity. At this instant incoming flow does not have any influence on the secondary recirculating eddy. When t becomes 5Δt, it is seen that the incoming flow with high momentum continues its circulation in the groove, and it also accelerates the rotation of the secondary recirculating eddy. It is observed that the primary recirculation eddy, whose focal point in the previous stage was suppressed by the flow entering the groove, moves up again. In the final stage (Figure 4.3(d)), flow recirculated in the groove rejoins to the mainstream from the downstream half of the groove, and secondary recirculation eddy loses its momentum. The distribution of velocity vectors at two distinct instants is presented in Figures 4.3(e) and (f) for Reyolds number, *Re,* of $2\text{x}10^3$. In these figures larger vector scale is used compared to *Re* = $5.5\text{x}10^3$ condition in order to magnify small scale vectors due to low velocity in *Re* = $2\text{x}10^3$. As seen from the figure flow structure inside the groove is almost similar for t= 0 and t = 5Δt. Furthermore, no massive fluid transfer occurs between flow in the groove and the mainstream. A similar flow pattern is kept for all instants; therefore, no more vector images are added for Re = $2\text{x}10^3$.

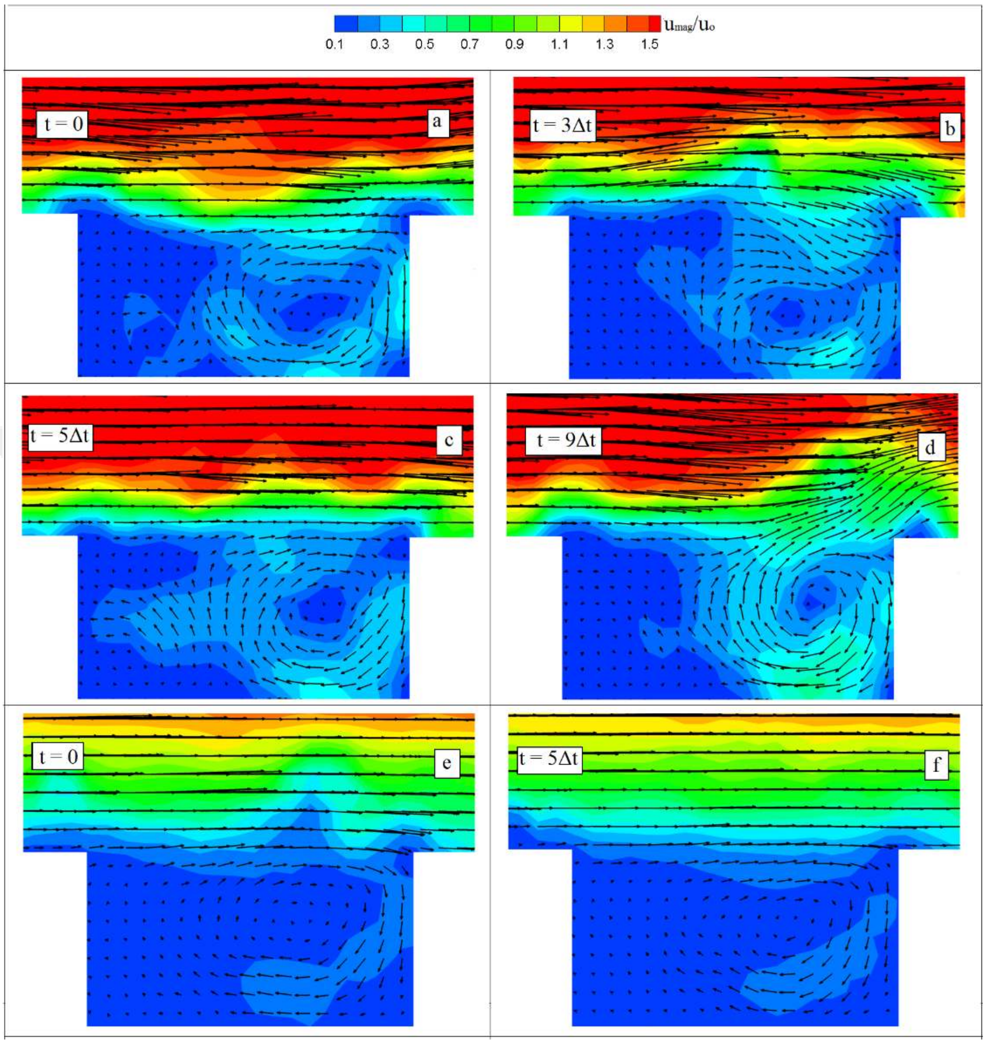

Figure 4.3. Velocity vectors for different instants at Re = $2x10^3$ and Re = $5.5x10^3$.

Vorticity, ω contours corresponding instants given in Figure 4.3 are demonstrated in Figure 4.4. As expected, the magnitude of instantaneous vorticity, ω concentrations is high near the channel surfaces along with shear layers. These instantaneous vorticity, ω concentrations are continuously interacted with the separated flow region in the groove and ensure the continuation of mass transfer between those two regions. If the negative vortical area on the lower groove is observed at each instant it can be seen that for t = 0 the intense vorticity, ω region is limited between the mouth of the groove and the central axis of the channel. When t is equal to 3Δt, the high vorticity, ω penetrates the groove space near the downstream wall and at the next stage (t = 5Δt) intensity of the positive vorticity, ω region where secondary circulation bubble exist, increases. Finally, the negative vorticial flow diffuses into the core flow with transferring mass from the groove region to the mainstream. Similar phenomena are observed in the study of Chang et. al. (2006) The behavior of high vorticity, ω regions near upper and lower grooves are different at each instant, so it can not be said that vortex shedding occurs simultaneously at upper and lower grooves. The process showed in Figure 4.4(a)-Figure 4.4(d) indicates the presence of good entrainment for the flow in the grooved channel. However similar entrainment is not observed for *Re* = $2x10^3$ (Figure 4.4(e) and Figure 4.4(f)). The intensity of the vorticity, ω is low in this Reynolds number, *Re* and since the interaction of recirculation eddies in groove and mainstream is limited, the vorticial region does not spread over the groove space and core flow region.

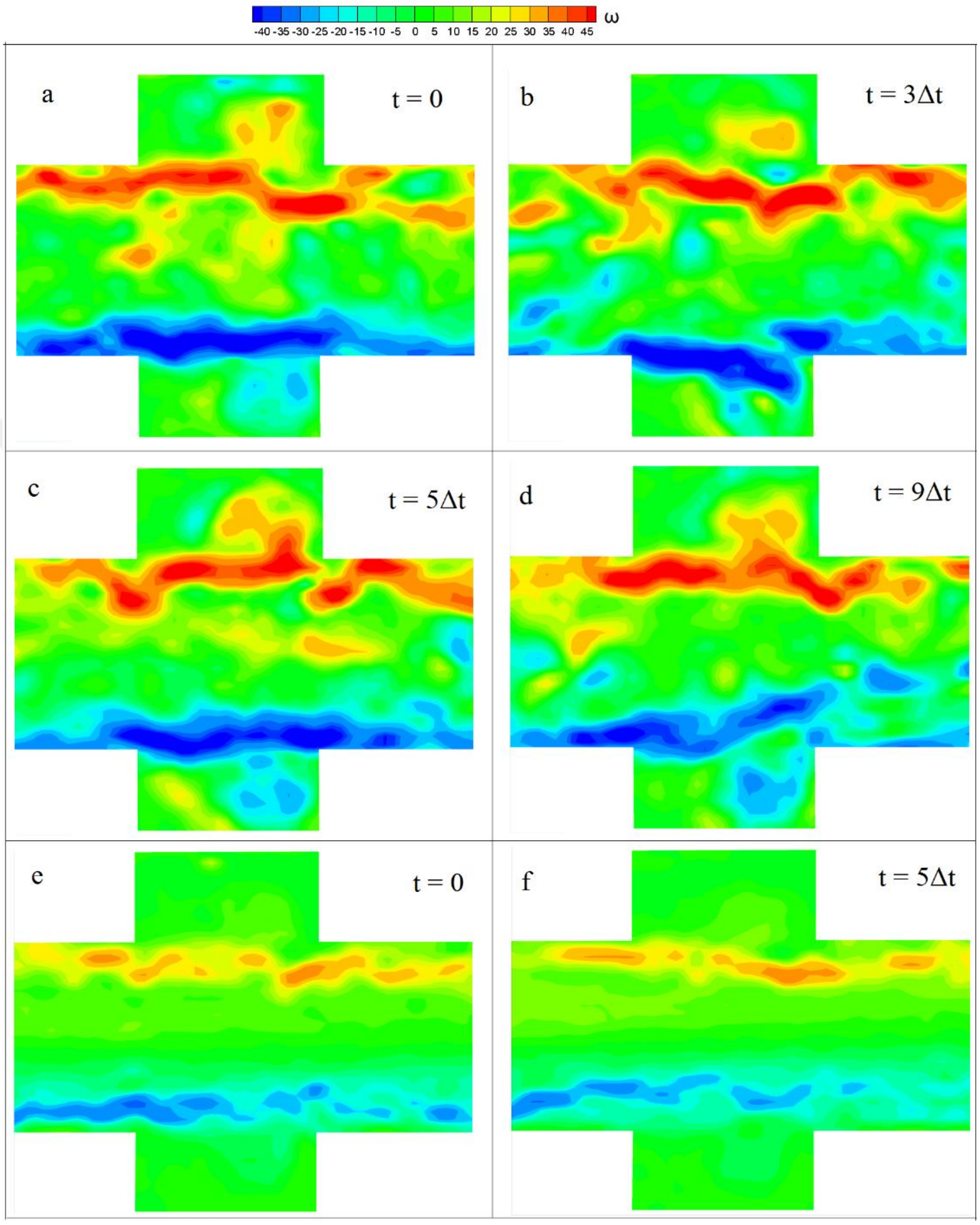

Figure 4.4. Instantaneous vorticity contours for Re = $2x10^3$ and Re = 5.5x10.

Time-averaged non-dimensionalized Reynolds stress, $\overline{u'v'}/u_o^2$ is presented in Figure 4.5 for 2nd, 5th and 8th grooves for Reynolds numbers, *Re* of 2x10^3, 4x10^3, and 5.5x10^3. Lines separating the levels of Reynolds stress, $\overline{u'v'}/u_o^2$ are solid for positive values and dashed for negative values. Contour maps indicate Reynolds stress, $\overline{u'v'}/u_o^2$ intensification in a separated shear layer which means fluctuations are amplified in this region. The peak point of the Reynolds stress, $\overline{u'v'}/u_o^2$ is close to the middle of the groove at *Re* = 2x10^3 however it shifts in a downstream direction with the increase of the Reynolds number, *Re*. This is because, in addition to small-scale turbulent structures, massive flow motions occur between the mainstream and the groove at the downstream half of the groove. Moreover, Reynolds stress values are low for the area in the groove when the Reynolds number, *Re* is equal to 2x10^3, it gets higher for *Re* = 4x10^3 yet more evident Reynolds stress, $\overline{u'v'}/u_o^2$ propagation is observed in the groove for Re = 5.5x10^3.

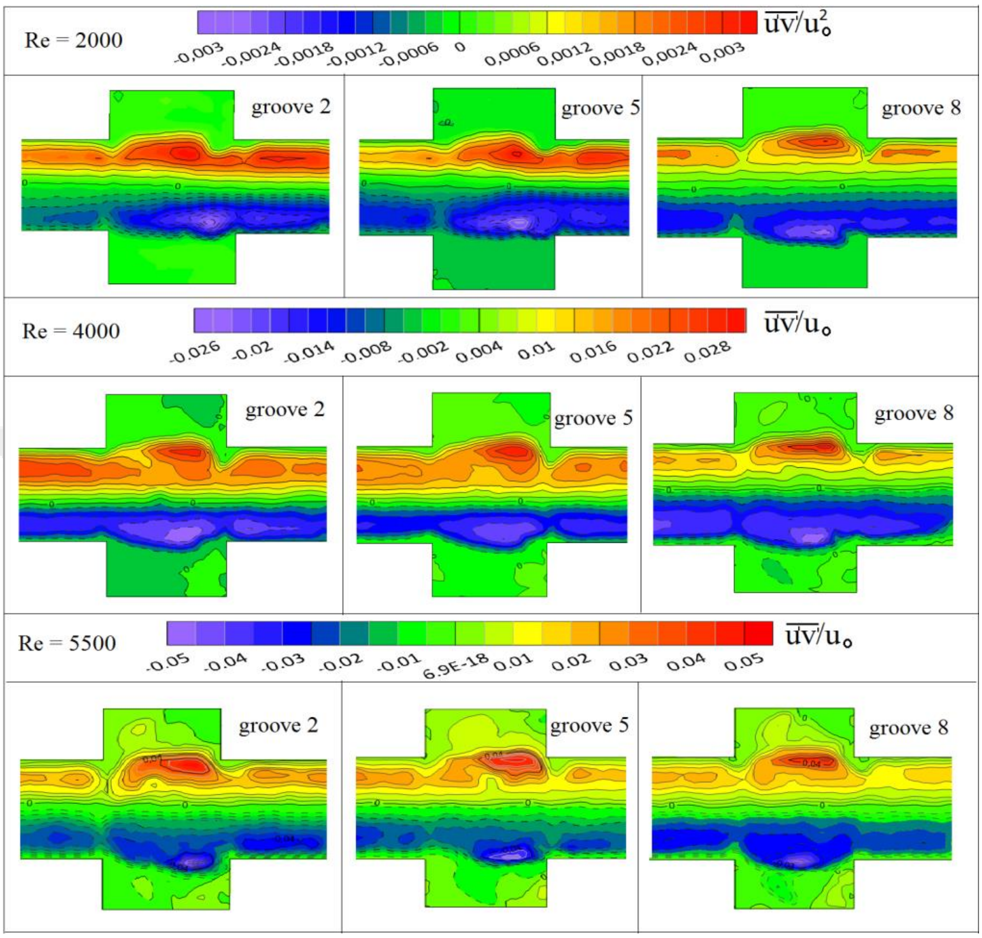

Figure 4.5. Patterns of Reynolds stress in different grooves for Reynolds numbers of $2x10^3$, $4x10^3$ and $5.5x10^3$.

Dimensionless Turbulent kinetic energy, *TKE* is also an important indicator for the mixing process. The TKE is nondimensilosized dividing u_o^2In Figure 4.6 *TKE* contours are plotted for the same Reynolds numbers, *Re* and grooves given in Figure 4.5, and the following formula is used for the calculation of *TKE* values.

$$TKE = \frac{3}{4}(\overline{u'u'} + \overline{v'v'})/u_o^2$$

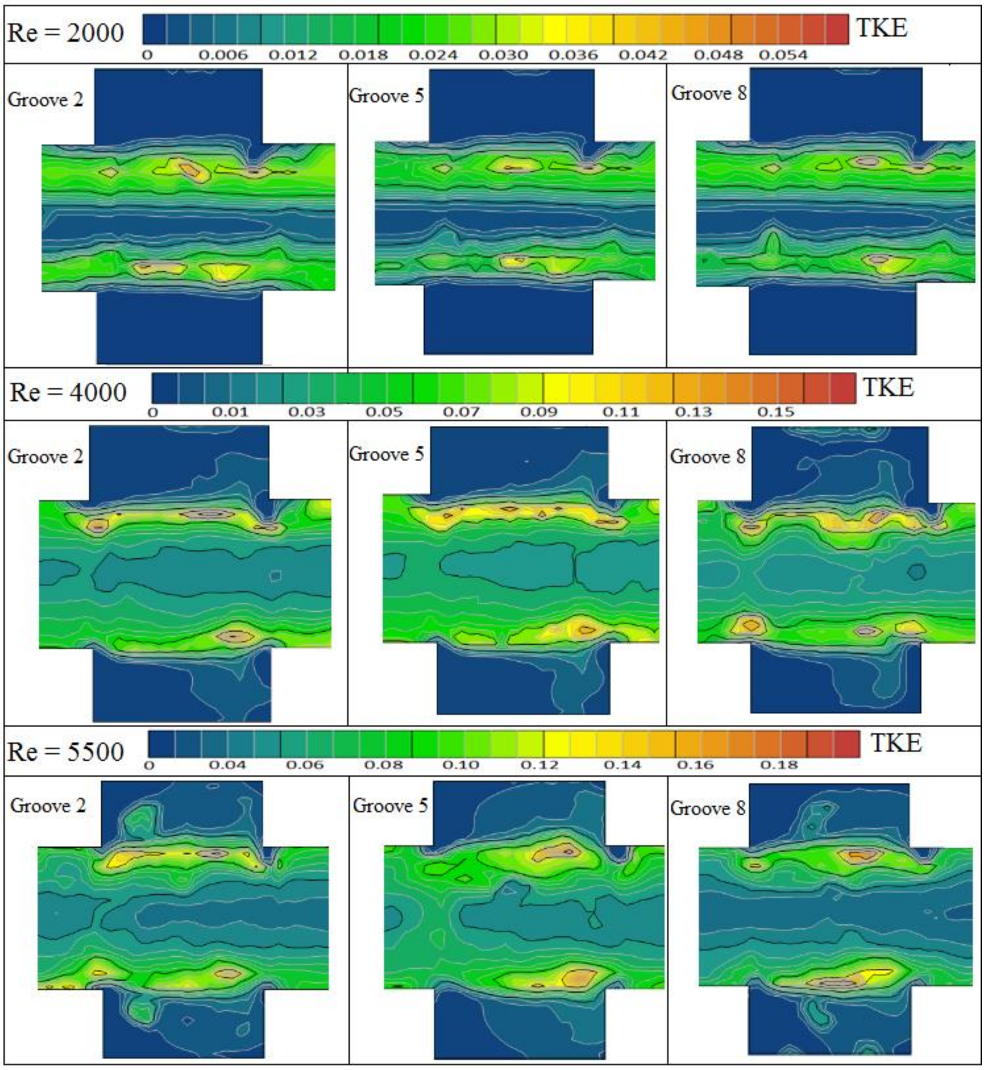

Figure 4.6. The turbulent kinetic energy distributions in different grooves for Reynolds numbers of $2x10^3$, $4x10^3$ and $5.5x10^3$.

According to the figure, it can be said that strong mixing emerges at the mouth of the groove where separated shear layers are located. However, intensity reduces near the central axis of the channel and the inside of the groove. Reduction in *TKE* is more dramatic for the area in the groove; this means the groove region is the weak point of the channel for heat and mass transfer applications. Moreover, *TKE* is strongly dependent on the Reynolds number. Significantly higher *TKE* values are observed at Re = 5.5x10^3 compared to Re = 2x10^3 and the increase of *TKE* is not limited to the mainstream, *TKE* values are also increased inside the groove which means that the turbulent mixing enhanced in this region.

The effect of shifting the grooved walls on the flow pattern is demonstrated in Figure 4.7 for Renolds numbers, Re of 2x10^3 and 5.5x10^3. Two different shifting distances which are half of the period, L/2, and a quarter of a period, L/4, are tested. Time-averaged streamlines indicate that shifting the grooved walls causes no discernible variation in the flow pattern. Similar recirculation eddies are seen in each case regardless of the position of the grooves. This indicates that each groove behaves individually, i.e., flow modified by the groove does not have any influence on the groove located at the opposite wall. An increase of Reynolds number, Re does not make a difference in the situation, and even at Re = 5.5x10^3, in which interaction between the mainstream and flow inside the groove is high, a similar flow pattern is kept for all shifting configurations.

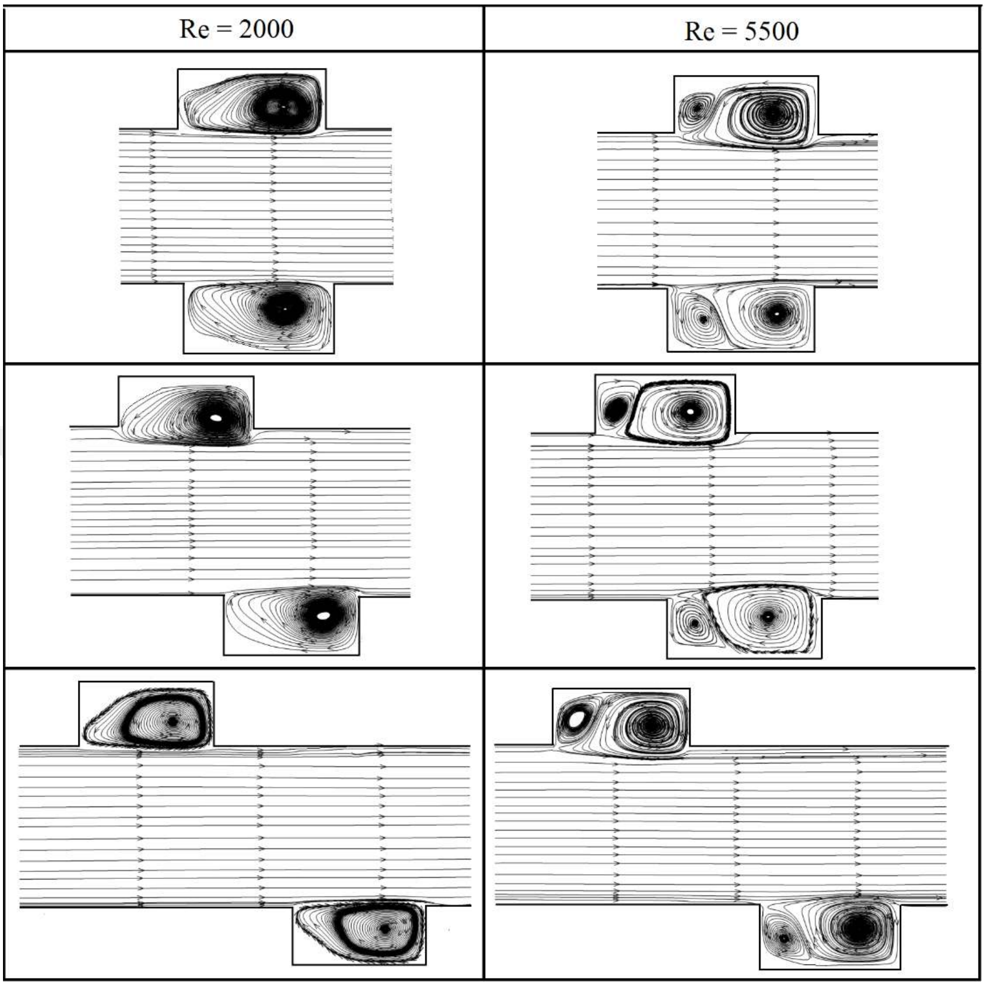

Figure 4.7. Patterns of streamlines in different grooved wall configurations.

Figure 4.8 is presented to summarize the effect of wall shifting on turbulence statistics. Time-averaged non-dimensional Reynolds stress, $\overline{u'v'}/u_o^2$ is presented in the figure at a Reynolds number, *Re* which groove is more effective in terms of disturbing the core flow. Nevertheless, the Reynolds stress, , $\overline{u'v'}/u_o^2$ contours show that shifting the walls do not cause a considerable difference. This is because instantaneous velocity fluctuations enhanced along separated shear layers does not spread beyond the central axis of the channel. As it is seen from the figure, Reynolds stress, , $\overline{u'v'}/u_0^2$ values are very low around the central axis, and this low Reynolds shear stress region separates the region with high fluctuations in instantaneous velocity components. Eventually, Figure 4.8 shows that segregation between upper and lower grooves is not just at large scale flow motions shown in Figure 4.7 but also at small scale turbulent structures. Therefore shifting the wall brings no worthwhile effect in this particular grooved channel geometry.

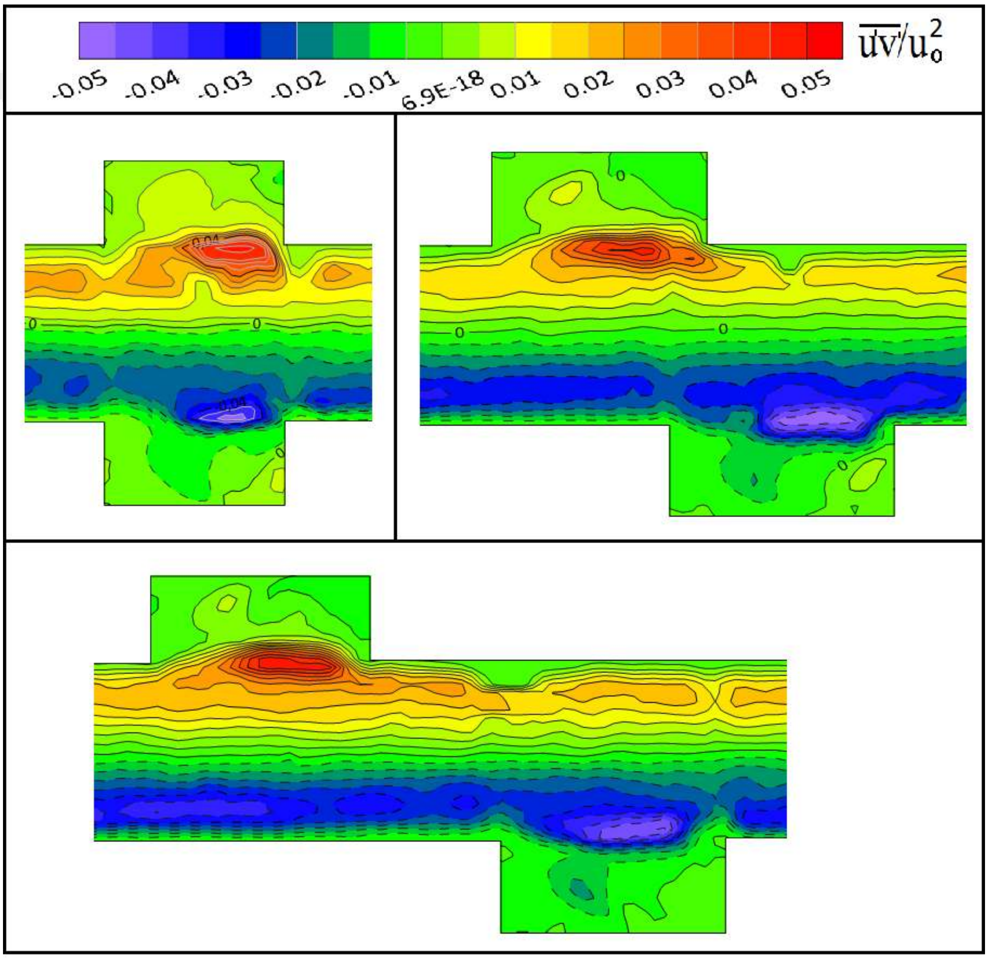

Figure 4.8. Reynolds stress in different grooved wall configurations for Re = $5.5x10^3$.

4.2. Heat Transfer and Pressure Drop in Steady Flow

Comparison of Nusselt numbers, *Nu* for smooth and grooved channels in Figure 4.9 shows that the flow modified by grooves significantly affcets convective heat transfer from the channel. The highest heat transfer enhancement is detected at $Re = 3x10^3$ which is 2.67 times greater than the straight channel. Enhancement decreases for higher Reynolds numbers, *Re* and it becomes 1.9 times higher than straight channel at $Re = 6.5x10^3$. The main reason for the increase in heat transfer is the enhancement of the mixing between hot fluid at the thermal boundary layer and cold fluid at the central region of the channel via turbulence created by disturbance with grooves. As a result; the thermal boundary layer cannot be continuously developed as it occurs in a smooth channel and becomes thinner than the smooth channel. Another important factor that affects heat transfer is the Reynolds number, *Re*. Turbulence, promoted with the increase of the Reynolds number, *Re* positively affects the heat transfer from the channel. As mentioned above shift of grooved walls has an insignificant impact on flow properties. Therefore heat transfer results do not diverge much for any shifted wall configurations. (see Figure 4.10) Similar to the results of the velocity profile, a good agreement is also obtained between the experimental and numerical Nusselt number, *Nu* values.

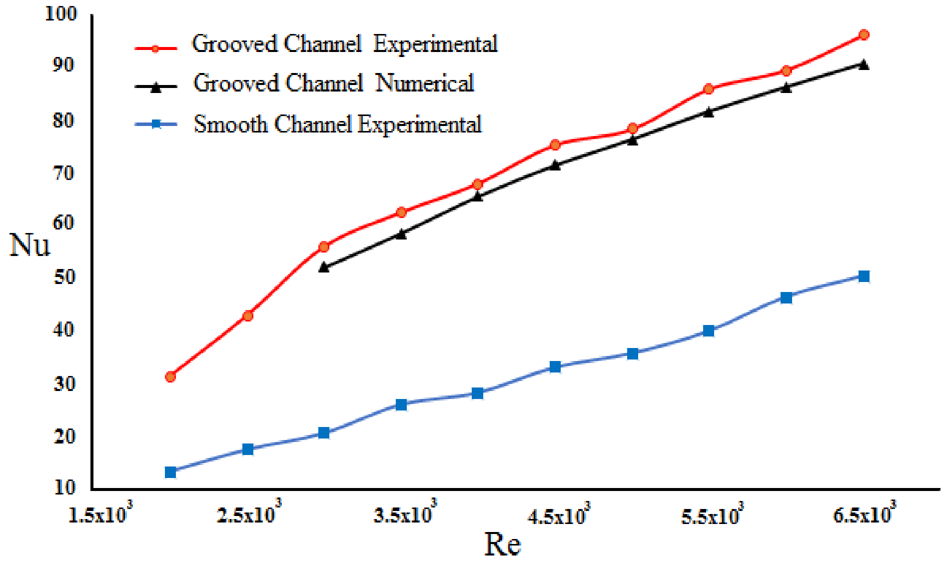

Figure 4.9. Variation of Nusselt number with respect to Reynolds number for the grooved channel with no wall shifting.

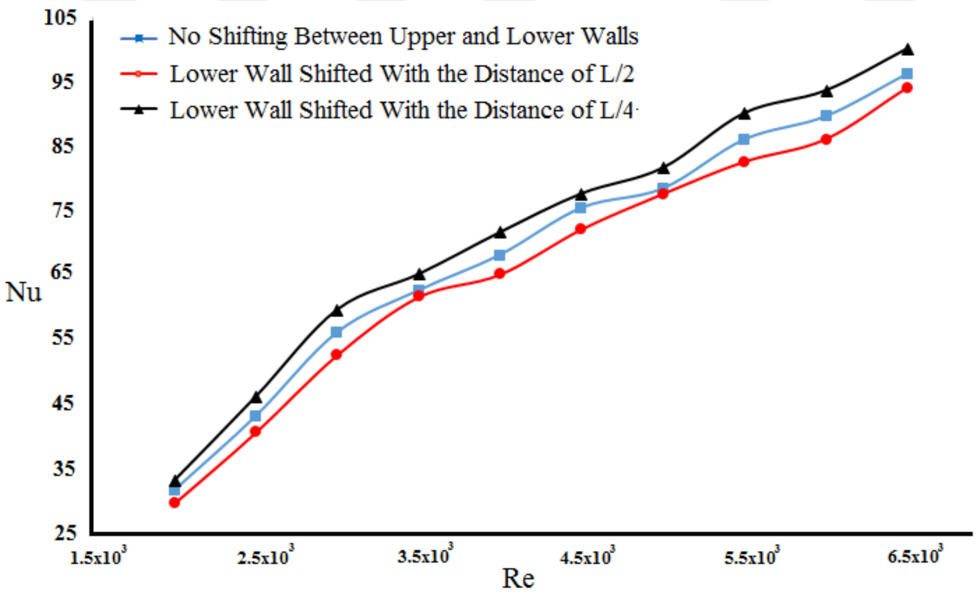

Figure 4.10. Variation of Nusselt number with respect to Reynolds number for different wall shifting configurations.

The relationship between temperature field and Reynolds number, *Re* (Figure 4.11) gives the rationale for the increase of heat transfer for higher Reynolds numbers, *Re*. As it is seen from the figure, the thickness of the thermal boundary layer reduces, and the cold flow region takes up more space in the channel with increasing Reynolds numbers, *Re*. In addition, the temperature of flow circulating inside the groove reduces at a high Reynolds number, *Re* as a result of improved mass transfer between groove and main flow. This is clearly observable from the comparison of Figures 4.11a and 4.11c. The coldest flow temperature level seen near the central axis of the channel in Figure 4.11a reaches the deep of the groove in Figure 4.11c. As indicated by the temperature field, groove regions are locations where the poorest heat transfer occurs, and the Reynolds number, *Re,* plays an important role in improving heat transfer in these regions.

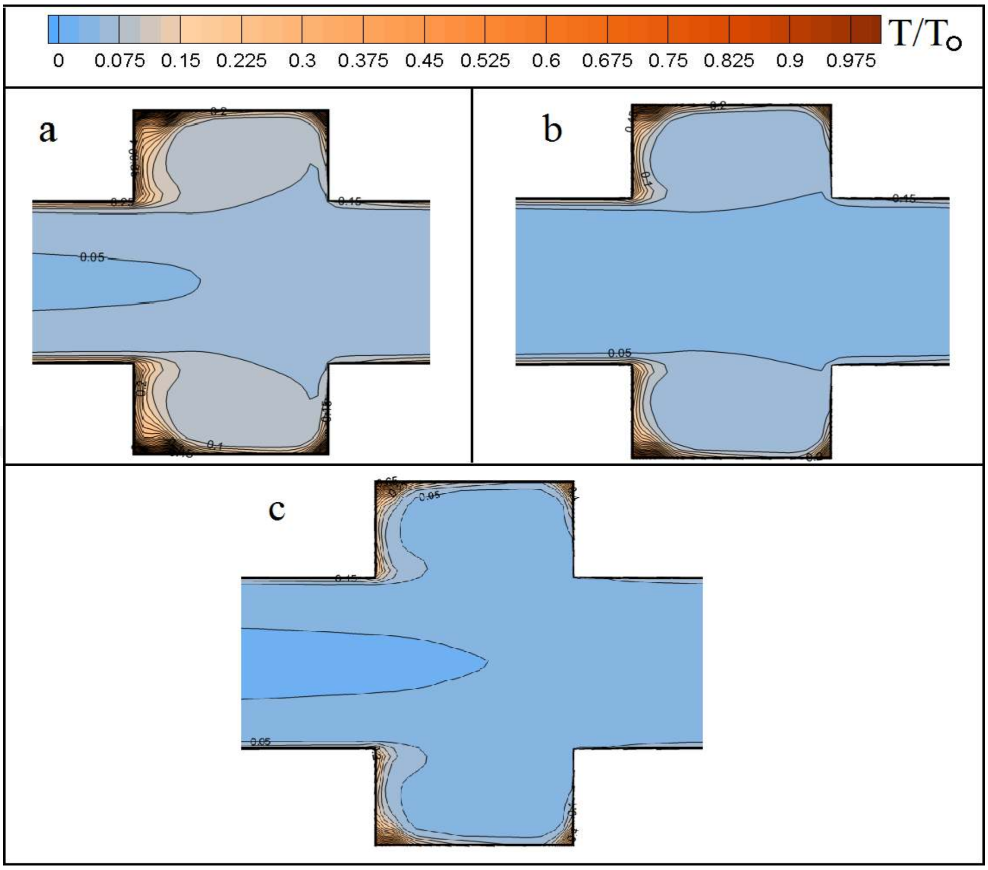

Figure 4.11. Temperature contours for a) Re = $2x10^3$, b) Re = $4x10^3$and c) Re = $5.5x10^3$.

An increase in heat transfer by using rectangular grooves is not a cost-free process. Disturbing the flow passing through the channel causes the rise of pressure drop between the inlet and outlet of the channel which also means the rise of required pumping power. As an indicator of pressure drop, a non-dimensional parameter; friction factor, *f* is plotted in Figure 4.12 with respect to the Reynolds number, *Re*. The friction factor, *f* values show grooved channel causes a significantly higher pressure drop than the smooth channel. Use of grooved channel cause 2.8-3.2 times increase in the friction factor depending on the Reynolds number, *Re*. The slope of the friction factor curves points out a reduction in friction factor with increasing Reynolds number, *Re,* however, this reduction does not mean pressure drop reduced, since by definition *f* is inversely proportional with square of mean velocity, u_o, increase of mean velocity cause a slight reduction in friction factor, *f*. Similar to heat transfer results pressure loss also does not change significantly for shifted grooved walls (Figure 4.13).

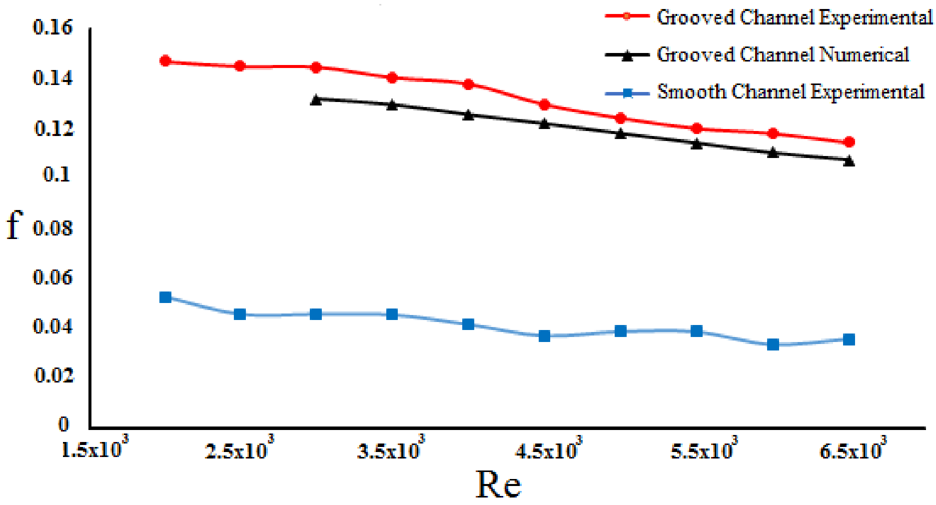

Figure 4.12. Variation of friction factor with respect to Reynolds number for the grooved channel with no wall shifting.

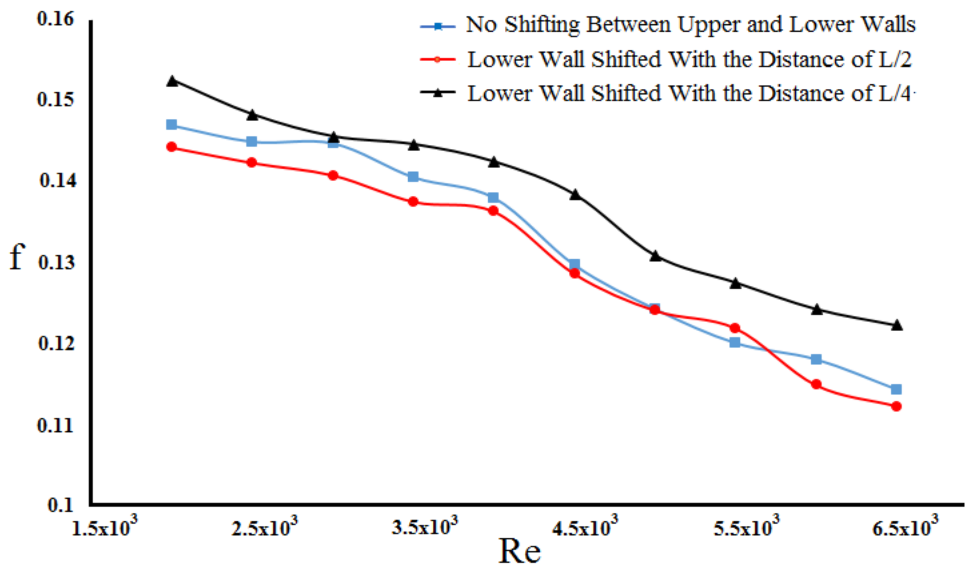

Figure 4.13. Variation of friction factor with respect to Reynolds number for different wall shifting configurations.

The thermal performance factor, *TPF,* is an important parameter in terms of evaluating both heat transfer enhancement and pressure drop. The *TPF* values in Figure 4.14 are greater than unity for all Reynolds numbers, *Re* and groove position configurations, showing that despite the increase of pressure loss with the use of the grooved channel instead of the smooth one, total energy gain is positive. The *TPF* rises as the Reynolds number, *Re* increases from $2x10^3$ to $3x10^3$. The rise of *TPF* points out that the heat transfer augmentation ratio increases relatively higher than the pressure loss ratio. Peak point, which is 1.75, detected for *Re* = $3x10^3$ and no shifted wall configuration. After *Re* = $3x10^3$ *TPF* starts to decline, i.e., the increase of pressure drop ratio becomes greater than the increase of heat transfer enhancement ratio. Its lowest value, 1.25, is seen at *Re* = $6.5x10^3$ with the wall shifted as L/2.

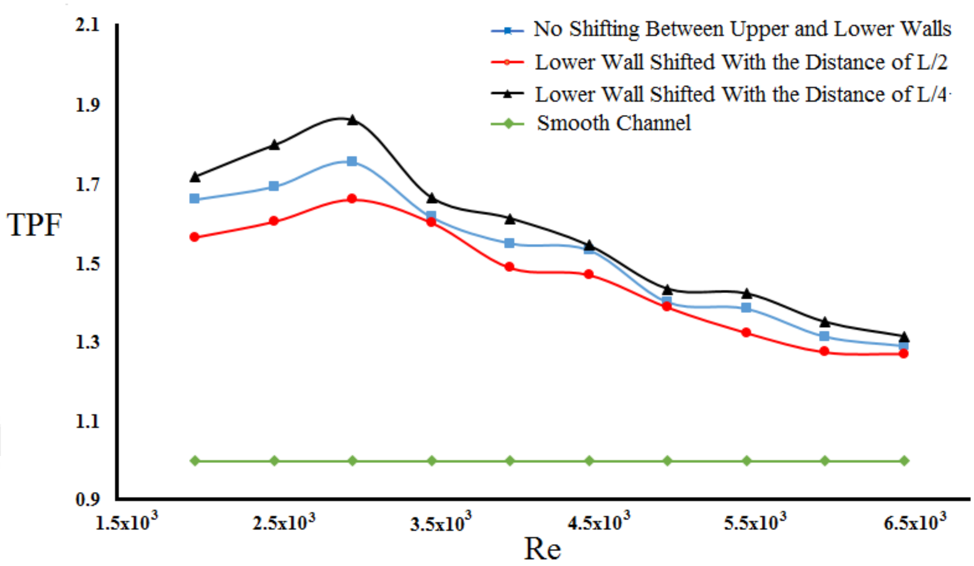

Figure 4.14. Variation of thermal performance factor with respect to Reynolds number for different wall shifting configurations.

Depth of the groove changes the heat transfer capability of the grooved channel expressively. The numerical part of the current study is extended to investigate the effect of groove depth. Results are presented in Figure 4.15 for six depths which is defined non-dimensionally as groove depth, groove length ratio,n = l/ L_g. As the figure indicates, n = 0.2 provides the highest heat transfer for all Reynolds numbers, *Re*. When the n = 0.2 curve is examined, it can be seen that it diverged from other curves when the Reynolds number increased. This is because for n is greater than 0.2 slope of the other curves reduces slightly with increasing Reynolds numbers, *Re*. However, the same reduction does not occur for n = 0.2. In addition, heat transfer caused by groove with n = 0.1 becomes better with increasing Reynolds number, *Re*. It causes the lowest heat transfer in low Reynolds numbers, *Re,* but its performance gets better as the Reynolds number, *Re* increases and it provides better heat transfer than n = 0.6 and n = 0.5 in high Reynolds numbers, *Re*.

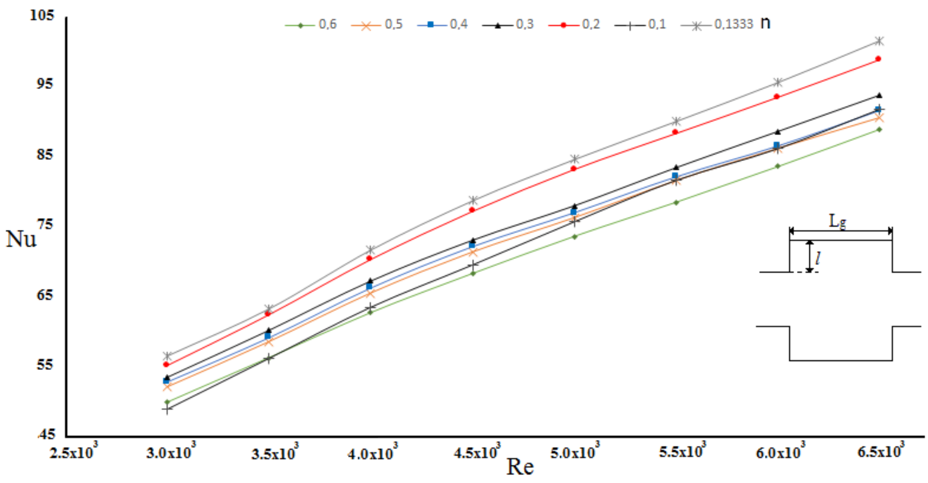

Figure 4.15. Effect of groove aspect ratio on the Nusselt number.

The effect of groove depth on the friction factor is presented in Figure 4.16 for various Reynolds numbers, *Re*. The groove depth, which is represented by n = 0.2 provides the highest heat transfer, also gives the highest friction factor. However, the n = 0.2 curve does not differ from others, as it is presented in Figure 4.15. Moreover, the geometry that has the deepest grooves (n = 0.6) causes a considerably lower friction factor compared to other geometries.

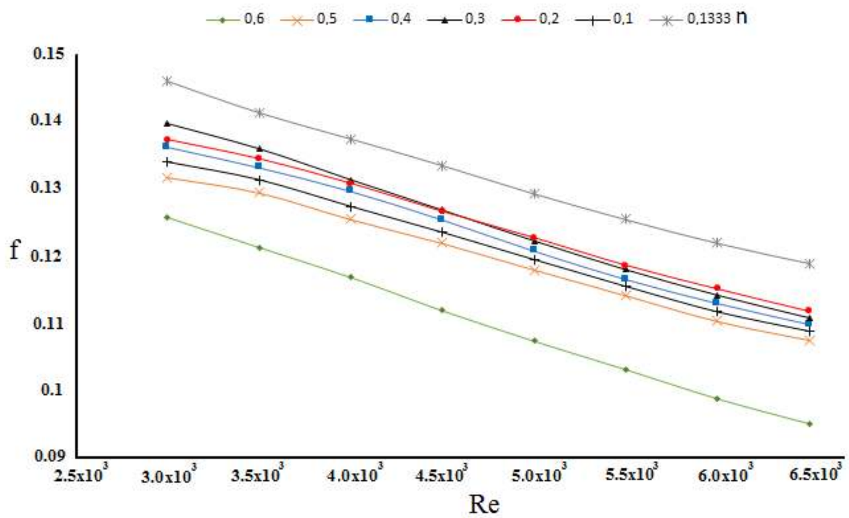

Figure 4.16. Effect of groove aspect ratio on the friction factor.

Despite its high friction factor groove with 0.2 depth to the length ratio has the highest *TPF* for all Reyolds numbers, *Re*. Moreover, groove depth represented by n = 0.1 causes a moderate friction factor, but since it provides the lowest heat transfer among investigated geometries, its *TPF* becomes the lowest. Comparison of *TPF* values for n = 0.5 and n = 0.6 indicates n = 0.5 shows better overall performance up to *Re* = 5.5x10^3 however *TPF* of n = 0.6 exceed n = 0.5 with increasing Reynolds number, *Re,* and it almost reaches the *TPF* of n = 0.3 for *Re* = 6.5x10^3. It is obvious that curves of n = 0.6 and n = 0.3 coincide at *Re* = 6.5x10^3 for two different reasons. The dominant parameter for the determination of *TPF* for n = 0.3 is the Nusselt number, *Nu*, however, the low friction factor of n = 0.6 raises the *TPF* for this Reynolds number, *Re*. Therefore groove depth represented by n = 0.6 shows itself as an alternative in high Reynolds numbers, *Re,* if pressure drop has a priority.

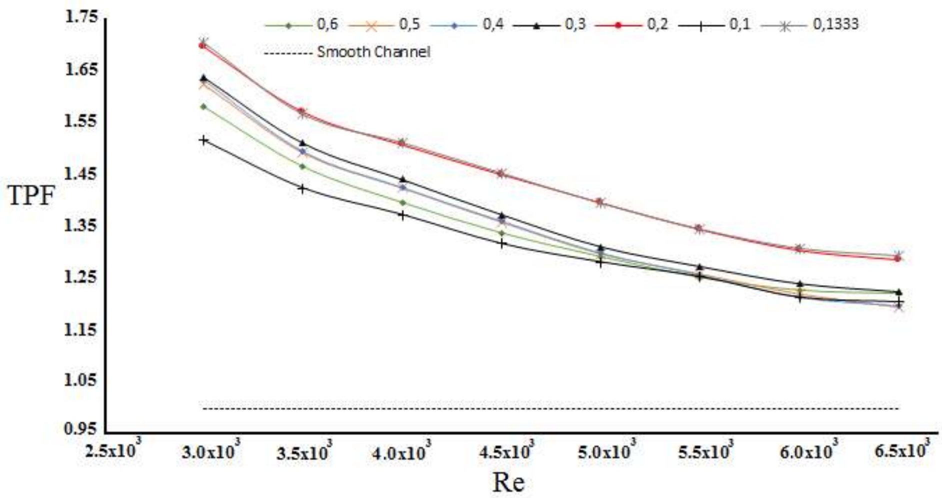

Figure 4.17. Effect of groove aspect ratio on thermal performance factor.

Pressure distribution along the central axis of the channel and walls of the second groove period is presented in Figure 4.18 for *Re* = 5.5x10^3. These data are obtained from numerical simulations. Wall and central axis static pressure values are non-dimensionalized by dividing them to the inlet static pressure. Time-averaged velocity vectors are also given to demonstrate the relationship between flow structures and static pressure distributions. It is an expected phenomenon pressure will drop along the channel in a streamwise direction. As it is seen in the figure, the wall, and central pressure decrease in accordance with each other away from the groove. However, the dynamics of secondary flow regions cause sudden variations of pressure distribution on the groove walls. The peak value of the pressure is detected at the near upper corner of the downstream groove wall. This is expected because mainstream enters the groove near the downstream corner, it hits the groove wall and its dynamic pressure is converted to static pressure. Similarly circulating flow hits the bottom wall of the groove near the lower corner therefore secondary pressure peak occurs at this location. Pressure reduces near the middle of the bottom wall because as the vector field indicates circulation changes its direction where two circulation regions intersect and flow separate from the surface. Another rapid reduction is observed right after the upper downstream corner of the groove. Here flow can not stay attached to the surface because the sharp corner, pressure values return to normal level in a short distance from the corner. Finally, the decrease rate of the central axis pressure increases between the grooves because circulating regions protrude beyond the groove and compress the mainstream resulting flow structure behaves as a contradiction.

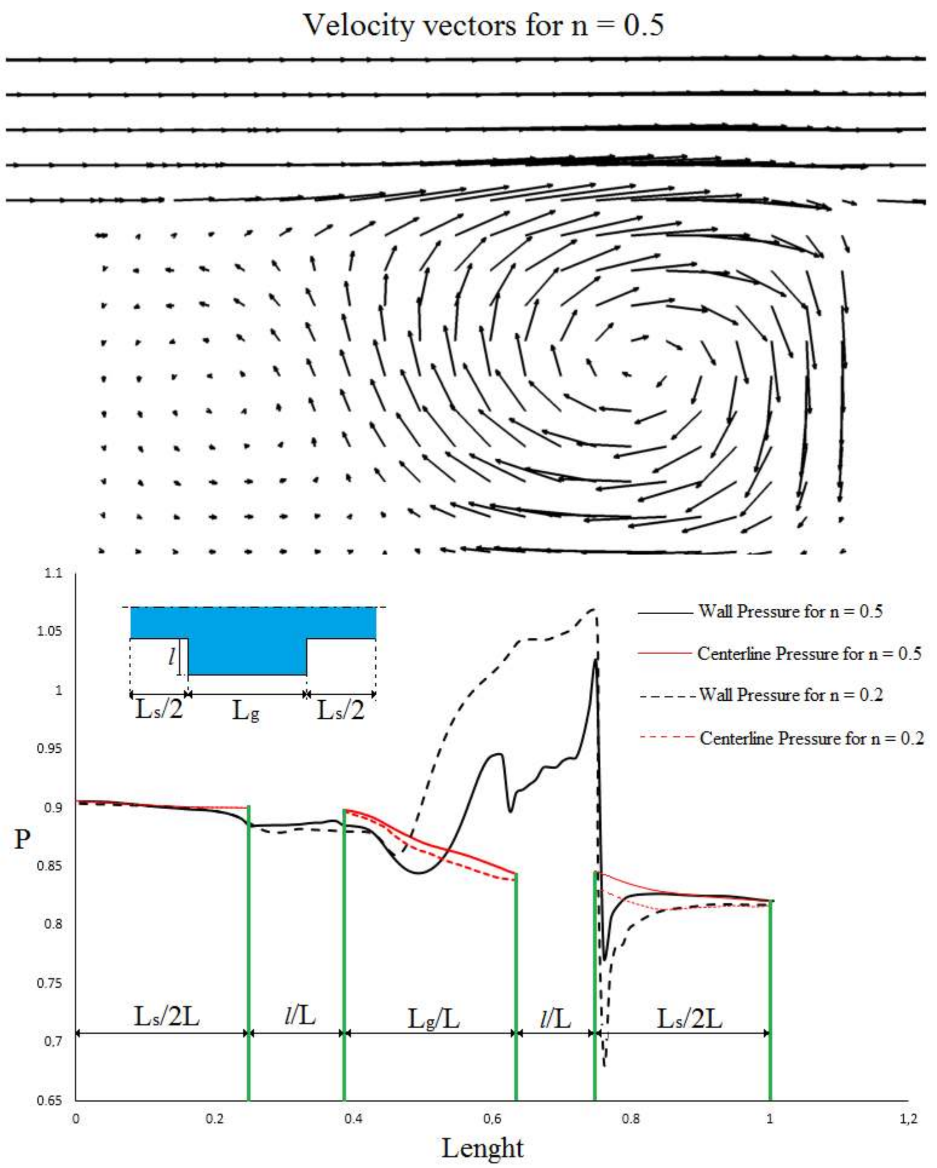

Figure 4.18. Averaged vector plot and pressure distribution for groove 2 at Re = $5.5x10^3$.

4.3. Pulsating Flow Observations Employing the PIV Method

For the steady-state of the flow in the corrugated channel, the PIV method was used to reveal the physics of the flow in order to understand the effect of the corrugations on the increase in the heat transfer rate. Since this method can measure instantaneous velocities at many points of the flow field, comprehensive information about the physics of the flow was obtained. As it is known, in the case of a pulse given to the flow, the boundary layer development is constantly disturbed by the pulsatile flow, thus increasing the mass mixture in the flow domain and spreading the momentum and heat transfer to the entire flow area. For this reason, it has been tried to reveal how the flow structure is effective on heat transfer by measuring instantaneous velocities in a particular area of the pulsed flow with the PIV method. Data obtained in this part of the experiment have been reported below.

Time-averaged streamlines in Figure 4.19 show the flow structure in various grooves and flow conditions. In the first row of the figure, the Reynolds number, *Re* and pulsation frequency, *F* are kept constant, and flow structure is investigated for three different groove positions located upstream, middle and downstream parts of the channel. Similar flow structures are observed in each groove which is consists of two opposite rotating circulation regions. The second row of the figure is devoted to investigating the influence of pulsation frequency. Groove 8 is selected for the investigation. When there is no pulsation one well-defined large flow circulation dominates the area inside the groove; however, when flow pulsation is applied with 1 Hz frequency, the secondary flow circulation region appears near the upstream side of the groove. The increase of the frequency to the 2 Hz flow structure inside the groove resembles the steady flow case. In the last row, the effect of frequency is investigated for Re = $5.5\text{x}10^3$. The secondary recirculation region that is not evident in steady flow with the Reynolds number of $2\text{x}10^3$ becomes apparent for Reyolds number of $5.5\text{x}10^3$. However, in high Reynolds numbers, *Re,* flow pulsation does not cause a clear difference in time-averaged flow patterns for any value of frequencies.

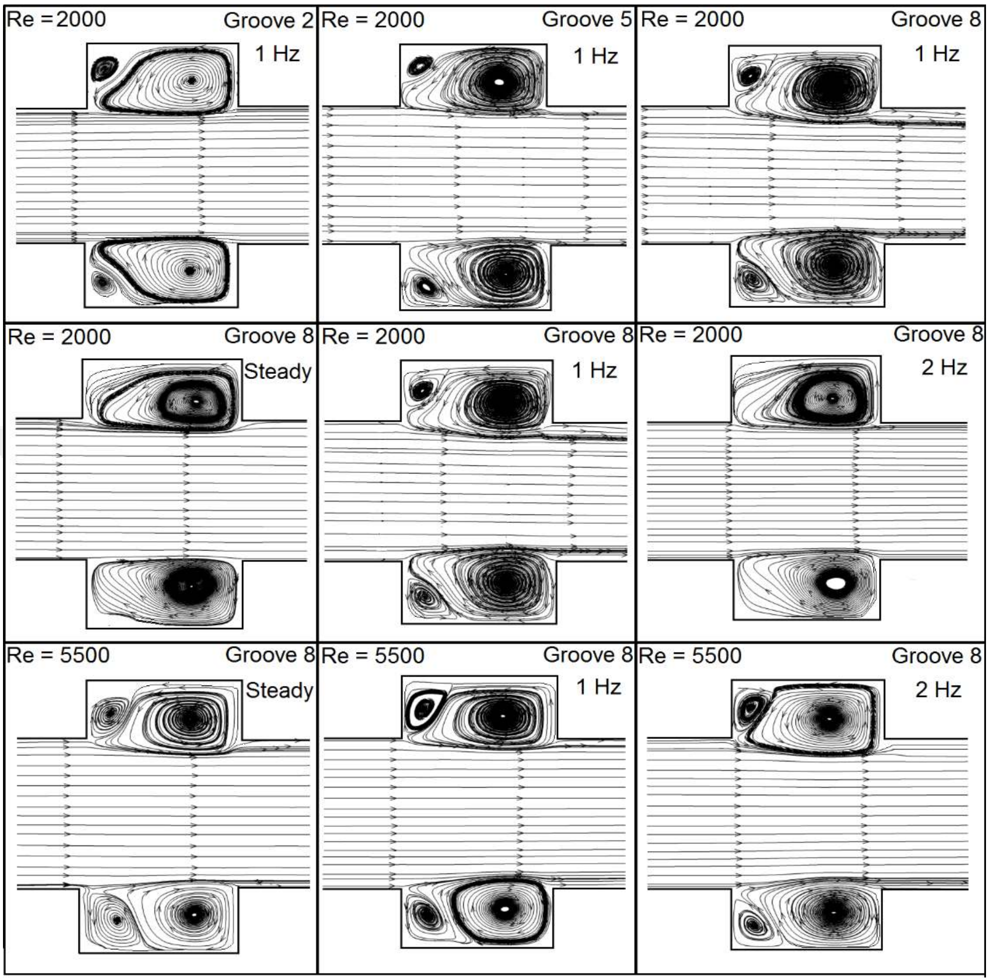

Figure 4.19. Patterns of time-averaged streamlines for various pulsating flow conditions and groove positions.

During the pulsating flow process, the flow pattern inside the groove changes significantly. Phase averaged streamlines are demonstrated in Figure 4.20 for three different steps of pulsation. In the low-velocity phase ($\Omega t = 3\pi/2$) the primary circulation region enlarges for both low and high Reynolds numbers, *Re*. The prominence of the secondary flow circulation region depends on the Reynolds number, *Re,* as it happens in steady flow cases (see Figure 4.1). In the acceleration part of the period ($\Omega t = 2\pi$), the incoming flow pushes the main flow circulation to become smaller. Flow structures out of the main circulation region show a significant dependence on Reynolds number, *Re*; in the case of the high Reynolds number, *Re,* secondary recirculation region enlarges and additional recirculation region forms up. However, for the low Reynolds number, the incoming flow enters the groove near the upstream corner it travels inside the upstream half of the groove and then goes out. During this process, the main recirculating flow region gets smaller but is not destroyed. Throughout the peak velocity phase ($\Omega t = 5\pi/2$) main recirculation region enlarges in size in the horizontal direction and presses the secondary flow circulation region at $Re = 5.5x10^3$. The secondary recirculating flow region is pressed by the main recirculating flow region for $Re = 2x10^3$ as well. However, the secondary circulation region is larger for $Re = 5.5x10^3$ than for $Re = 2x10^3$. As it is explained above, fluid flow in the groove is remarkably dynamic in pulsating flow conditions. This dynamism of fluid flow indicates that the with the effect of pulsation main flow is able to penetrate wake flow area inside the of the groove.

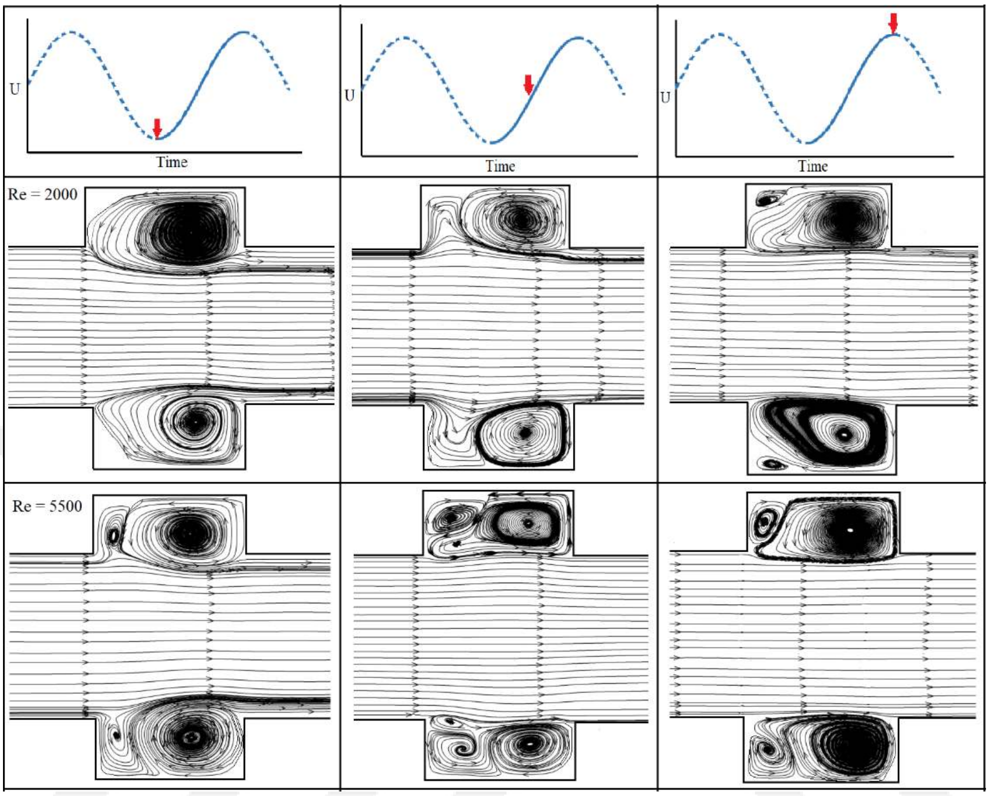

Figure 4.20. Phase averaged streamlines for high and low Reynolds numbers and 1 Hz pulsation frequency.

Pulsating frequency of 2 Hz caused a different flow structure inside the groove than the 1 Hz frequency as shown in Figure 4.21. Since the successive variation of velocity occurs more frequently in high pulsation frequency, *F*, the circulation regions cannot enlarge in size in the low-velocity phase as much as it happens in 1 Hz. This situation is valid for *Re* = 2x10^3 and *Re* = 5.5x10^3. The increase in pulsation frequency, *F,* caused a significant change in the flow pattern for the *Re* = 2x10^3 in the acceleration phase (Ωt = 2π). In the acceleration phase of the 1 Hz frequency, the flow entering the groove on the upstream side is not observed at the 2 Hz frequency. A similar flow pattern is seen between low velocity (Ωt = 3π/2) and acceleration (Ωt = 2π) phases of *Re* = 5.5x10^3. Primary and secondary circulation regions reach almost identical sizes at the peak velocity phase (Ωt = 5π/2) of *Re* = 2x10^3. However, for the *Re* = 5.5x10^3, the flow pattern keeps its shape but a slight increase in the secondary circulation region occurs.

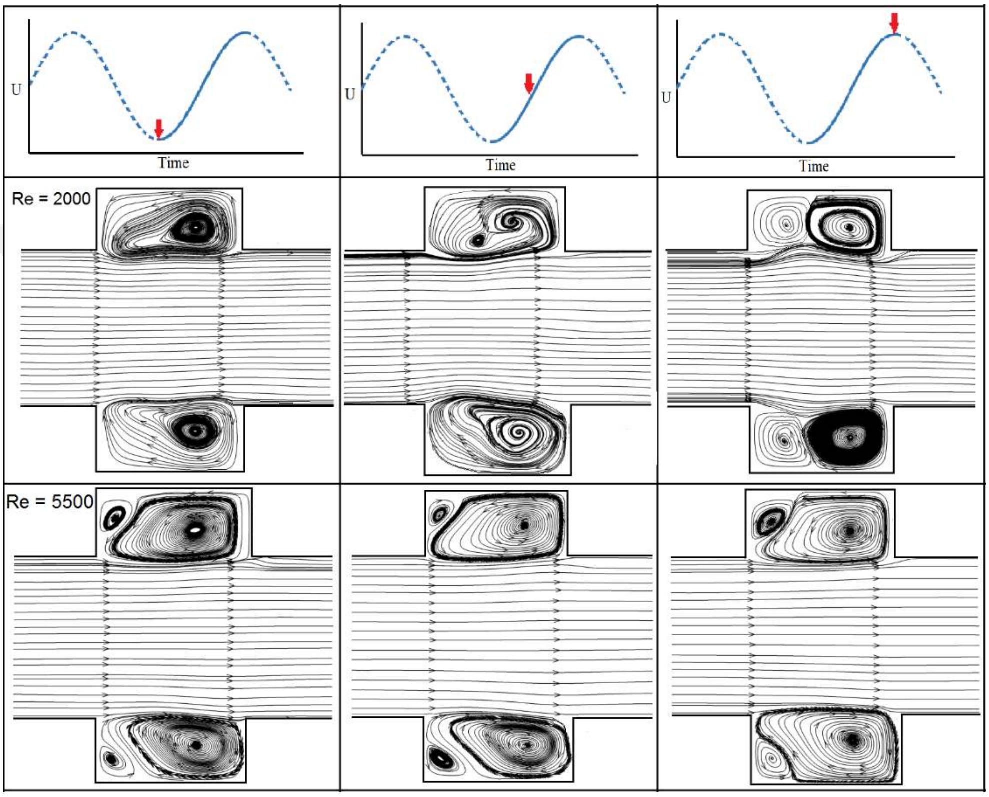

Figure 4.21. Phase averaged streamlines for high and low Reynolds numbers and 2 Hz pulsation frequency.

Instantaneous velocity vector field together with velocity magnitude, u_{mag}, contours are presented in Figure 4.22 for six different instants of a pulse period at *Re* = 2x10^3 and *F*= 1 Hz. The moment in which mainstream velocity reaches peak is tagged as ‘t = 0’, and a period of pulsation is investigated as the time evolved. The time between two images taken by PIV was determined as Δt. At the high-velocity phase of the period (t = 0), some fluid is caught by the groove. The flow joined the recirculation inside the groove has high momentum, and it accelerates the main circulation region inside the groove. However, the secondary circulation region near the bottom of the upstream wall of the groove is not significantly affected by the velocity increase of main recirculation (Figure 4.22(b)). During the deceleration phases (Figure 4.22(c) and (d)) recirculation region enlarges and protrudes beyond the groove. Thus, the mass transfer occurs from the circulation region to the mainstream. When the acceleration phase starts (Figure 4.22(e)), another fluid transfer process happens between mainstream and groove. This time, fluid enters the groove near the upstream corner of the groove. It pushes the main circulation region further downstream and eliminates the secondary circulation region. However, the second fluid transfer process is relatively weaker than the first one and it is observed that the momentum of the flow in this process changes at each cycle of the pulsation. Therefore penetration of second mass transfer to the deep of the groove can not happen efficiently at each pulsation period. Nevertheless, for no pulsation, the wake region in the vicinity of the upstream wall of the groove has the lowest magnitude of the velocity, and the rate of heat transfer is poor where the groove surfaces interact with this wake region; therefore, the second mass transfer process is beneficial for enhancing the heat transfer from these part of bottom wall surfaces. In the final phase of pulsating flow cycle, (Figure 4.22(f)) velocity values in the groove start to reduce, and the flow pattern begins to resemble that is seen in the first stage. The sequence shown in Figure 4.22 indicates a substantial mass transfer improvement compared to the flow pattern given in Figures 4.3 (e) and (f). A similar mass transfer was reported for triangular grooved channels by Xin et al. (2007) for pulsating flow. In their study circulation region inside the groove is ejected from the groove at certain instants. This phenomenon is not observed in the current study, the circulation region is deformed, but it keeps its existence during the pulsation. This indicates that the groove geometry has an effect on the interaction process between mainstream and wake flow in the groove.

In Figure 4.23 a pulsation period investigated for Re = 5.5x10^3 and F = 1 Hz. In the higher Reynolds number case, there is no striking difference compared to Figure 4.22 the main circulation region is deformed during the period of pulsation. It gets smaller at the acceleration part of the pulsation cycle. Conversely, it becomes larger at the deceleration phases of the pulsation cycle. Mass transfer between groove and mainstream also occurs in similar phases as Re = 2 x10^3. However, the second mass transfer process is given in Figures 4.22(e), and (f) is not observed for Re = 5.5 x10^3. As the results presented in Figure 4.23 indicate pulsating flow promotes mass transfer between groove and mainstream for higher Reynolds numbers, Re as well. For steady flow, there is already considerably better mass transfer available for Re = 5.5 x10^3 compared to the case of Re = 2x10^3, which is documented in Figure 4.3. Therefore, the relative improvement of interactions between the mainstream and wake flow of groove in the case of pulsating flow instead of steady flow is more evident in low Reynolds numbers, Re.

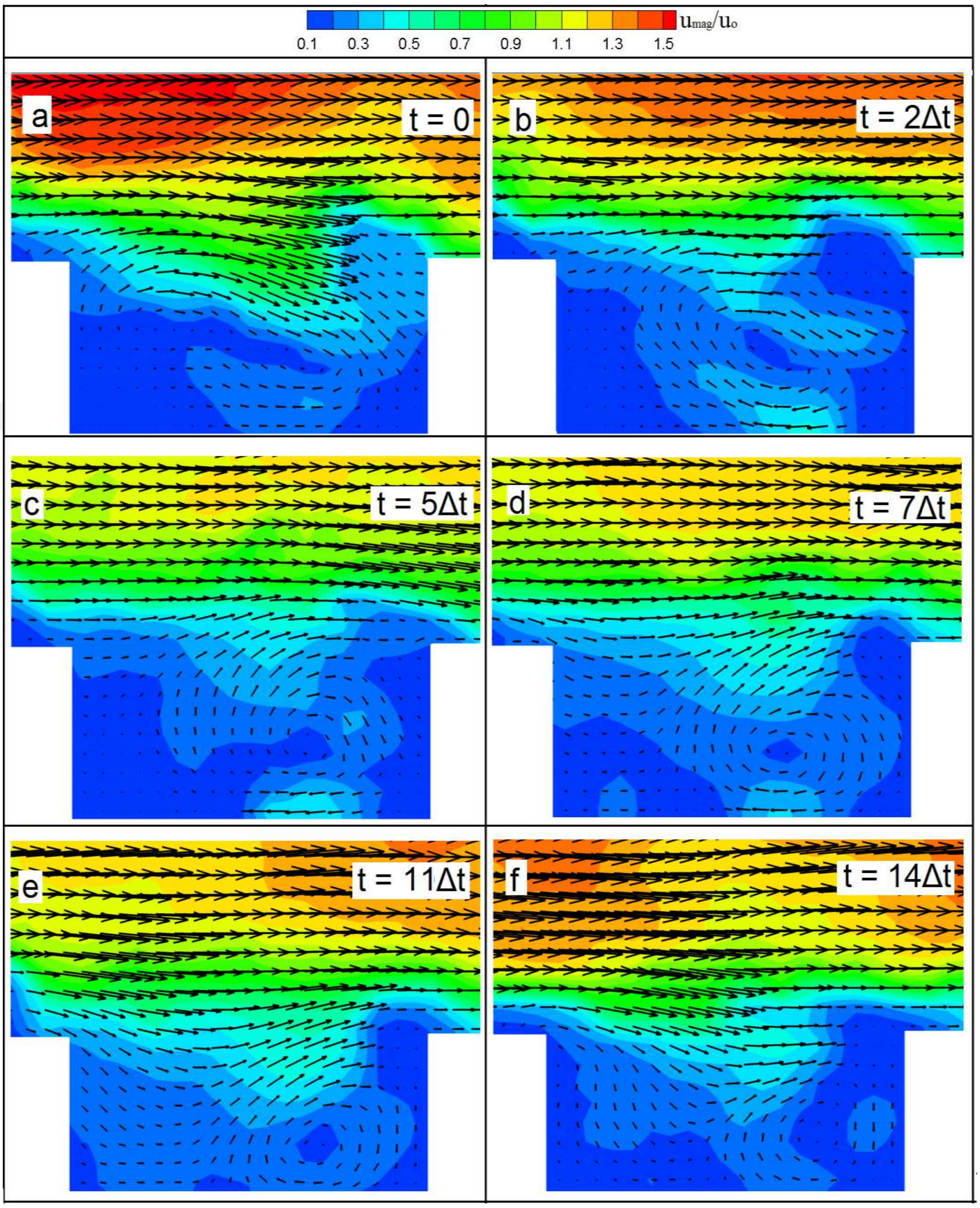

Figure 4.22. Instantaneous velocity vectors and dimensionless velocity magnitude contours for $Re = 2x10^3$ and F = 1 Hz.

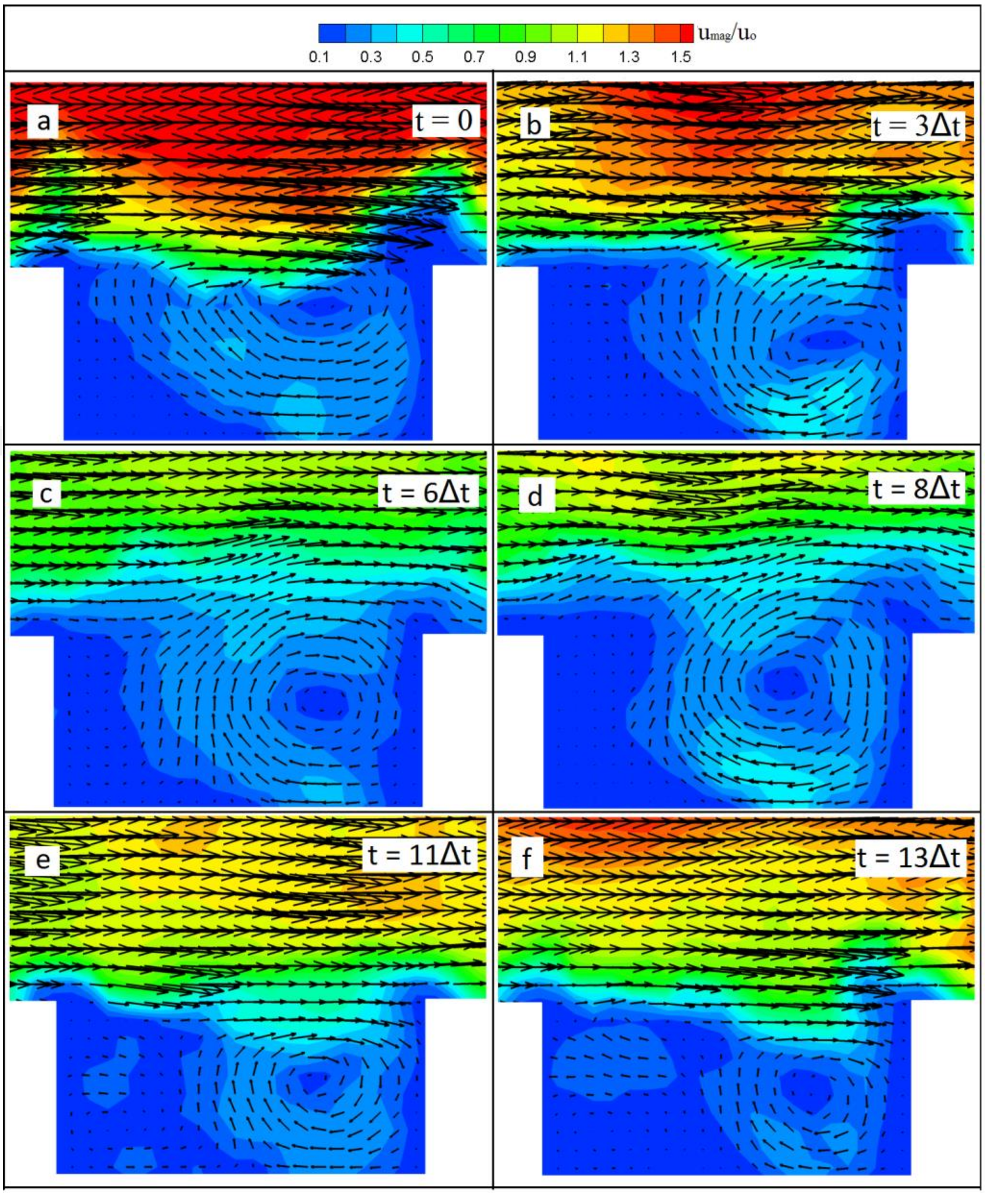

Figure 4.23. Instantaneous velocity vectors and dimensionless velocity magnitude contours for Re = 5.5x10^{3}and F = 1 Hz.

A case for *Re* = $2x10^3$ and *F* = 2 Hz is shown in Figure 4.24 to demonstrate the effect of higher frequency on flow behaviour. In high frequency, every phase lasts a shorter time resulting in a difference in flow patterns. This situation is seen when the acceleration stages in Figure 4.22 and Figure 4.24 are compared. Figure 4.24(c) and (d) reveales that flow circulation region enlarges in the horizontal direction, and fluid transfer from the groove wake flow to the mainstream region occurs near the upstream corner of the groove. As the flow accelerates, the location where massive fluid transfer from the groove to the core flow region shifts downstream. However, as discussed before an additional flow transfer occurs from the mainstream to the groove space for 1 Hz flow pulsation. It can be concluded that rapid acceleration of flow does not let this second fluid transfer process since the change between phase angles of pulsating cycle happens in a short time as seen in Figure 4.23(e), and flow patterns rapidly resemble their initial appearance which occurs at the beginning of the period.

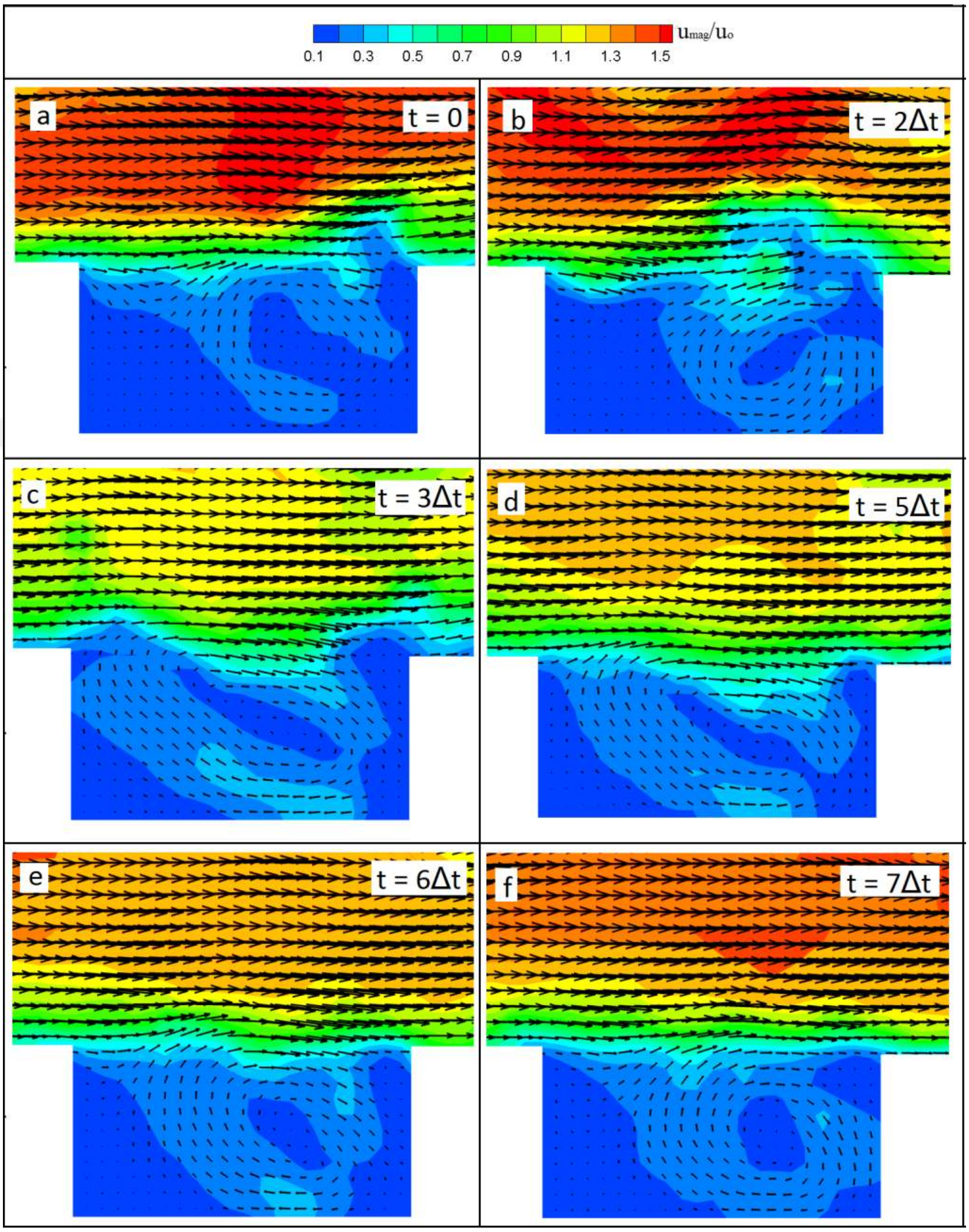

Figure 4.24. Instantaneous velocity vectors and dimensionless velocity magnitude, contours for *Re* = 2x10^{3}and *F* = 2 Hz.

Like the velocity field, the vorticity field also varies during the period of pulsation. This variation is shown in Figure 4.25 for the Reynolds number of $5.5 x 10^3$ and frequency of 1 Hz. In the figure, the period starts when velocity is nearly time-averaged velocity. As the figure indicates, vorticity, ω is concentrated near upstream corners of the grooves where vortex shedding occurs, at t = 0. During the acceleration phase, high vorticity, ω spread through the shear layer (Figure 4.25(b)) and intensified when flow velocity reaches a peak (Figure 4.25 (c)). At the beginning of the deceleration phase (Figure 4.25(d)) high vorticity region along the shear layer starts losing its intensity; however, vorticity diffuses towards the central axis of the channel. Finally, the intensity of vorticity, ω continues to decrease, and high values of vorticity, ω are seen only in a limited region in the shear layer at the next stages of the deceleration(Figure 4.25(e) and (f)).

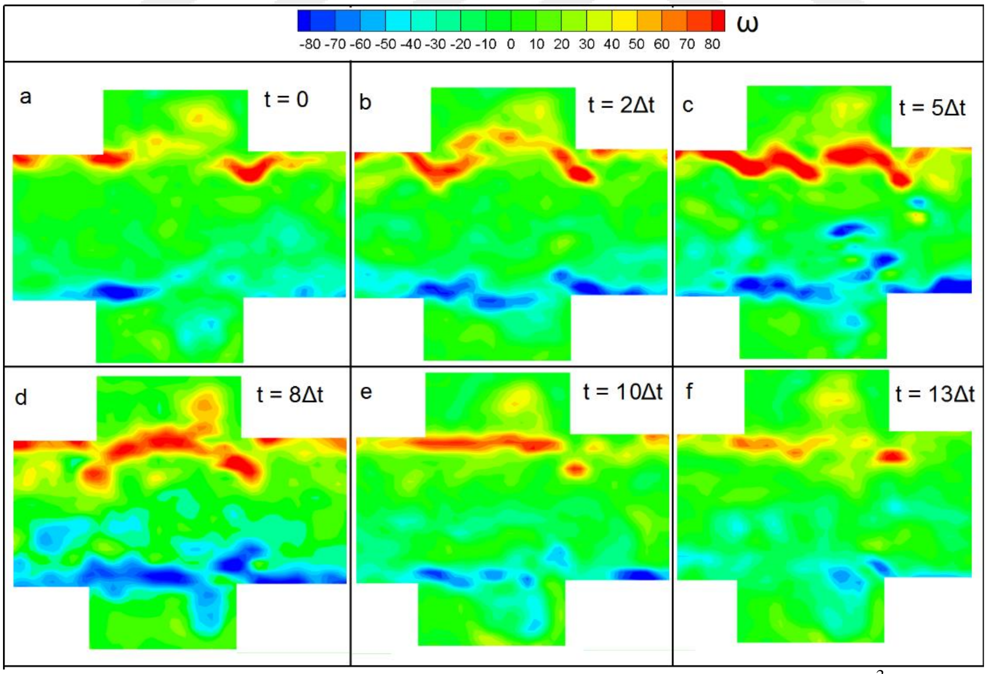

Figure 4.25. Instantaneous vorticity contours in groove 8 for Re = $5.5 x 10^3$ and F = 1 Hz.

Time-averaged vorticity, ω is plotted in Figure 4.26 for steady flow and two different pulsation frequencies, *F*. During the pulsation period, the instantaneous vorticity field indicates that vorticity, ω diffuses in the channel, and local peaks occur in specific locations. The magnitude of vorticity concentrations is gradually attenuated to a very low value during decelerated phases of the pulsation cycle. Hence, peak values of vorticity, ω and discrete vortical structures at the outer boundary of the shear layers are canceled out in the averaging of instantaneous vorticity data. Therefore, as it is seen in Figure 4.26 vorticity values are concentrated primarily along with the separated shear layer near wake flow. The pulsating flow causes a notable difference in the vorticity field, especially for $Re = 2x10^3$. When comparing Figures 4.26(a) and (b), the vorticity value increases in separated shear layers with the use of pulsating flow. But more importantly, an increase in vorticity, ω is detected inside the groove near the downstream corner (see Figure 4.26(b)) which means mainstream groove interaction is enhanced. For pulsation frequency of 2 Hz, the intensity of the vorticity slightly gets smaller values at this location. Since there is already considerable interaction between wake flow in groove and mainstream even for steady flow at Re = $5.5x10^3$, pulsation does not cause a dramatic change in vorticity field for this value of Reynolds number.

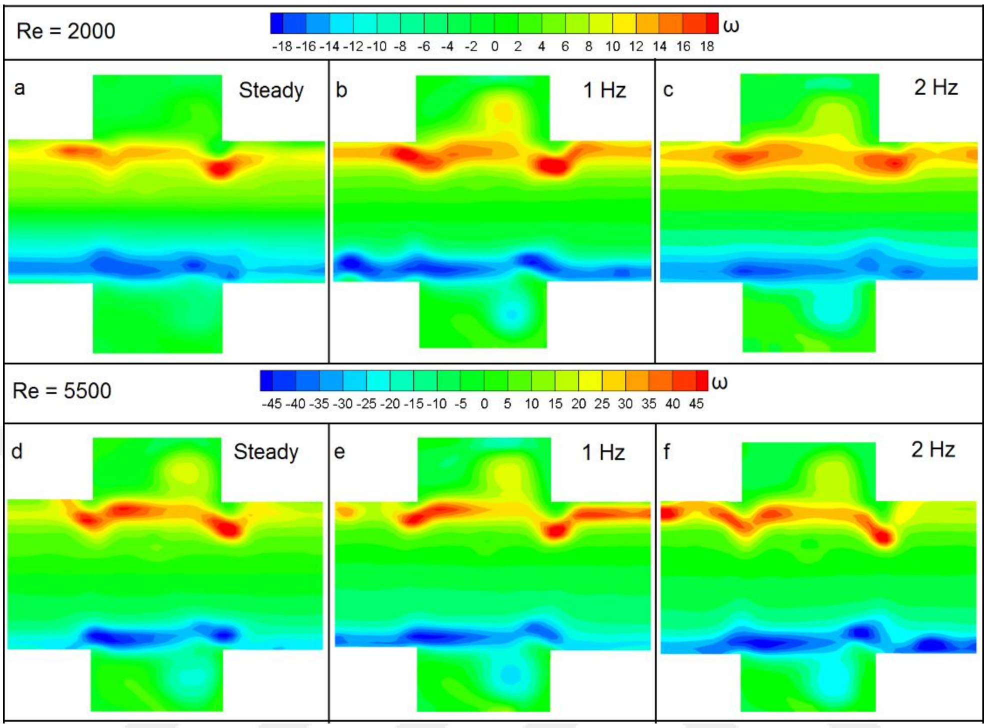

Figure 4.26. Time-averaged vorticity contours in groove 8.

Significant variation in Reynolds stress, $\overline{u'v'}/u_o^2$ occurs during a pulsation period. It is apparent from Figure 4.27 that when the flow is slowed down to its lowest velocity by a pulsator located downstream of the test section, medium and high Reynolds stress values fill the larger area in the channel. Konstantinidis et al. (2004) reported in their study that turbulence increases when coherent vortices are disintegrated into turbulent flow. A similar phenomenon is available in the low-velocity phase of the current case. As shown in Figure 4.26, in the low-velocity phase, the vortical structures concentrated in the shear layer in the previous phases, diffuse over the larger area in the channel and lost their magnitude during the diffusion process because of disintegration. When acceleration and peak velocity phases are investigated, it can be seen that significant Reynolds stress levels are seen only at the mouth of the groove since shaded vortices spread along with this location. There is not a considerable difference in the intensity of Reynolds stress between two pulsation frequencies. A noticeable increase is only seen in low-velocity phase of 2 Hz pulsation frequency.

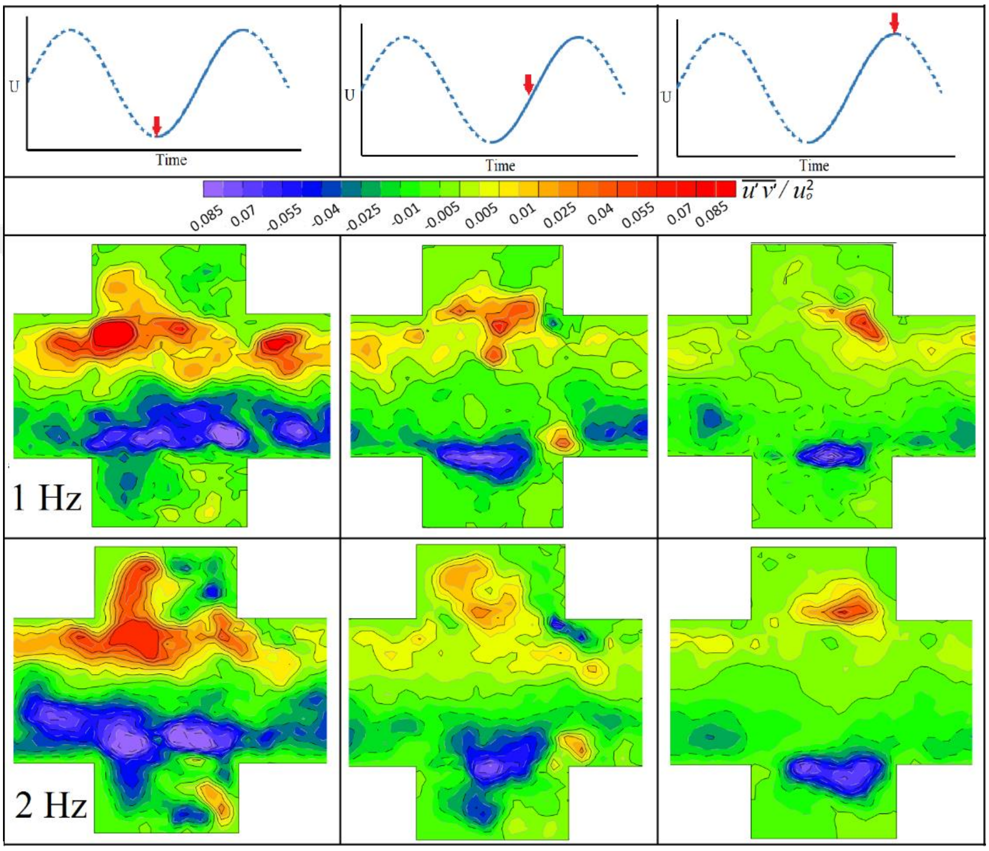

Figure 4.27. Reynolds stress at different phases of pulsation for 1 Hz and 2 Hz pulsation frequencies and Re = 5.5x10^3.

Like Reynolds stress, root mean square of the velocity component, u_{rms} also reach the highest level at low-velocity phase, as shown in Figure 4.28. In this phase, u_{rms} islands with high intensity are seen on separated shear layers; however, u_{rms} values near the central axis between the grooves are considerably lower than the shear layers developed along the grooves. At the downstream of the grooves, highly concentrated u_{rms} areas disappear but contours of the u_{rms} with moderate values merge at the central axis. Therefore; u_{rms} level on the central axis increase at downstream of the grooved section The. same phenomena are observed for both 1 Hz and 2 Hz pulsation frequencies. Moreover, for 2 Hz frequency u_{rms} is also intensified inside the grooves but similar intensification does not occur at 1 Hz frequency. During the acceleration and peak velocity phases u_{rms} areas with high intensity near the top and bottom grooves remain separated from each other and the area on the u_{rms} values in the central axis is low throughout the entire field of view.

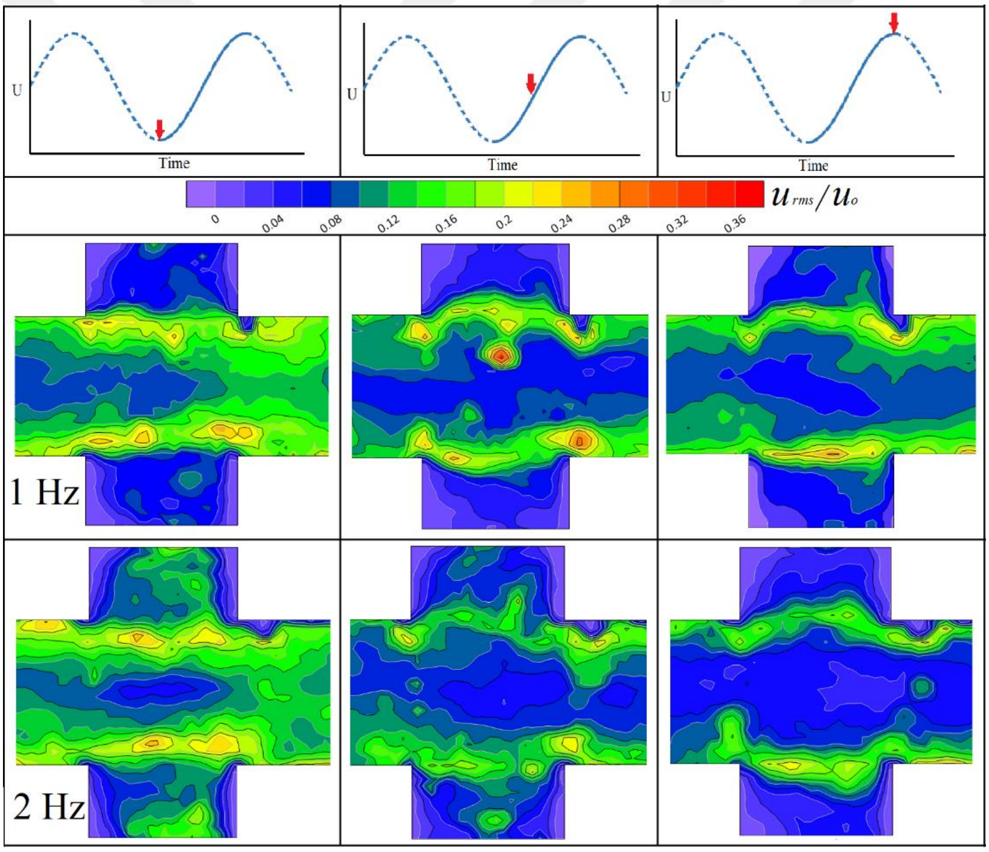

Figure 4.28. RMS of u velocity component, u_{rms} at different phases of pulsation for 1 Hz and 2 Hz pulsation frequencies and Re = 5.5x10^3.

Variation of root mean square of spanwise velocity component, v_{rms} under application of pulsation is more dramatic than u_{rms} (see Figure 4.29), this means that fluctuations in y-direction have an important contribution to change of Reynolds stress during the pulsation. High v_{rms} intensity was observed inside the grooves and in the mainstream region between the grooves for the low-velocity phase of pulsation. At the acceleration phase, v_{rms} values at the mainstream reduce and local peaks are seen inside the grooves. When the peak velocity phase is reached, the v_{rms} intensity over mainstream reaches its minimum value over the entire oscillating flow period.

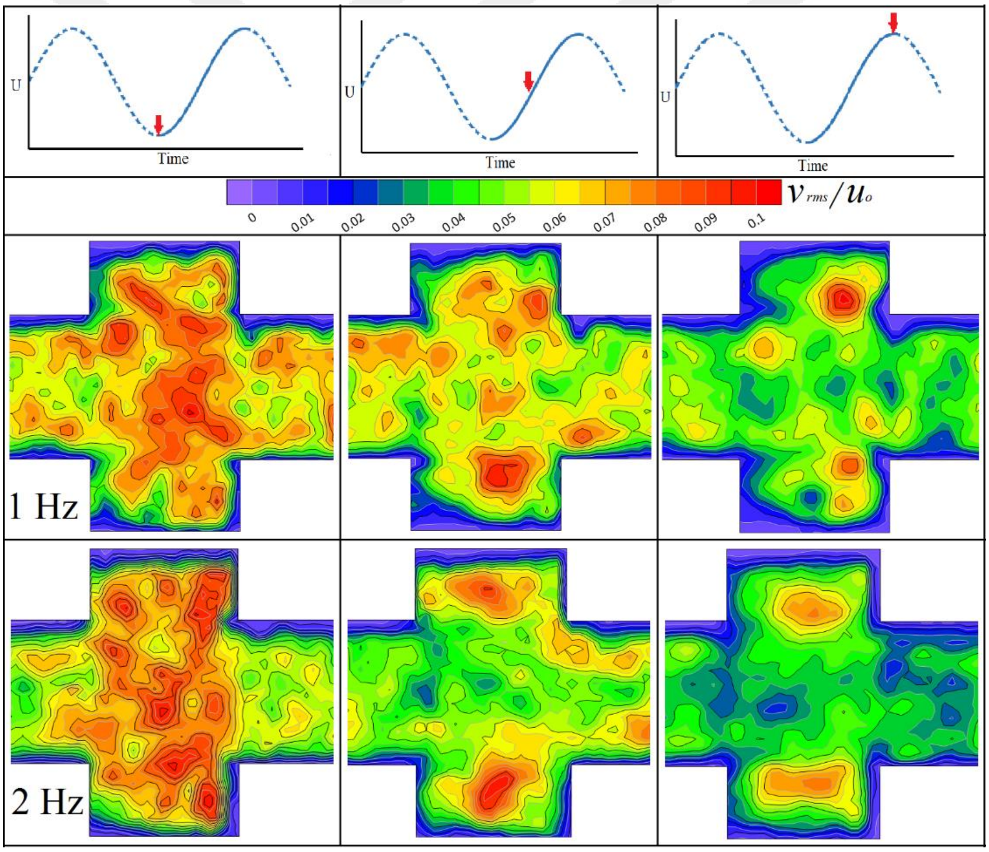

Figure 4.29. RMS of v velocity component, v_{rms} at different phases of pulsation for 1 Hz and 2 Hz pulsation frequencies and Re = $5.5\text{x}10^3$.

When the Reynolds number, *Re* decreases to $2x10^3$, the phase angles in which low and high Reynolds stresses are seen do not change as shown in Figure 4.30. However, the effect of 1 Hz and 2 Hz frequencies on Reynolds stress differs from the higher Reynolds number. At 1 Hz pulsation frequency and the low velocity phase, high Reynolds stress values fill the entire mainstream domain, but at 2 Hz pulsation frequency, the similar high magnitude of Reynolds stress distributions are seen in limited regions mostly they appear along with the separated shear layers over the groove space. Reynolds stress reduces at the next two phases of the pulsation ($\Omega t = \pi$ and $\Omega t = 5\pi/2$) as it is expected.

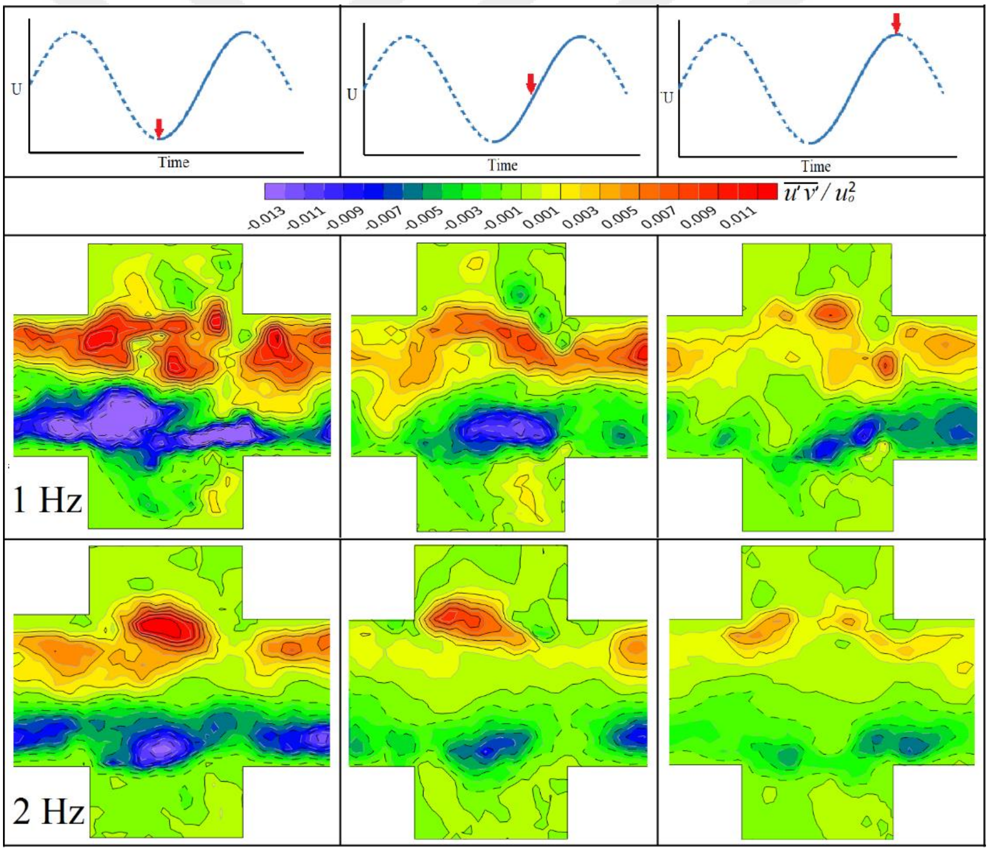

Figure 4.30. Reynolds stress at different phases of pulsation for 1 Hz and 2 Hz pulsation frequencies and Re = $2x10^3$.

Streamlines are presented for the channel with the bottom wall shifted as *L*/4 in the streamwise direction in Figure 4.31. Reynolds number is selected as $5.5x10^3$, and the effect of two different pulsation frequencies is investigated in the figure. Shifting the wall does not cause a noticeable difference in flow pattern with the pulsating flow just as it happens in the steady inlet velocity case. For each phase of the flow pulsation, circulation regions inside the grooves exhibit similar behavior which is seen in the no wall shifting case. As is discussed before, the interaction between grooves located opposite walls is very limited for the selected geometrical configuration of the grooved channel. Figure 4.31 shows that flow pulsation can not enhance the interaction between the groove therefore each groove continues to behave individually.

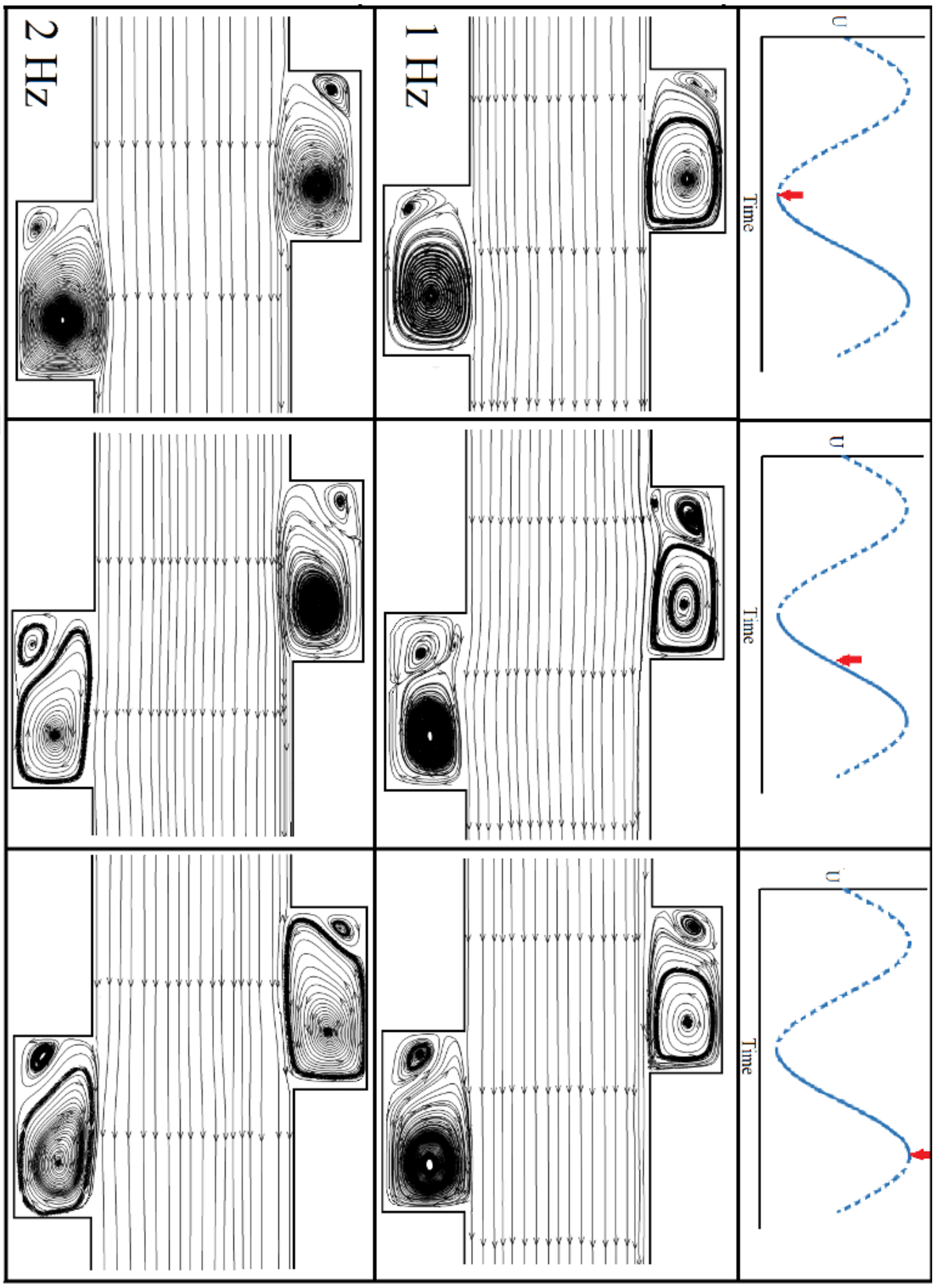

Figure 4.31. Effect of shifting the channel walls as *L*/4 on flow patterns at different phases of the pulsation for 1 Hz and 2 Hz pulsation frequencies and Re = 5.5x10^3.

Figure 4.32 demonstrates streamlines for the bottom wall shifted as *L*/2. In this wall shifting configuration, there is a non-grooved section on the opposite of each groove. Since the horizontal distance between grooves on the opposite walls is the greatest in this case, the effect of interaction between grooves on the opposite wall is minimalized. The flow patterns in each groove show that even the distance between grooves on opposite walls is the furthest; there is no substantial difference occur in the flow patterns inside the groove space. These results confirm that interaction between grooves can be ignored in this type of grooved channel regardless inlet flow is steady or pulsating. If more interaction between the grooves is desired, either the groove aspect ratio or distance between upper and lower walls must be changed.

Time-averaged vorticity contours are given in Figure 4.33 for different shifted wall configurations at Re = $5.5x10^3$ and 1 Hz pulsation frequency. As the figure indicates vortical structures with high intensity are seen near the solid surfaces, especially the downstream of the groove's sharp corners. However, the magnitude of the vorticity is relatively low at the central axis of the channel. Investigation of instantaneous vortical structures for a pulsation period which is shown in Figure 4.26 for non-shifted wall configuration, reveals that some part of shaded vortices reaches the center of the channel however during the next phase angles of the pulsation cycle, they are disintegrated and lost their part of intensity. Therefore, vortical flow structures departed from the shear layers can not keep their presence beyond the central axis, so it can be said that there is no considerable interaction between shear layers with high vorticity magnitude which are located near the top and bottom walls of the channel. Because of this poor interaction between shear layers, the vorticity field does not exhibit a significant difference even if channel walls are shifted.

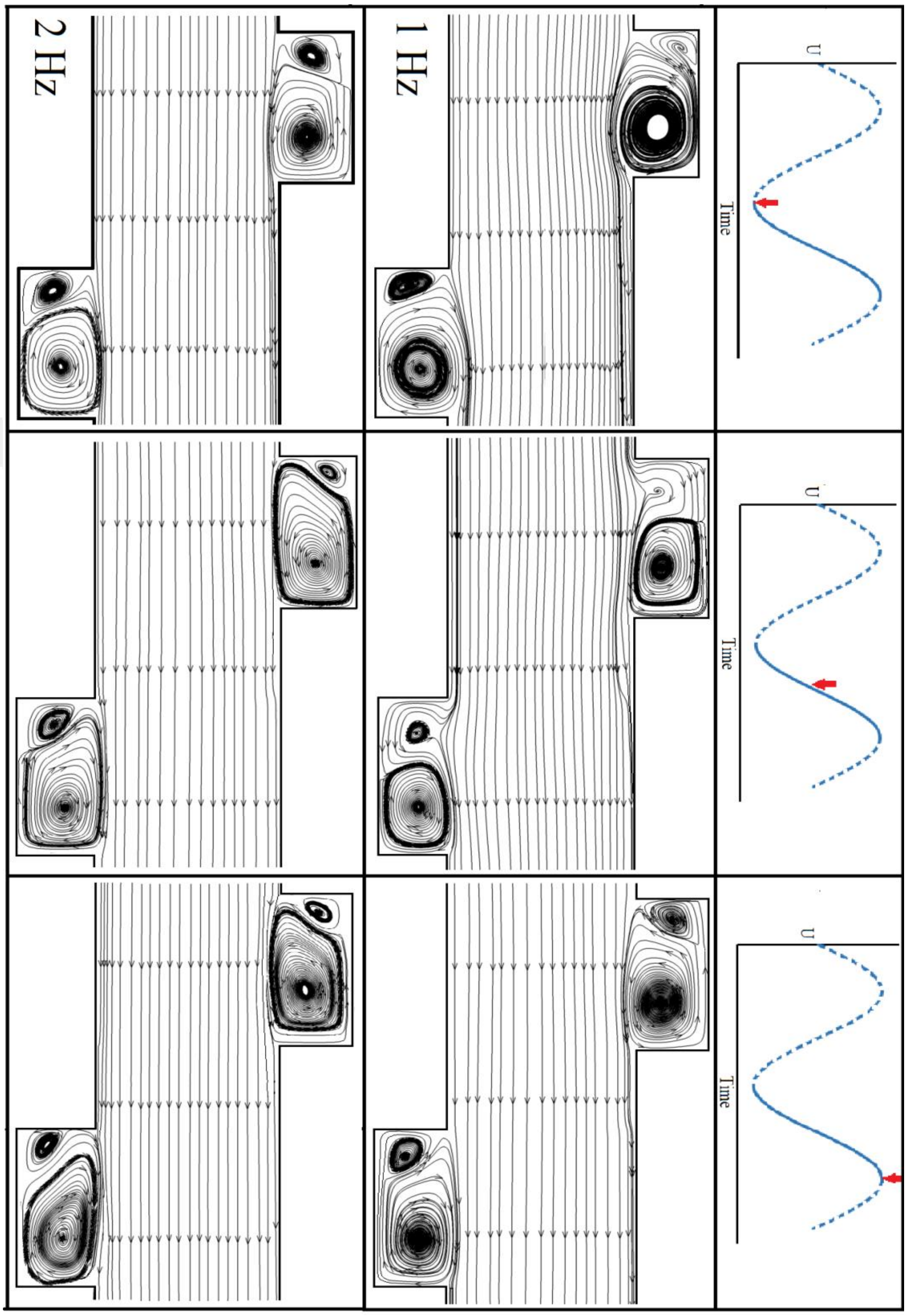

Figure 4.32. Effect of shifting the channel walls as $L/2$ on flow patterns at different phases of the pulsation for 1 Hz and 2 Hz pulsation frequencies and $Re = 5.5x10^3$.

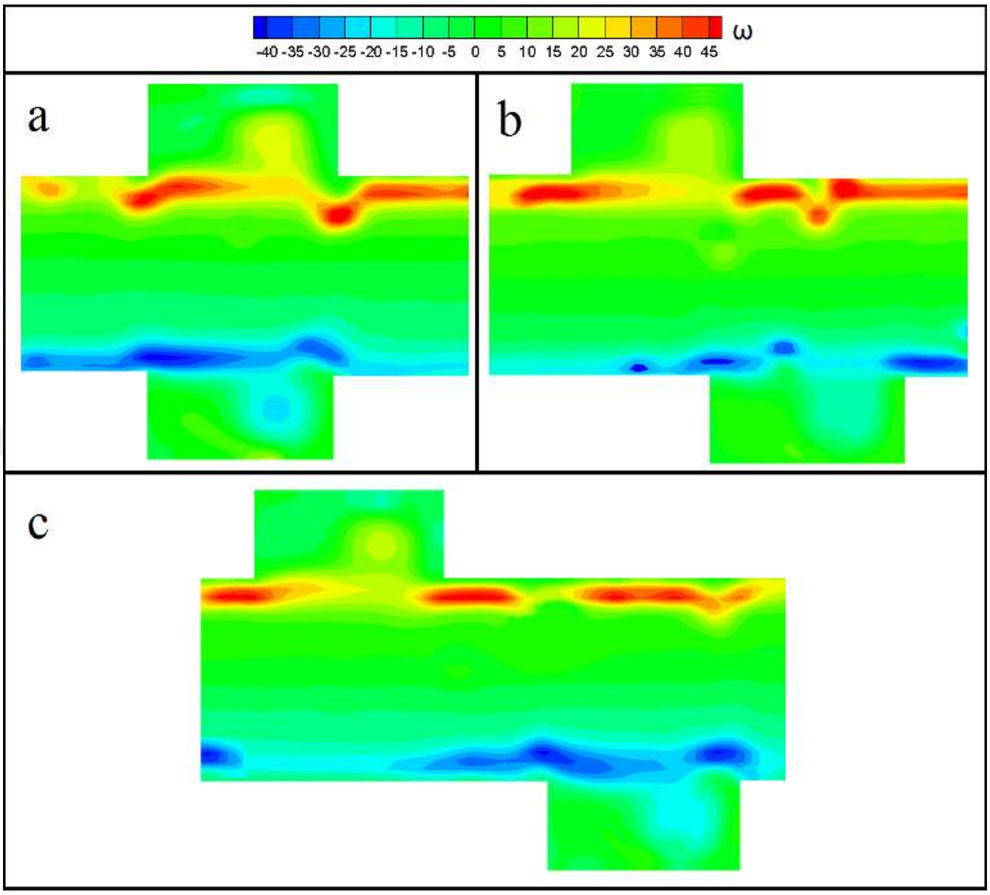

Figure 4.33. Time-averaged vorticity contours for different shifted wall configurations at Re = $5.5x10^3$ and 1 Hz pulsation frequency.

Figure 4.34 shows that conditions described for 1 Hz pulsation frequency are also available for 2 Hz pulsation frequency, i.e., the increasing frequency can not enhance the interaction between shear layers located in the vicinity of two opposite walls. However, even if the vortical flow structures departed from the shear layers and disintegrated quickly, they still impact the turbulence fluctuations. For this reason, investigation of velocity fluctuations for different shifted wall configurations is still important even though wall shifting does not cause a substantial difference in massive fluid transfers and structure of flow patterns.

Therefore, patterns of Reynolds stress are presented for different shifted wall cases in the following figures to observe turbulence statistics.

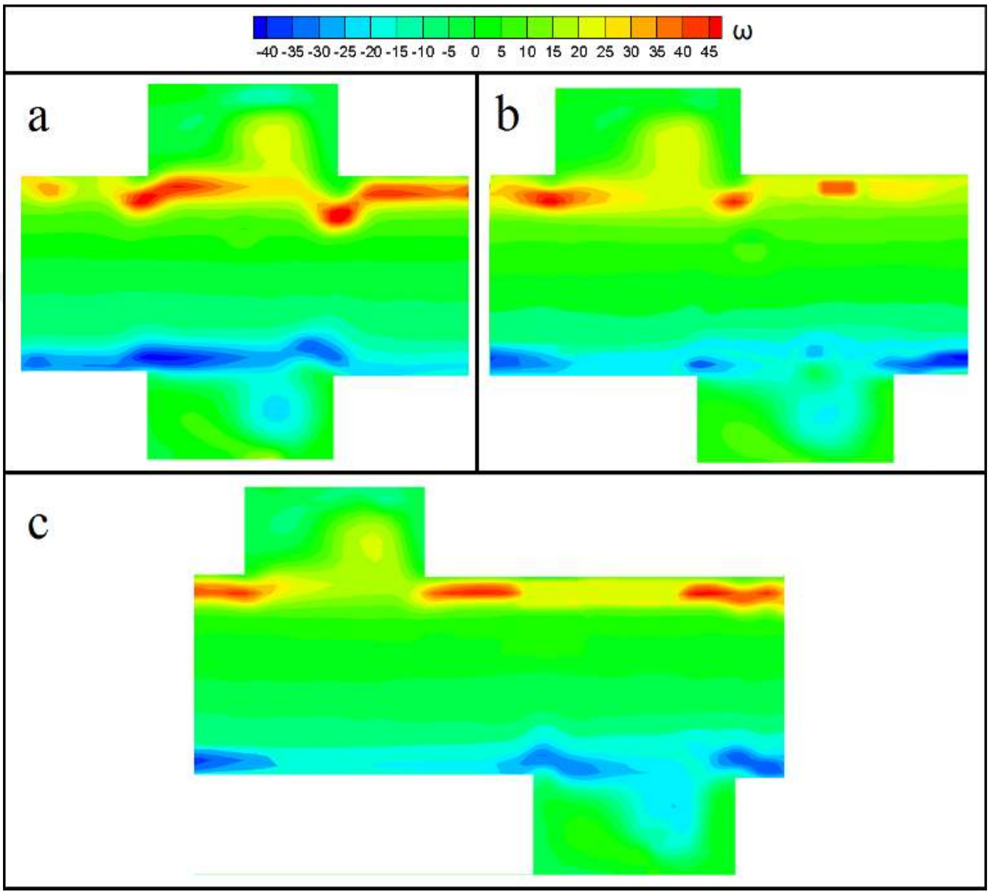

Figure 4.34. Time-averaged vorticity contours for different shifted wall configurations at Re = $5.5x10^3$ and 2 Hz pulsation frequency.

Distributions of Reynolds stress which are shown in Figure 4.35, reveals that shifting the bottom wall as *L*/4 causes a difference in turbulence intensity compared to no shifted wall configuration. When the Reynolds stress in Figure 4.27 and Figure 4.30 are compared with Figure 4.35 for low-velocity phases it can be seen that high and moderate Reynolds stress levels are more propagated through the channel in Figure 4.35. This situation is more evident for 2 Hz pulsation frequency than 1 Hz frequency case. The reason for the enhancement in turbulence intensity can be explained by the fact that the downstream corner of the upper groove and upstream corner of the corresponds to the groove mouth on the opposite wall. As it is mentioned in previous sections, the corners of the grooves are important for the generation of velocity fluctuations. When the corner of one groove is located across the separated shear layer of the groove placed on the opposite wall, an increase in turbulence intensity is occurs in the region of the channel which is located between two opposing grooves. During the acceleration and high-velocity phases, Reynolds stress levels are reduced as happens in other groove position configurations. However, islands of high Reynolds stress seen on separated shear layers are still larger than no shifted wall configuration. An increase of the horizontal distance between upper and lower groove to $L/2$ causes a reduction of the Reynolds stress levels back to the values in the no-shifted wall configuration (see Figure 4.36). As seen in both shifted wall configurations the positions of the grooves on opposite walls with respect to each other are important for the increase in the turbulence level of flow passing through the grooved channel. Despite groove positions do not cause a substantial difference in flow pattern on the macroscopic scale, they still impact vortical flow structures with small scales. Since the enhancement of the turbulence mixing is beneficial in terms of heat transfer, positions of the grooves should be considered for obtaining the maximum heat transfer rate. In the next section, heat transfer values are presented for different shifted wall configurations under the pulsating flow conditions.

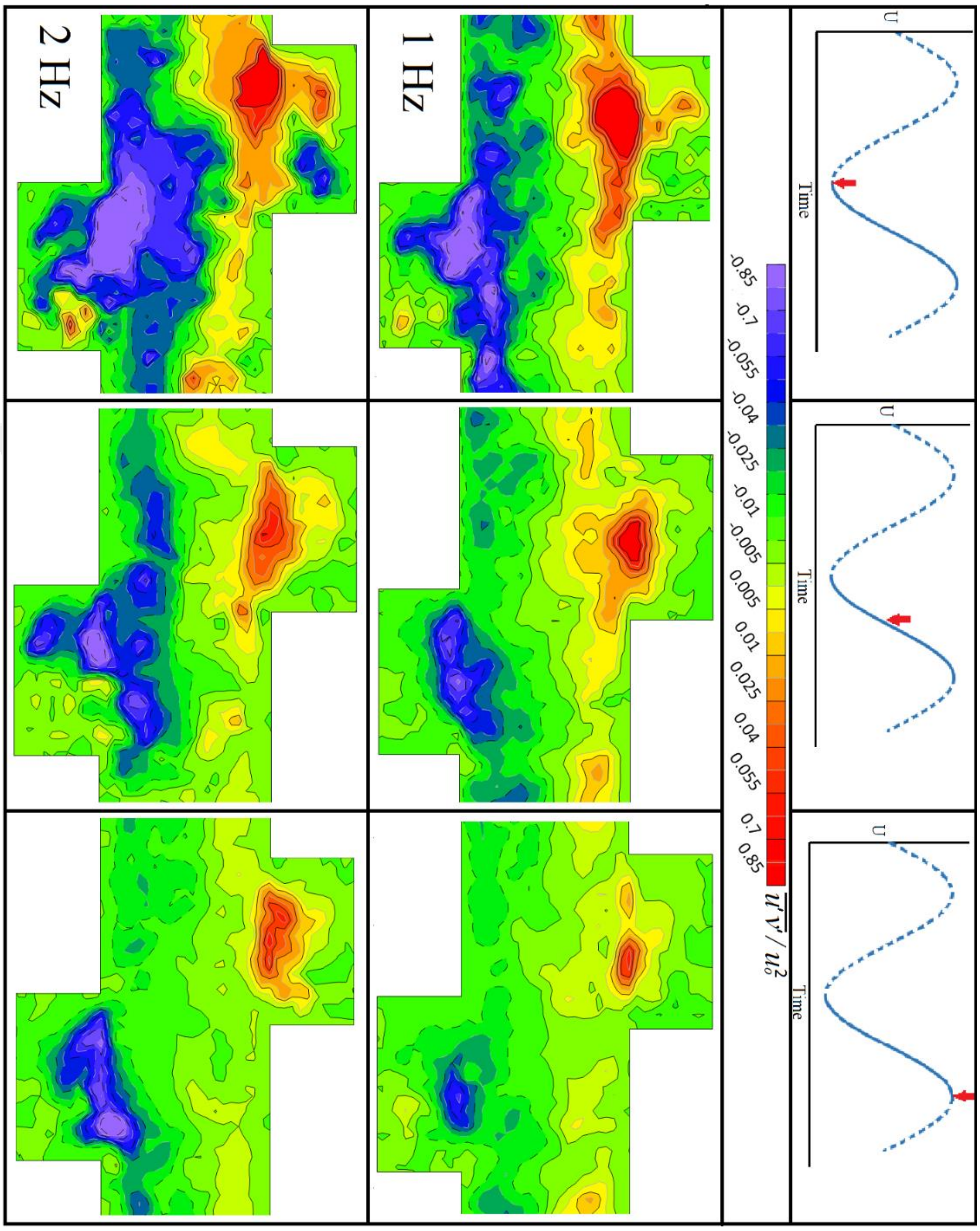

Figure 4.35. Effect of shifting the channel walls as L/4 on Reynolds stress at different phases of the pulsation for 1 Hz and 2 Hz pulsation frequencies and Re = 5.5x10^3.

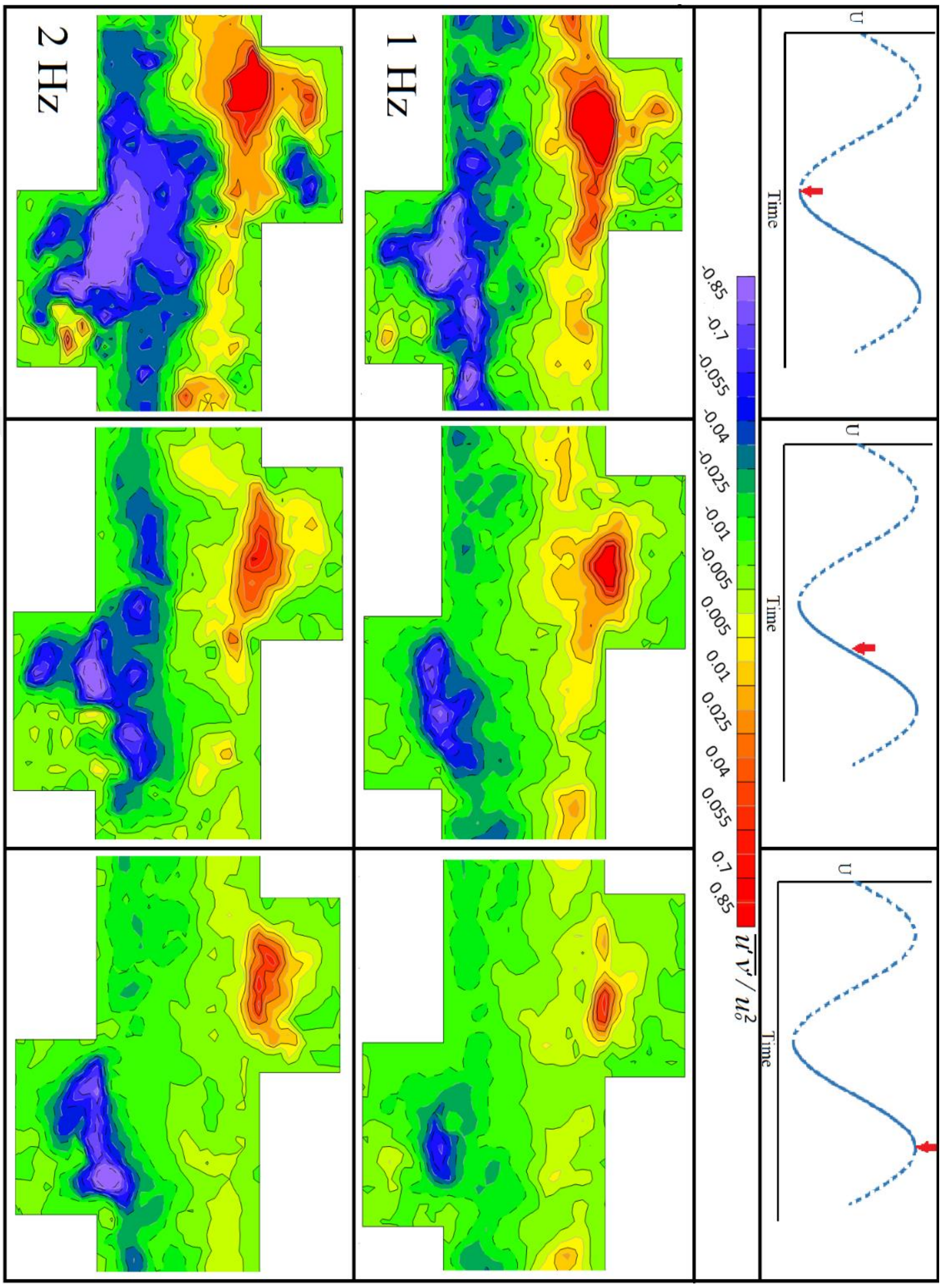

Figure 4.36. Effect of shifting the channel walls as *L*/2 on Reynolds stress at different phases of the pulsation for 1 Hz and 2 Hz pulsation frequencies and Re = 5.5x10^3.

4.4. Heat Transfer and Pressure Drop in Pulsating Flow

As discussed in the previous sections, the pulsating flow has an important effect on both enhancing turbulence mixing and improving the fluid transfer between the wake flow of grooves and mainstream. Results of these effects are shown itself as an increase in heat transfer which is presented in Figure 4.37 and Figure 4.38. When the variation of the Nusselt number, *Nu* is investigated with respect to pulsation frequency, *F,* it can be seen that the Nusselt number, *Nu* does not increase steadily with increasing pulsation frequency, *F*. Instead, it reaches a maximum level at a certain frequency and then starts to get reduced when pulsation frequency, *F* is increased more. The reason for this situation can be explained by recalling the flow hydrodynamics given in Figures 4.22 and 4.24. These two figures reveal that an increase in pulsation frequency does not always cause an increase of interaction between wake flow in grooves and mainstream. In higher frequencies, successive variation of the flow velocity happens more frequently; as a result, the efficiency of the fluid transfer between wake flow of groove space and mainstream gets reduces. This situation also affects the heat transfer results. Enhancements in heat transfer start to be reduced with increasing pulsation frequency, *F* and eventually, the Nusselt number, *Nu* values gets closer to non-pulsating flow heat transfer values at very high frequencies. The decrease of the difference between steady and pulsating flow heat transfer values at high frequencies shows, that despite the butterfly valve (flow pulsator) rotating very fast in high frequencies creates a fluctuation in the flow, the flow's behavior in high frequencies resemble the steady flow.

Heat transfer enhancement by the implementation of pulsating flow is demonstrated by using thermal enhancement factor, *E* in Figure 4.39 and Figure 4.40. Values of the thermal enhancement factor, *E,* indicate that flow pulsation is more effective in increasing the heat transfer in low Reynolds numbers.

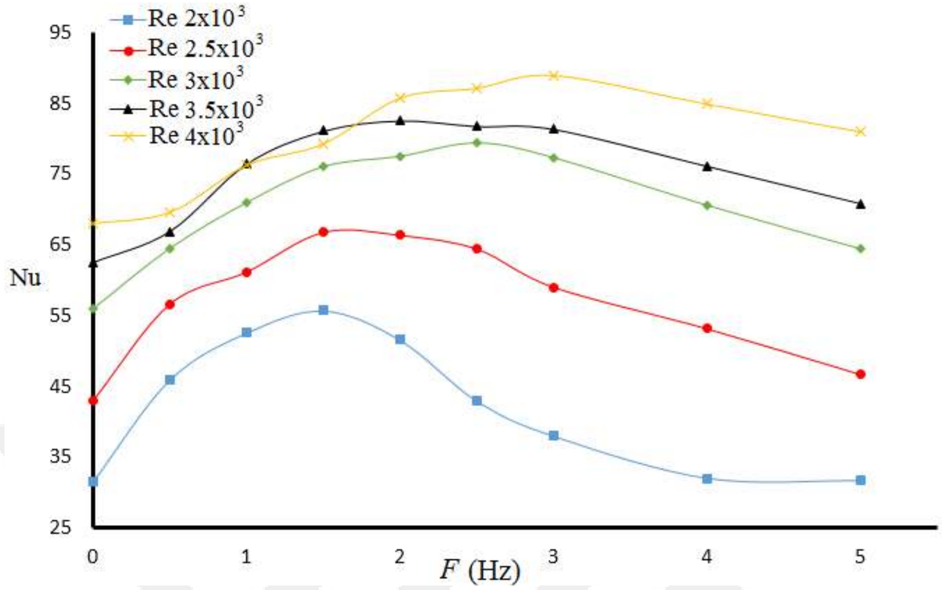

Figure 4.37. Effect of pulsation frequency on Nusselt number between Re $2x10^3$ and $4x10^3$.

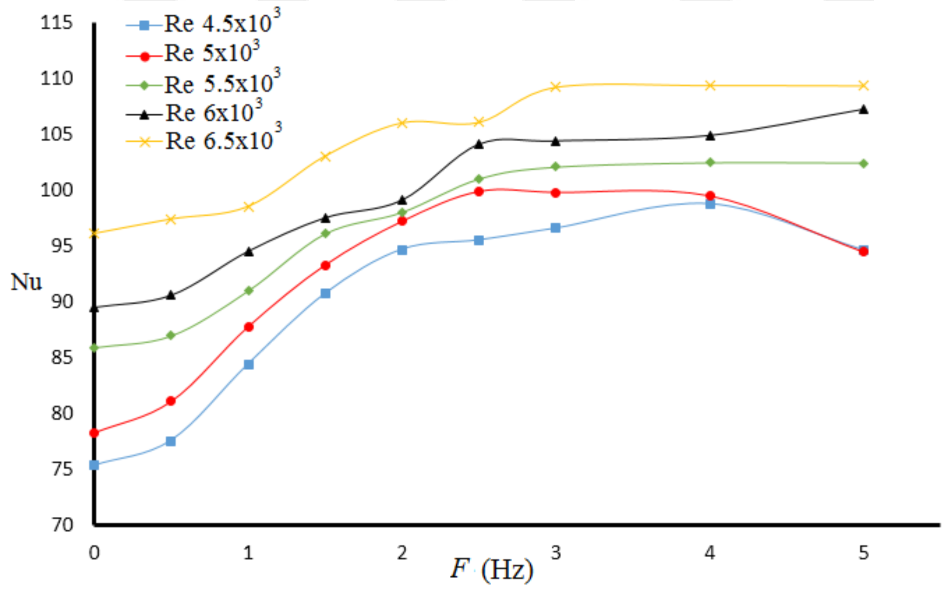

Figure 4.38. Effect of pulsation frequency on Nusselt number between Re $4.5x10^3$ and $6.5x10^3$.

For the Reynolds number of $2x10^3$, heat transfer enhancement becomes 1.77 times greater than steady flow at the 1.5 Hz pulsation frequency. However, with the increase of the Reynolds number, *Re*, the peak value of the heat transfer enhancement starts to be reduced and becomes 1.14 for Re = $6.5x10^3$ and F = 5 Hz. This situation is expected because, in low Reynolds numbers, the low level of interaction between circulating flow regions in grooves and core flow occurs resulting in poor turbulence mixing. Therefore any disturbance of flow caused by pulsation results in a more pronounced enhancement in heat transfer. As is discussed before, there is already considerable turbulence mixing in the channel for higher Reynolds numbers, and interaction between flow in grooves and mainstream is not as poor as it happens in low Reynolds numbers. For this reason contribution of pulsating flow on heat transfer becomes less. Another important difference seen between Reynolds numbers is the frequency of the pulsation in which peak heat transfer enhancement occurs.

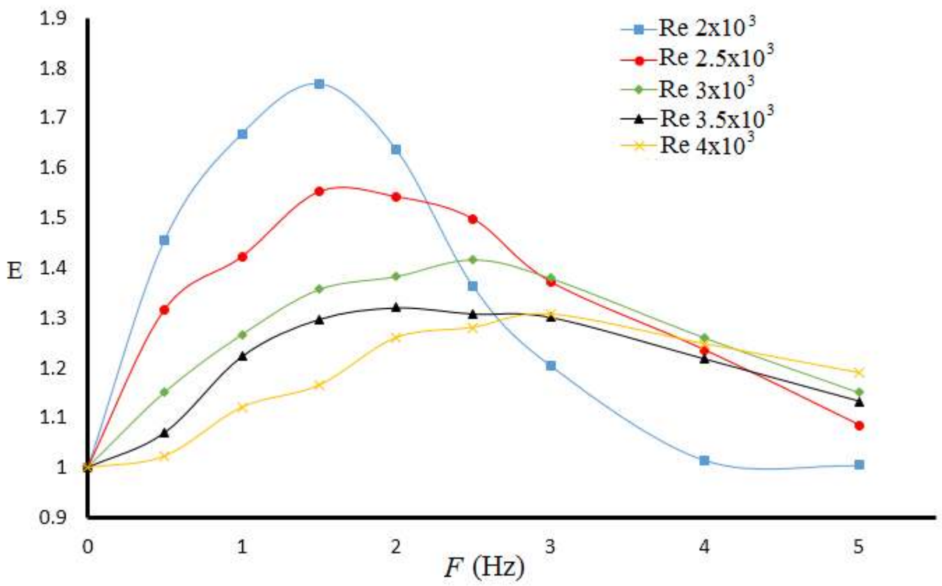

Figure 4.39. Thermal enhancement factor in different pulsation frequencies between Re $2x10^3$ and $4x10^3$.

In low Reynolds numbers, the peak value of the enhancement is seen at low frequencies, and heat transfer enhancement, *E* reduces rapidly after the peak, however as the Reynolds number, *Re* increases, the frequency that causes peak enhancement rises, and reduction in the heat transfer enhancement becomes less dramatic. Heat transfer results presented in this section indicate there is an optimum value of the frequency for the pulsating flow through a rectangular grooved channel, and the value of the optimum frequency strictly depends on the Reynolds number.

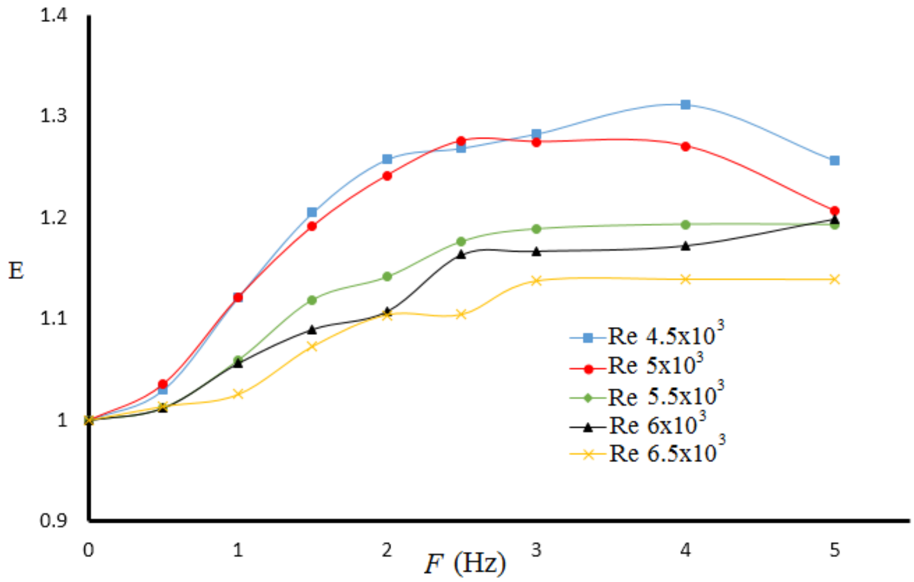

Figure 4.40. Thermal enhancement factor in different pulsation frequencies between Re $4.5x10^3$ and $6.5x10^3$.

Effect of pulsation frequency on friction factor is shown in Figure 4.41 and Figure 4.42. As it is seen from these figures, the change of the friction factor with respect to pulsation frequency is not consistent. The friction factor reaches the maximum value at 1-1.5 Hz pulsation frequencies. It reduces until 3 Hz and then starts to rise again for higher frequencies. It is believed that non-consistent variation of friction factor arises from the insufficient sampling rate of differential pressure transmitter. The pressure transmitter used in this study has a 480 ms response time. For this reason, measuring the pulsating pressure in high frequencies by using such a slow responding instrument is not appropriate. It seems that only friction factor values between 0-1.5 Hz frequencies are reliable.

The diameter of the disc of the clape is divided by the open hole of the clape, Dd/Dh is equal to 0.80, or the porosity of the clape is P=0.2 between throttle disc diameter and clapper hole diameter. When there is no rotation of the disc, the hydrodynamics of flow around the disc is constant. But the disc is rotated in order to create pulsatile flow. That is, in the case of pulsatile flow, the flow characteristics change continuously based on the continuous variations of porosity of the clape. The disc rotates to create periodic pulsatile flow. During the cycle, half of the disc moves against the flow direction. This disc rotation causes back pressure variation. The flow in the test region causes acceleration and declaration in fluid flow with effects of the pulsations created in the fluid flow. In other words, in addition to affecting the boundary layer development sequentially in the corrugated channel, the grooves also affect the boundary layer change in these periodic pulsatile flow structures. In conclusion, a higher level of entrainment occurs between the wake flow region placed in the groove space and the core flow regions with the pulsation effect. As seen in figures. Pressure losses are presented in terms of the friction factor. However, the mixing process of fluid in pulsatile flow causes more pressure losses. That is why the value of the friction factor is nearly two times higher than the friction factor of steady flow under the same average Reynolds number. When the pulsation frequency of flows more than 1 Hz, the rotational speed of the disc increases; this results in a change in the velocities inside the groove spaces. The variation of the velocities between 1 Hz and 2 Hz frequencies is shown in Figures 4.43-4.48. As the figures indicate flow pulsation with 2 Hz causes considerable higher velocity values overall area inside the groove. These velocity values are important in terms of giving an idea about the reason for the decrease in friction factor. It can be derived from the local lost formula; $f = \Delta P \frac{D}{L} \frac{2}{\rho u^2}$. As the formula indicates friction factor is inversly propotional to the square of the flow velocity. Therefore the increase of the flow velocity cause a reduction in friction factor.

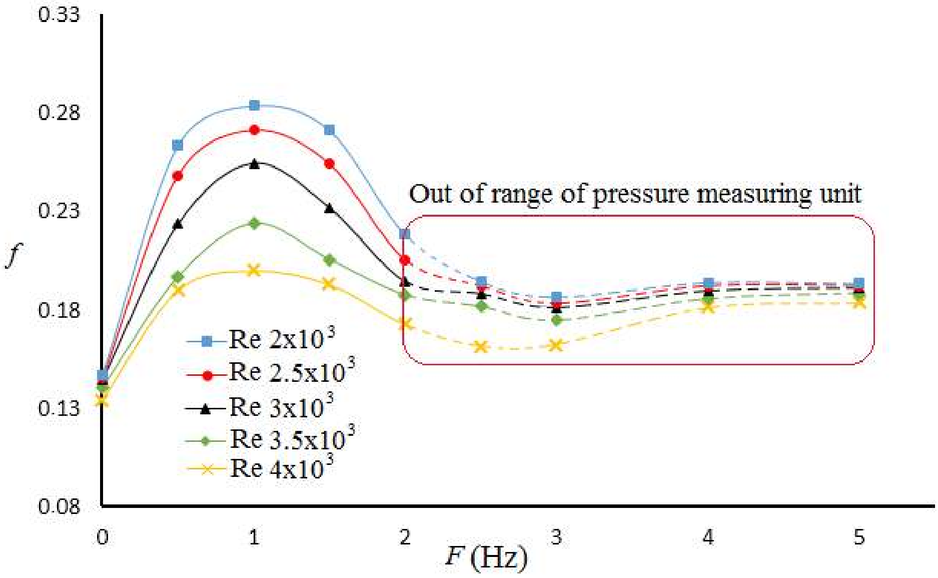

Figure 4.41. Effect of pulsation frequency on friction factor between Re $2x10^3$ and $4x10^3$.

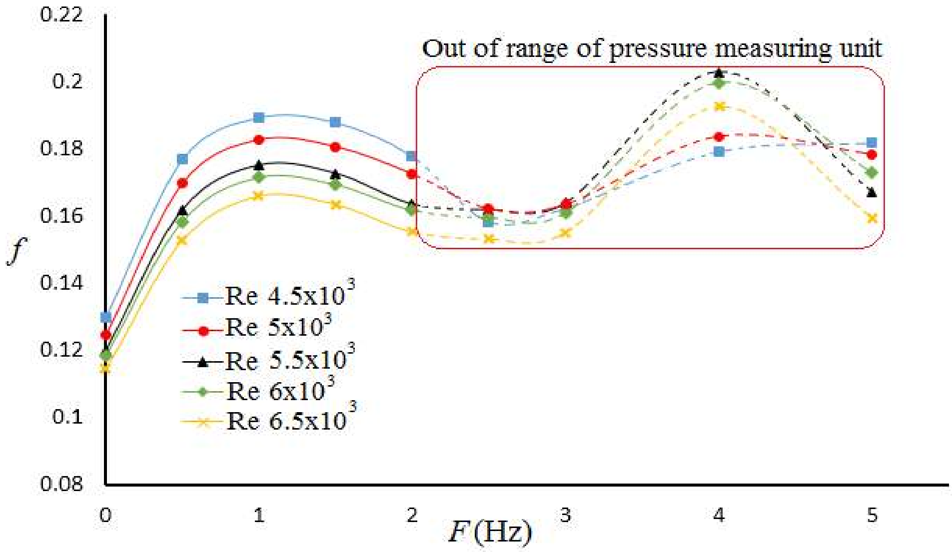

Figure 4.42. Effect of pulsation frequency on friction factor between Re 4.5×10^3 and 6.5×10^3.

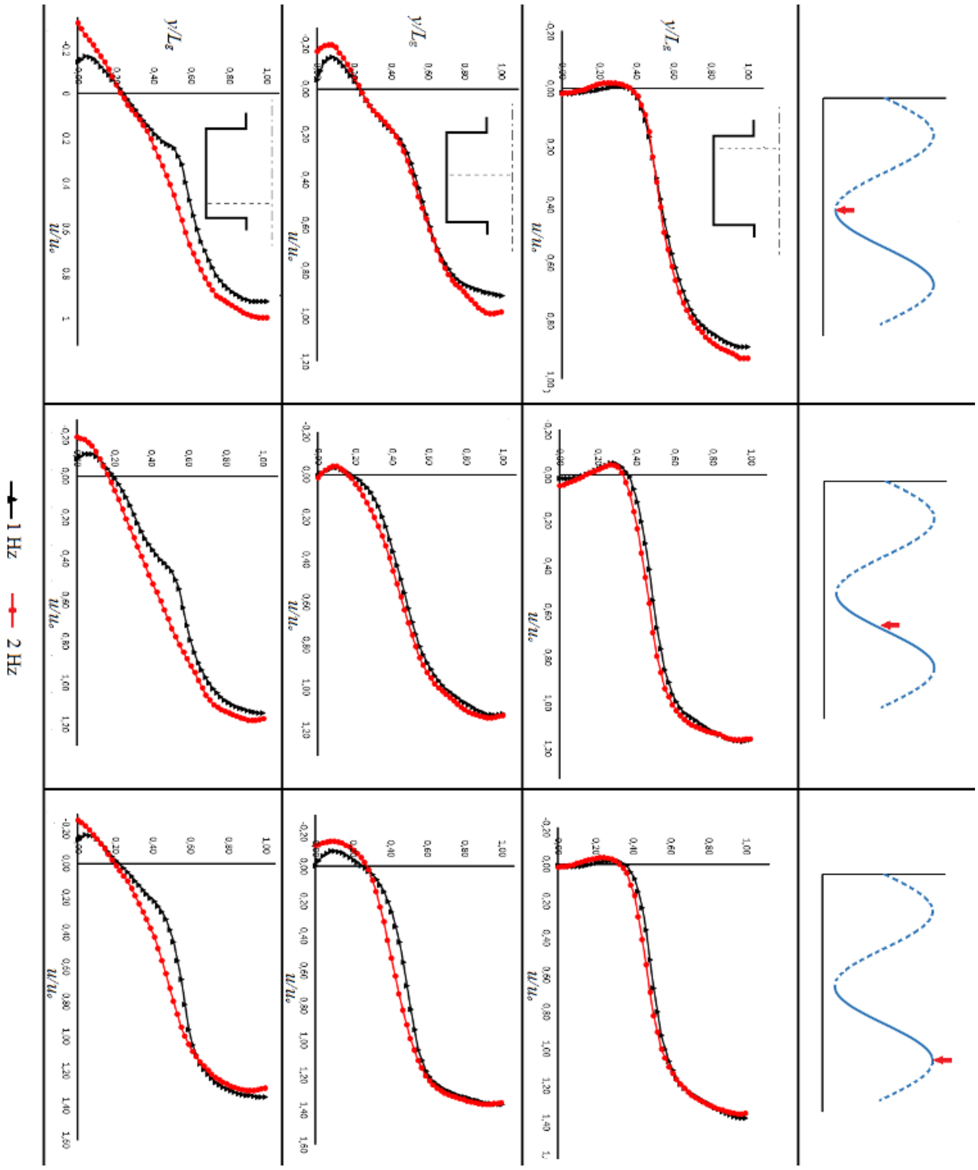

Figure 4.43. Variation of streamwise velocity along diffrent vertical lines in groove for Re = 5.5×10^3.

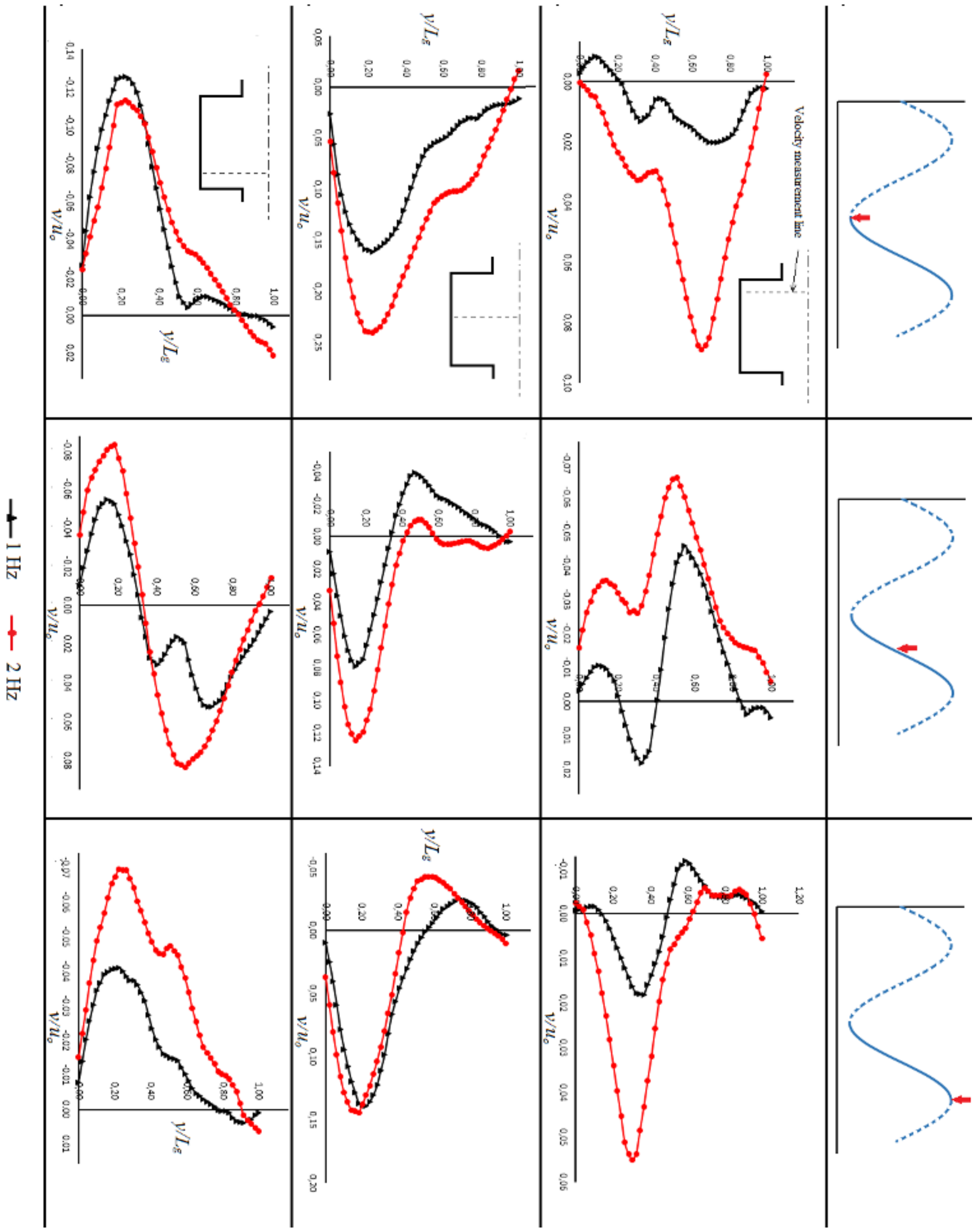

Figure 4.44. Variation of transverse velocity along diffrent vertical lines in groove for Re = 5.5 x 10^3.

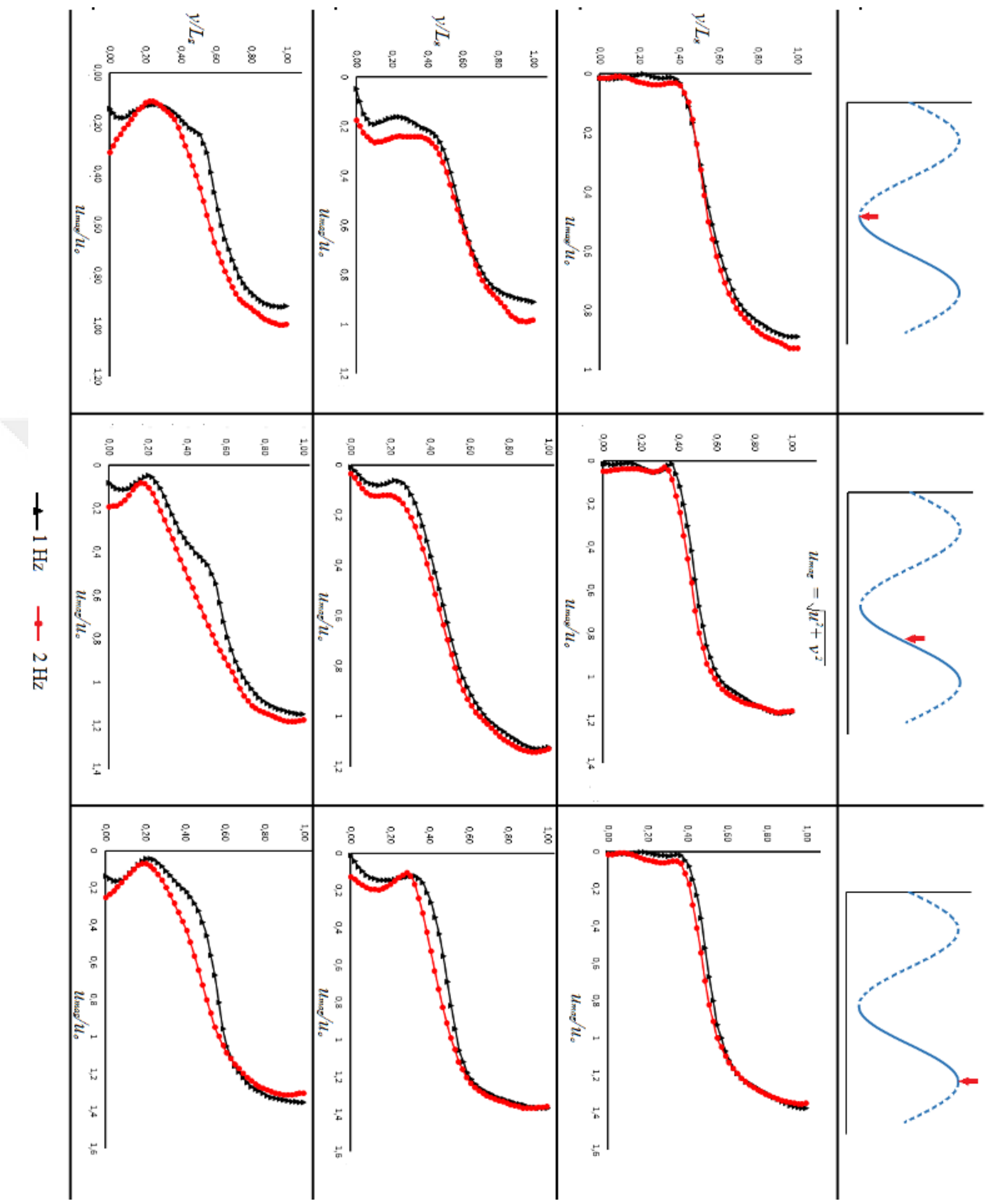

Figure 4.45. Variation of velocity magnitude along diffrent vertical lines in groove for Re = 5.5 x 10^3.

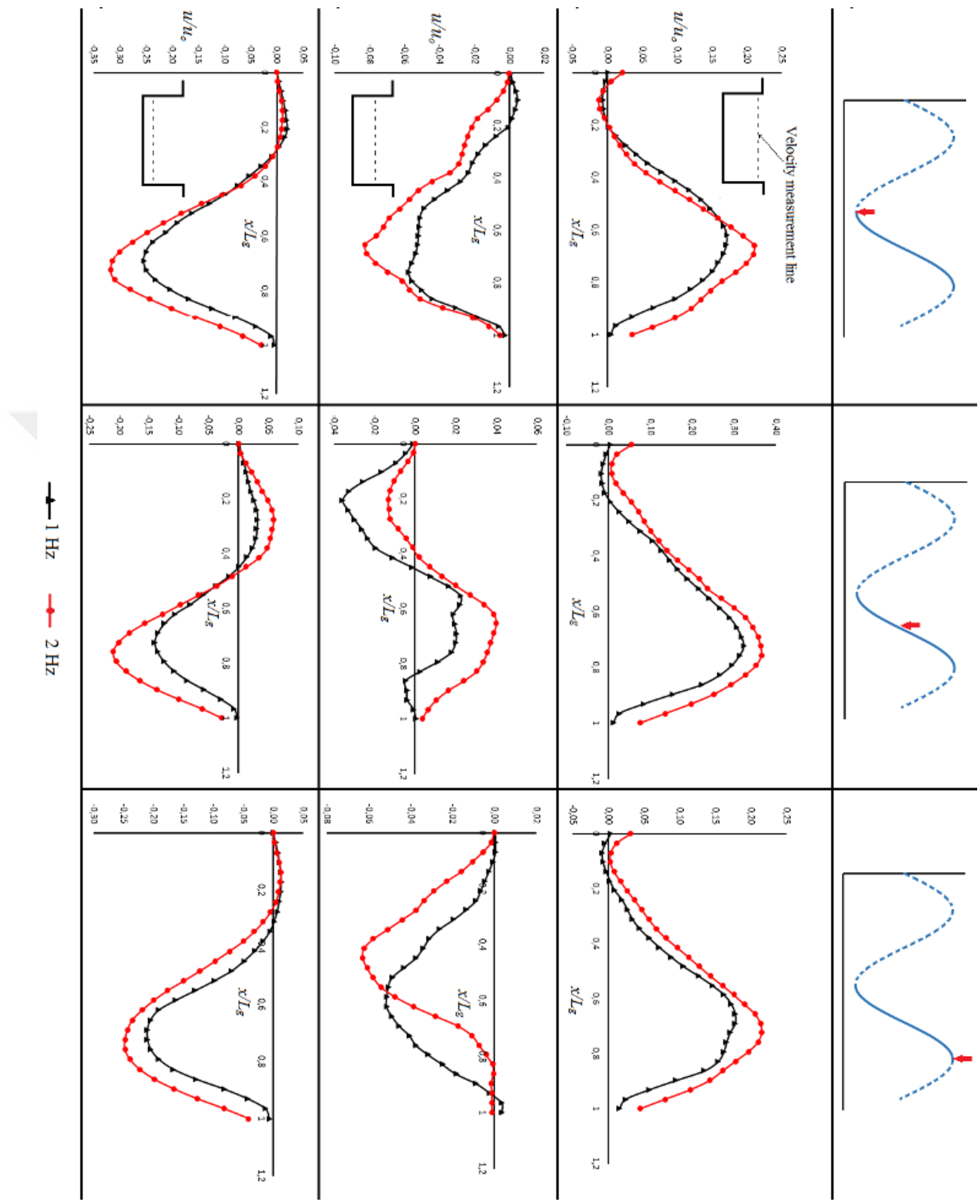

Figure 4.46. Variation of streamwise velocity along diffrent horizontal lines in groove for Re = 5.5 x 10^3.

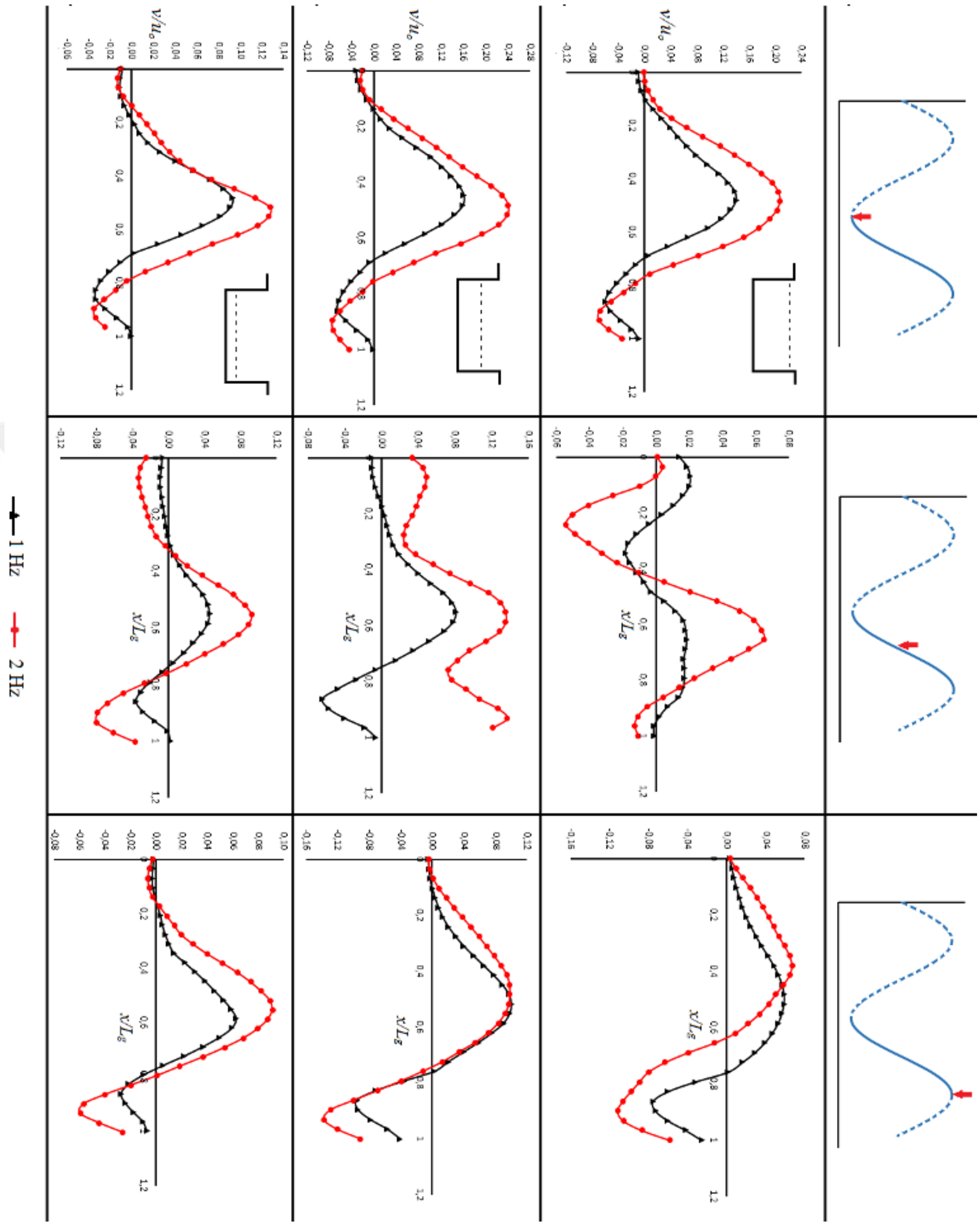

Figure 4.47. Variation of transverse velocity along diffrent horizontal lines in groove for Re = 5.5 x 10^3.

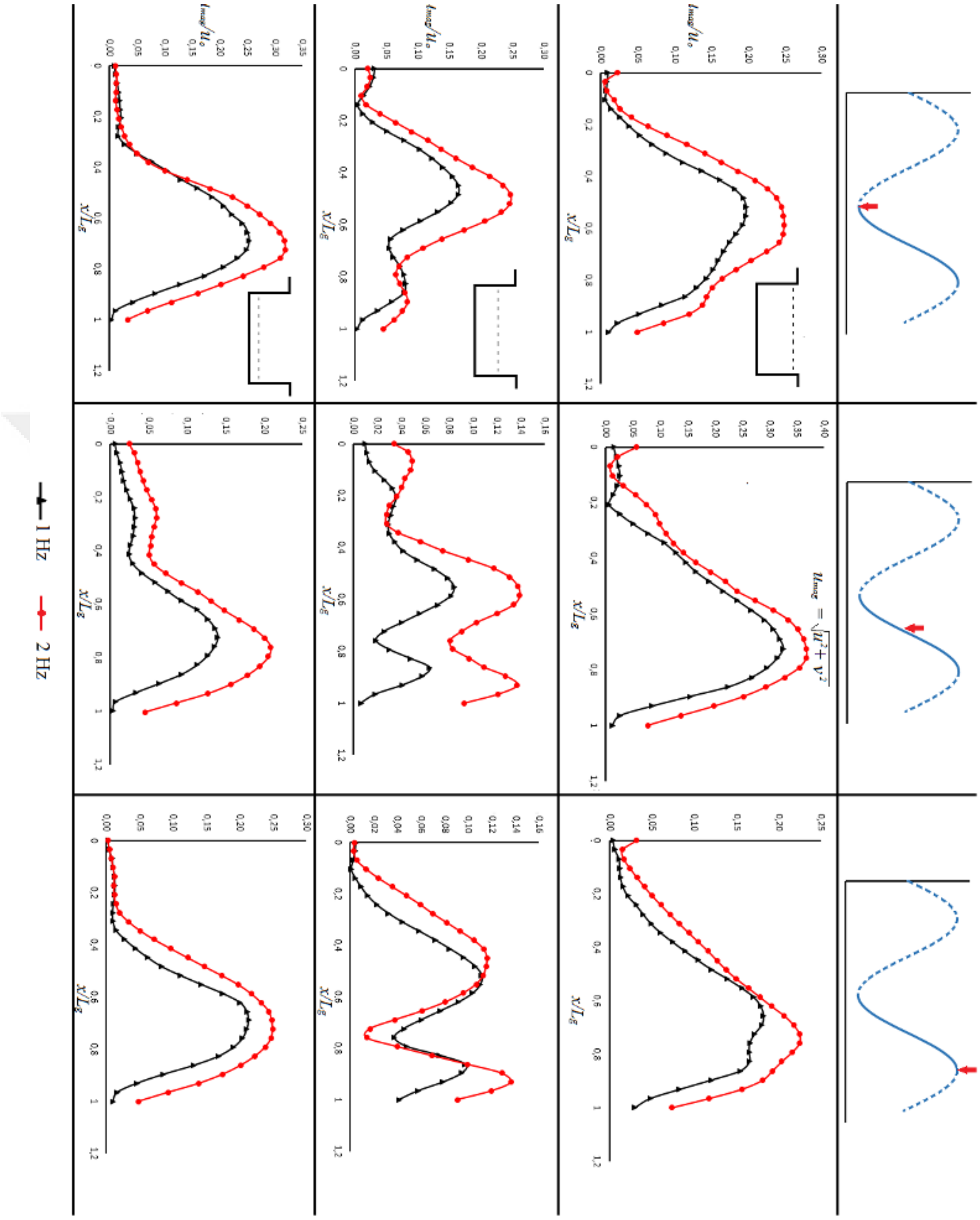

Figure 4.48. Variation of velocity magnitude along diffrent horizontal lines in groove for Re = 5.5 x 10^3.

The thermal performance factor, *TPF* is given in Figures 4.49 and 4.50 for all Reynolds numbers considered in present study. It is worth mentioning that *TPF* was not calculated higher than 2 Hz since the friction factor, *f* values are not reliable for higher frequencies than 2 Hz. That is, the frequency of the differential pressure measuring device is limited to 2 Hz frequency. In these figures *TPF* is a measure of heat transfer enhancement, pressure drop increase ratio compared to steady flow in the grooved channel. As the figures indicate TPF values are greater in low Reynolds numbers. This is expected because as it is mentioned before heat transfer enhancement of pulsating flow is much better at low Reynolds number, so despite the rise of pressure drop higher *TPF* values are seen in low Reynolds numbers. However, as the Reynolds number increases heat transfer enhancement capability of the pulsating flow decreases but the same rate of decrease does not occur in the friction factor, *f*. Therefore *TPF* values become less than unity near 1-1.5 Hz. Reduction in *TPF* is more evident for higher Reynolds numbers (Re > $4x10^3$). Near 2 Hz frequencies *TPF* starts to rise again because friction factor, *f* reduces at this frequency.

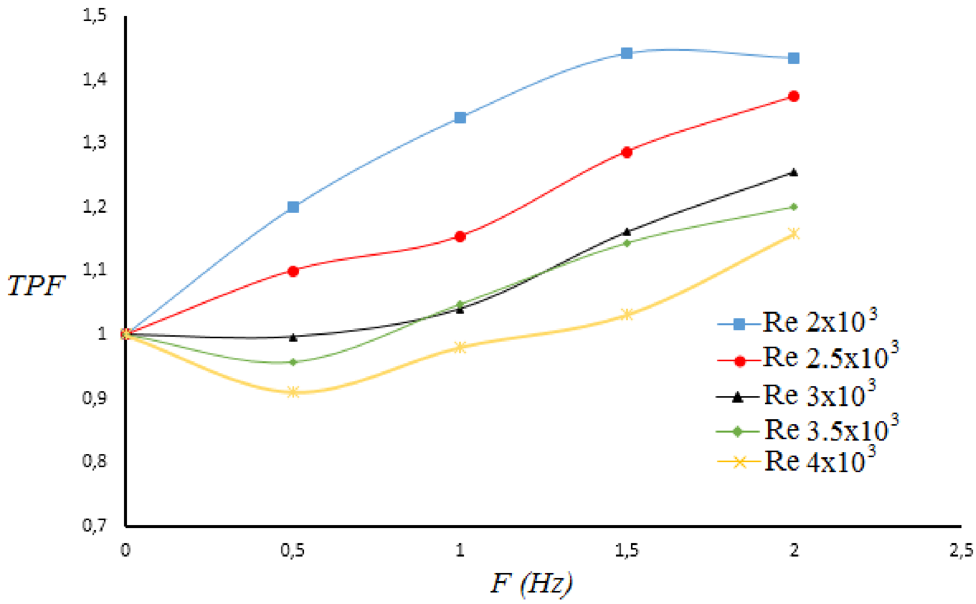

Figure 4.49. Effect of pulsation frequency on TPF between Re $2x10^3$ and $4x10^3$.

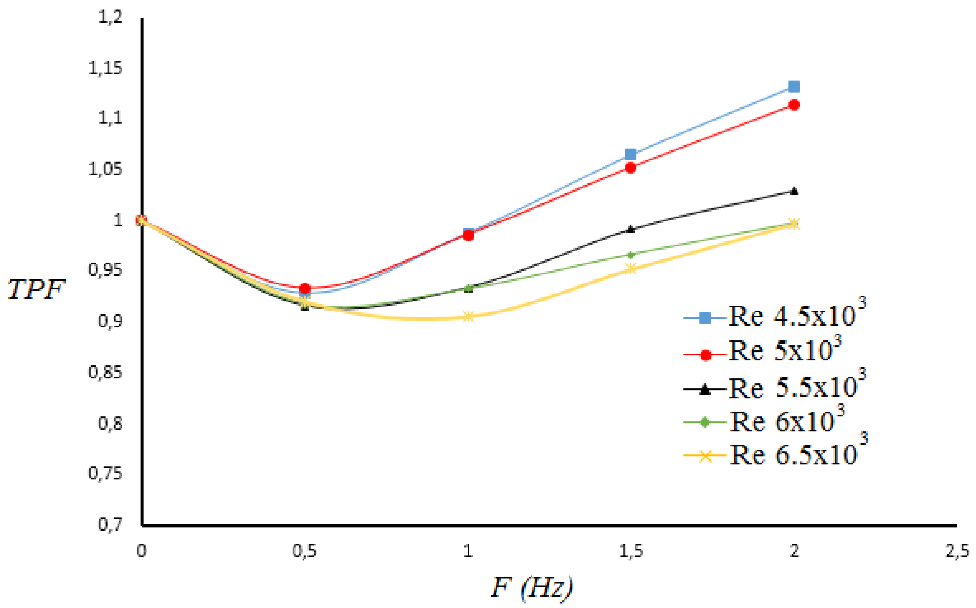

Figure 4.50. Effect of pulsation frequency on TPF between Re $4.5x10^3$ and $6.5x10^3$.

Heat transfer enhancement, *E* of pulsating flow at different wall shifting positions are demonstrated in Figure 4.43 for low, medium and high Reynolds numbers. Similar to a steady flow, shifting the corrugated bottom wall does not cause a significant change in heat transfer. The trend of the heat transfer enhancement, *E* curves is similar to each other for all wall configurations. As it is mentioned in Figure 4.35, the configuration, which is the bottom wall shifted as L/4, gives results in favor of increasing turbulence fluctuations. Therefore this configuration provides better heat transfer enhancement than others. Nevertheless, its heat transfer enhancement value is 3% better than no shifted wall case at most.

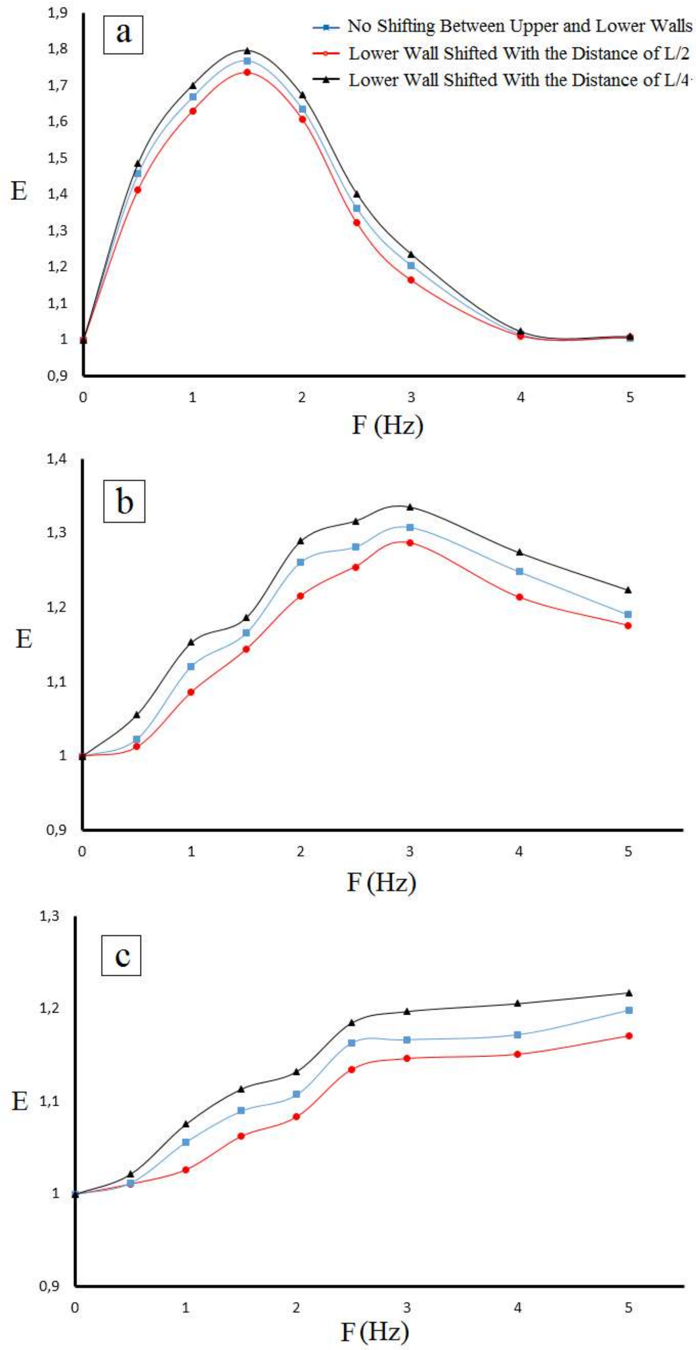

Figure 4.51. Heat transfer enhancemet with pulsating flow at different shifted wall configurations for a)Re = $2x10^3$, b) Re = $4x10^3$ and c) $6x10^3$.

5. CONCLUSION

Heat transfer and hydrodynamics of steady and pulsating flow passing through a channel with rectangular grooves placed on the top and bottom walls are investigated in the present work. The hydrodynamic factors underlying the heat transfer and pressure drop results obtained in the experiments are revealed using the Particle Image Velocimetry (PIV) method.

Steady flow experiments are performed to show the heat transfer enhancement capability of the grooved channel. The grooved channel provides 2.67 times better heat transfer than the straight channel at Re = $3x10^3$. This value corresponds to the highest heat transfer enhancement provided by the grooved channel. The enhancement reduces as the Reynolds number, *Re,* increases, and the lowest enhancement in heat transfer is detected at Re = $6.5x10^3$, which is 1.9 times greater than the straight channel. Heat transfer enhancement by using a grooved channel is not a cost-free process. Use of grooved channel instead of straight one cause 2.8-3.2 times increase in the friction factor, *f* depending on the Reynolds number. Since the grooved channel creates pressure loss along with the heat transfer increase, the net energy gain of the system needs to be evaluated. This evaluation is performed by calculating the Thermal Performance Factor, *TPF*. *TPF* is greater than unity for all investigated cases in the study, which indicates despite the increase in pressure loss net energy gain is positive. The maximum detected *TPF* value is 1.75.

A hydrodynamic investigation employing the PIV method shows that grooves disturb the flow and increase the mixing process by enhancing the turbulence fluctuations. Reynolds stress contours are plotted to show areas where fluctuations are concentrated. High Reynolds stress levels are observed at the separated shears layer over grooves. However, their spread is very limited to the other regions like the central axis or area inside the groove for low Reynolds numbers, *Re*. As the Reynolds number, *Re,* increases, the magnitude of the

Reynolds stress levels in the channel increases. Moreover, turbulence fluctuations spread to a larger area, especially the region inside the groove. The main reason for the increase of Reynolds stress inside the groove is the enhancement of interaction between energetic wake flow occupied groove space and mainstream. These phenomena are revealed by using the ability of the PIV method to get instantaneous flow data. Instantaneous flow structures showed that the secondary flow region inside the grooves behaves stable, and no massive flow motions occur between groove and mainstream for low Reynolds numbers. However, when the Reynolds number increased size and the location of the circulating flow region inside the groove dynamically changes due to flow moves in and out. An increase of wake flow of groove and mainstream interaction enhances turbulence mixing and also constantly refreshes the flow inside the groove space which means an increase of the heat transfer at these locations.

An additional study is carried out for a steady flow case that investigates the groove aspect ratio on heat transfer and pressure drop. Numerical simulations are performed for this investigation. Six different groove aspect ratios, n are tested and it is seen that $n = 0.2$ provides the best heat transfer but also the highest friction factor for all Reynolds numbers. Nevertheless, its *TPF* is highest among other groove aspect ratios.

Pulsating flow remarkably augments the heat transfer capability of the grooved channel. However, the enhancement ability of the pulsating flow strongly depends on its frequency and the value of the Reynolds number. The highest heat transfer enhancement is detected at Re = $2x10^3$ and pulsation frequency of 1.5 Hz. For these conditions heat transfer is 1.77 times greater than the steady flow cases. The value of the frequency that best heat transfer enhancement occurs is not fixed, but it changes with the Reynolds number. As the Reynolds number increases, pulsation frequency which provides the highest enhancement, also increases. Moreover, amount of the enhancement in heat transfer reduces for higher Reynolds numbers. The most heat transfer increase in Reynolds $6x10^3$ is 1.13 times higher than the steady flow. Pressure drop results do not show consistent variation with respect to pulsation frequency. Friction factor increases between 0-1.5 Hz it reduces 1.5-3 Hz and then again increases for higher frequencies. Since the pressure transmitter used in this study has a slow response time, reliable pressure data couldn't be taken for high frequencies of pulsating flow conditions.

Flow visualization experiments performed under pulsating flow conditions show that this type of flow further increases groove-mainstream interactions. Periodic variation in the flow velocity creates phases that facilitate flow transfer from the wake flow of grooves to the mainstream and vice versa. It is observed that the high velocity phase of pulsation is more suitable for flow enters the groove and low velocity phase of the pulsation provides convenient conditions for rejoining the flow inside the groove to the mainstream. When these phases successively follow each other, favorable conditions for heat transfer are created. However, an increase in the pulsating frequency, F does not always support this phenomenon. For higher frequencies, each phase of the pulsation lasts shorter, and therefore the effectiveness of the flow transfer is lessened. Variation of the vortical flow fluctuations through the pulsation period is demonstrated by analyzing the phase averaged Reynolds stress contours in low, medium (acceleration), and peak velocity phases. The highest Reynolds stress levels are observed in the low velocity phase of the pulsation. The reason for this situation is the disintegration of the coherent vortices into the flow in the low velocity phase. When the acceleration of the flow begins, areas with the high Reynolds stresses get smaller, and at the peak velocity phase, high Reynolds stress values are only seen in a limited region at the separated shear layers over the grooves. The representations of the $\overline{u'_{rms}}$ and $\overline{v'_{rms}}$ contours in the same pulsation phases showed that the variation in time and distribution in the channel of the fluctuation components of two directions are quite different from each other. High and medium $\overline{u'_{rms}}$ levels are mostly seen in shear layers, the area they cover, and their intensity do not vary significantly during the pulsation period. However, $\overline{v'_{rms}}$ levels with high and medium intensity are seen in a larger region including grooves and the area between grooves, in low velocity phase. Unlike $\overline{u'_{rms}}$, the intensity of $\overline{v'_{rms}}$ reduces dramatically in higher velocity phases of the pulsation.

Pulsating flow enhances turbulence mixing and groove-mainstream interaction. In low Reynolds numbers, Re, self-oscillations of the flow can not cause enough mixing, and fluid transfer between wake flow of grooves and mainstream is poor; therefore, the perturbation of the flow by pulsation creates the more pronounced effect. This is manifested in the results as better heat transfer enhancement at low Reynolds numbers.

Three different grooved channel configurations are created by shifting the bottom grooved wall at the distance of L/2 and L/4. By shifting the wall the affect of the groove positions with respect to each other located the opposite walls are investigated. It is seen that each groove behaves individually i.e. disturbance of the flow by the groove does not effect the other groove on opposite wall. However, a slight increase is observed in Reynolds stress levels for wall shifting as L/4. Since the wall shifting has a limited effect on flow, no substantial difference is obtained in heat transfer results neither for steady nor pulsating flow conditions.

REFERENCES

Adachi, T., and Uehara, H., 2001. Correlation between heat transfer and pressure drop in channels with periodically grooved parts, Int. J. Heat Mass Transf., 44: 4333–4343.

Ahmed, H.E., and Ahmed, M.I., 2015. Optimum thermal design of triangular, trapezoidal and rectangular grooved microchannel heat sinks, Int. Commun. Heat Mass Transf., 66: 47–57.

Ahmed, M.A., Shuaib, N.H., and Yusoff, M.Z., 2012. Numerical investigations on the heat transfer enhancement in a wavy channel using nanofluid, Int. J. Heat Mass Transf., 55: 5891–5898.

Ahn, J., Choi, H., Lee, and J.S., 2005. Large eddy simulation of flow and heat transfer in a channel roughened by square or semicircle ribs, J. Turbomach., 127: 263–269.

Ajeel, R.K., Salim, W.S.I.W., and Hasnan, K., 2019. Design characteristics of symmetrical semicircle-corrugated channel on heat transfer enhancement with nanofluid, Int. J. Mech. Sci., 151: 236–250.

Akbarzadeh, M., Rashidi, S., and Esfahani, J.A., 2017. Influences of corrugation profiles on entropy generation, heat transfer, pressure drop, and performance in a wavy channel, Appl. Therm. Eng., 116: 278–291.

Akdag, U., Akcay, S., and Demiral, D., 2014. Heat transfer enhancement with laminar pulsating nanofluid flow in a wavy channel. International Communications in Heat and Mass Transfer, 59: 17-23.

Bell, J.H., and Mehta, R.D., 1988. Contraction Design for Small Low-Speed Wind Tunnels.

Benim, A.C., Chattopadhyay, H., and Nahavandi, A., 2011. Computational analysis of turbulent forced convection in a channel with a triangular prism. International Journal of Thermal Sciences, 50.10: 1973-1983.

Blythman, R., Persoons, T., Jeffers, N., and Murray, D.B.; 2019. Heat transfer of laminar pulsating flow in a rectangular channel. International Journal of Heat and Mass Transfer, 128: 279-289.

Chang, K., Constantinescu, G., and Park, S.O., 2006. Analysis of the flow and mass transfer processes for the incompressible flow past an open cavity with a laminar and a fully turbulent incoming boundary layer, J. Fluid Mech., 561: 113–145.

Choi, E.Y., Choi, Y.D., Lee, W.S., Chung, J.T., and Kwak, J.S., 2013. Heat transfer augmentation using a rib-dimple compound cooling technique, Appl. Therm. Eng., 51: 435–441.

Choi, H.S., and Suzuki, K., 2005. Large eddy simulation of turbulent flow and heat transfer in a channel with one wavy wall, Int. J. Heat Fluid Flow., 26: 681–694.

Cho, H.W., and Hyun, J.M. 1990. Numerical solutions of pulsating flow and heat transfer characteristics in a pipe. International Journal of Heat and Fluid Flow, 11(4): 321-330.

Chattopadhyay, H., Durst, F., and Ray, S., 2006. Analysis of heat transfer in simultaneously developing pulsating laminar flow in a pipe with constant wall temperature. International communications in heat and mass transfer, 33(4): 475-481.

Davletshin, I.A., Mikheev, A.N., Mikheev, N.I., and Shakirov, R.R. 2020. Heat transfer and structure of pulsating flow behind a rib. International Journal of Heat and Mass Transfer, 160: 120173.

Ebrahimi-Moghadam, A., and Moghadam, A.J., 2019. Optimal design of geometrical parameters and flow characteristics for Al2O3/water nanofluid inside corrugated heat exchangers by using entropy generation minimization and genetic algorithm methods, Appl. Therm. Eng., 149: 889–898.

Eiamsa-ard, S., and Promvonge, P., 2008. Numerical Study on Heat Transfer of Turbulent Channel Flow over Periodic Grooves, Int. Commun. Heat Mass Transf., 35: 844–852.

Eiamsa-ard, S., and Promvonge, P., 2009. Thermal characteristics of turbulent rib-grooved channel flows, Int. Commun. Heat Mass Transf., 36: 705–711.

Eiamsa-Ard, S., and Changcharoen, W., 2011. Analysis of turbulent heat transfer and fluid flow in channels with various ribbed internal surfaces, J. Therm. Sci., 20: 260–267.

Elshafei, E.A., Mohamed, M.S., Mansour, H., and Sakr, M., 2008. Experimental study of heat transfer in pulsating turbulent flow in a pipe. International Journal of Heat and Fluid Flow, 29(4): 1029-1038.

Faghri, M., Javdani, K., and Faghri, A., 1979. Heat transfer with laminar pulsating flow in a pipe. Letters in Heat and Mass Transfer, 6(4): 259-270.

Farzad, B. T., Karami, M., and M., Jahromi. 2011. Unsteady flow and heat transfer analysis of an impinging synthetic jet. Heat and mass transfer, 47.11: 1363-1373.

Gbadebo, S.A., Said, S.A.M., and Habib, M.A. 1999. Average Nusselt number correlation in the thermal entrance region of steady and pulsating turbulent pipe flows. Heat and mass transfer, 35(5): 377-381.

Ghaddar, N.K., Magen, M., Mikic, B. B., and Patera, A.T., 1986. Numerical investigation of incompressible flow in grooved channels. Part 2. Resonance and oscillatory heat-transfer enhancement, Journal of Fluid Mechanics, 168: 541-567.

Ghaddar, N., and El-Hajj, A., 2000. Numerical study of heat transfer augmentation of viscous flow in corrugated channels, Heat Transf. Eng., 21: 35–46.

Gosselin, L., and Da Silva, A. K., 2004. Combined Heat Transfer andPower Dissipation Optimization of Nanofluid Flows,AppliedPhysics Letters,vol. 85, no. 18, pp. 4160–4162.

Greiner, M., 1991. An experimental investigation of resonant heat transfer enhancement in grooved channels. International journal of heat and mass transfer, 34(6): 1383-1391.

Greiner, M., Spencer, G., and Fischer, P.F., 1996. Direct numerical simulation of three-dimensional flow and augmented heat transfer in a grooved channel, Am. Soc. Mech. Eng. Heat Transf. Div. HTD, 330: 125–131.

Guzmán, A.M., Cárdenas, M.J., Urzúa, F.A., and Araya, P.E., 2009. Heat transfer enhancement by flow bifurcations in asymmetric wavy wall channels, Int. J. Heat Mass Transf.; 52: 3778–3789.

Habib, M.A., Ul-Haq, I., Badr, H.M., and Said, S.A.M. 1998. Calculation of turbulent flow andheat transfer in periodicallyconverging–diverging channels. Computers & fluids, 27: 95-120.

Habib, M.A., Said, S.A.M., Al-Farayedhi, A.A., Al-Dini, S.A., Asghar, A., and Gbadebo, S.A. 1999. Heat transfer characteristics of pulsated turbulent pipe flow. Heat and mass transfer, 34(5): 413-421.

Han, J.C., 1988. Heat Transfer and Friction Characteristics in Rectangular Channels With Rib Turbulators, J. Heat Transfer., 110: 321–328.

Harikrishnan, S., and Tiwari, S., 2018. Effect of skewness on flow and heat transfer characteristics of a wavy channel, Int. J. Heat Mass Transf., 120: 956–969.

Hemida, H.N., Sabry, M.N., Abdel-Rahim, A., and Mansour, H. 2002. Theoretical analysis of heat transfer in laminar pulsating flow. International journal of heat and mass transfer, 45(8): 1767-1780.

Herman, C., and Kang, E., 2002 Heat transfer enhancement in a grooved channel with curved vanes, Int. J. Heat Mass Transf., 45: 3741–3757.

International Energy Agency, 2020. World gross electricity production, by source, 2018,https://www.iea.org/data-and-statistics/charts/world-gross-electricity-production-by-source-2018, (last accessed in October,2020).

Ji, T.H., Kim, S.Y., and Hyun, J.M., 2008. Experiments on heat transfer enhancement from a heated square cylinder in a pulsating channel flow. International Journal of Heat and Mass Transfer, 51(5-6): 1130-1138.

Jin, D.X., Lee, Y.P., & Lee, D.Y., 2007. Effects of the pulsating flow agitation on the heat transfer in a triangular grooved channel. International journal of heat and mass transfer, 50(15-16): 3062-3071.

Kamali, R., and Binesh, A.R., 2008. The importance of rib shape effects on the local heat transfer and flow friction characteristics of square ducts with ribbed internal surfaces, Int. Commun. Heat Mass Transf., 35: 1032–1040.

Khosravi-Bizhaem, H., Abbassi, A., and Ravan, A.Z.; 2019. Heat transfer enhancement and pressure drop by pulsating flow through helically coiled tube: an experimental study. Applied Thermal Engineering, 160: 114012.

Kim, S.Y., Kang, B.H., and Hyun, J.M., 1993. Heat transfer in the thermally developing region of a pulsating channel flow. International journal of heat and mass transfer, 36(17): 4257-4266.

Kim, S.Y., Kang, B.H., and Hyun, J.M., 1998. Forced convection heat transfer from two heated blocks in pulsating channel flow. International Journal of Heat and Mass Transfer, 41(3): 625-634.

Kurtulmuş, N., Zontul, H., and Sahin, B., 2020. Heat transfer and flow characteristics in a sinusoidally curved converging-diverging channel, Int. J. Therm. Sci., 148.

Krishnan, K.N., and Sastri, V.M.K., 1982. Pulsating flows in heat exchangers—an experimental study. Wärme-und Stoffübertragung, 16(3): 169-173.

Labbe, O., and Le, T.H., 1970. Numerical simulation of flow in a ribbed channel. WIT Transactions on Engineering Sciences, 12.

Lai, Y.G., Iyer, R.S., Kakac, S., and Fung, K.-Y., 1997. Instability and heat transfer in grooved channel flow, J. Thermophys. Heat Transf., 11: 437–445.

Launder, B. E., and Spalding, D. B., 1974. The Numerical Computation of Turbulent Flows, Computer Methods in Applied Mechanics an d Engineering, 3: 269- 289.

Liou, T.M., Hwang, J.J., Chen, and S.H., 1992. Turbulent transport phenomena in a channel with periodic rib turbulators, J. Thermophys. Heat Transf., 6: 513–521.

Liang, C., and George P., 2005. Study of the effect of flow pulsation on the flow field and heat transfer over an inline cylinder array using LES. Engineering Turbulence Modelling and Experiments 6. Elsevier Science BV: 813-822.

Liu, J., Xie, G., and Simon, T.W., 2015. Turbulent flow and heat transfer enhancement in rectangular channels with novel cylindrical grooves, Int. J. Heat Mass Transf., 81: 563–577.

Lorenz, S., Mukomilow, D., and Leiner, W., 1995. Distribution of the heat transfer coefficient in a channel with periodic transverse grooves, Exp. Therm. Fluid Sci., 11: 234–242.

Mackley, M.R., and Stonestreet, P., 1995. Heat transfer and associated energy dissipation for oscillatory flow in baffled tubes. Chemical Engineering Science, 50(14): 2211-2224.

Mehta, B., and Khandekar, S., 2015. Local experimental heat transfer of single-phase pulsating laminar flow in a square mini-channel. International Journal of Thermal Sciences, 91: 157-166.

Mehta, S.K., and Pati, S., 2019. Analysis of thermo-hydraulic performance and entropy generation characteristics for laminar flow through triangular corrugated channel, J. Therm. Anal. Calorim. 136: 49–62.

Mikheev, N.I., Molochnikov, V.M., Mikheev, A.N., and Dushina, O.A., 2017. Hydrodynamics and heat transfer of pulsating flow around a cylinder. International Journal of Heat and Mass Transfer, 109: 254-265.

Mohammed, H.A., Al-Shamani, A.N., and Sheriff, J.M., 2012. Thermal and hydraulic characteristics of turbulent nanofluids flow in a rib-groove channel, Int. Commun. Heat Mass Transf., 39: 1584–1594.

Moon, J.W., Kim, S.Y., and Cho, H.H., 2005. Frequency-dependent heat transfer enhancement from rectangular heated block array in a pulsating channel flow. International journal of heat and mass transfer, 48(23-24): 4904-4913.

Moschandreou, T., and Zamir, M., 1997. Heat transfer in a tube with pulsating flow and constant heat flux. International journal of heat and mass transfer, 40(10): 2461-2466.

Molochnikov, V.M., Mikheev, A.N., Aslaev, A.K., Dushina, O.A., and Paereliy, A.A.; 2019. Heat transfer of a tube bundle in a pulsating flow. Thermophysics and Aeromechanics, 26(4): 547-559.

Nassar, M.S., Hegazi, A.A., and Mousa, M.G.; 2019. Combined effect of pulsating flow and magnetic field on thermoelectric cooler performance. Case Studies in Thermal Engineering, 13: 100403.

Naphon, P., and Wiriyasart, S., 2018. Pulsating flow and magnetic field effects on the convective heat transfer of TiO2-water nanofluids in helically corrugated tube. International Journal of Heat and Mass Transfer, 125: 1054-1060.

Nedyalkov, I., 2012. Design of Contraction , Test Section , and Diffuser for a High-Speed Water Tunnel.

Nigen, J.S., and Amon, C.H., 1994. Time-dependent conjugate heat transfer characteristics of self-sustained oscillatory flows in a grooved channel, J. Fluids Eng. Trans. ASME., 116: 499–507.

Olayiwola, B., and Walzel, P., 2008. Cross-flow transport and heat transfer enhancement in laminar pulsed flow. Chemical Engineering and Processing: Process Intensification, 47(5): 929-937.

Ozturk, N.A., Akkoca, A., and Sahin, B., 2008. PIV measurements of flow past a confined cylinder, Exp. Fluids., 44: 1001–1014.

Pan, J., Bian, Y., Liu, Y., Zhang, F., Yang, Y., and Arima, H. 2020. Characteristics of flow behavior and heat transfer in the grooved channel for pulsatile flow with a reverse flow. International Journal of Heat and Mass Transfer, 147: 118932.

Promthaisong, P., and Eiamsa-ard, S., 2019. Fully developed periodic and thermal performance evaluation of a solar air heater channel with wavy-triangular ribs placed on an absorber plate, Int. J. Therm. Sci., 140: 413–428.

Rabadi, N. J., Chow, J.C. F., and Simon, H.A., 1982. Heat transfer in curved tubes with pulsating flow. International Journal of Heat and Mass Transfer, 25(2): 195-203.

Rashidi, S., Akbarzadeh, M., Masoodi, R., and Languri, E.M., 2017. Thermal-hydraulic and entropy generation analysis for turbulent flow inside a corrugated channel, Int. J. Heat Mass Transf., 109: 812–823.

Ridouane, E.H., and Campo, A., 2007. Heat transfer and pressure drop characteristics of laminar air flows moving in a parallel-plate channel with transverse hemi-cylindrical cavities, Int. J. Heat Mass Transf., 50: 3913–3924.

Singh, V., Haridas, D., and Srivastava, A., 2019. Experimental study of heat transfer performance of compact wavy channel with nanofluids as the coolant medium: Real time non-intrusive measurements, Int. J. Therm. Sci., 145.

Selimefendigil, F., and Öztop, H.F., 2018. Role of magnetic field and surface corrugation on natural convection in a nanofluid filled 3D trapezoidal cavity, Int. Commun. Heat Mass Transf., 95: 182–196.

Stone, K., and Vanka, S.P., 1999. Numerical study of developing flow and heat transfer in a wavy passage, J. Fluids Eng. Trans. ASME, 121: 713–719.

Sun, F., Bian, Y., Arima, H., Ikegami, Y., and Xu, X., 2010. Strength characteristics of the self-sustained wave in grooved channels with different groove length, Heat Mass Transf. Und Stoffuebertragung, 46:1229–1237.

Sung, H.J., Hwang, K.S., and Hyun, J.M., 1994. Experimental study on mass transfer from a circular cylinder in pulsating flow. International journal of heat and mass transfer, 37(15): 2203-2210.

Tokgoz, N., Aksoy, M.M., and Sahin, B., 2017. Investigation of flow characteristics and heat transfer enhancement of corrugated duct geometries, Appl. Therm. Eng., 118: 518–530.

U.S. Energy Information Administration 2020. International Energy Outlook 2019 with projections to 2050,https://www.eia.gov/outlooks/ieo/pdf/ieo2019.pdf, (lastaccessed in April,2020).

Valencia, A., and Hinojosa, L., 1997. Numerical solutions of pulsating flow and heat transfer characteristics in a channel with a backward-facing step. Heat and mass transfer, 32(3): 143-148.

Valinataj-Bahnemiri, P., Ramiar, A., Manavi, S.A., and Mozaffari, A., 2015. Heat transfer optimization of two phase modeling of nanofluid in a sinusoidal wavy channel using Artificial Bee Colony technique, Eng. Sci. Technol. an Int. J., 18: 727–737.

Valueva, E. P., 2005. Hydrodynamics and heat transfer in pulsating turbulent pipe flow of a liquid of variable properties. High Temperature, 43(6): 890-899.

Vanaki, S.M., Mohammed, H.A., Abdollahi, A., and. Wahid, M.A., 2014. Effect of nanoparticle shapes on the heat transfer enhancement in a wavy channel with different phase shifts, J. Mol. Liq., 196: 32–42.

Velazquez, A., Arias, J.R., and Mendez, B., 2008. Laminar heat transfer enhancement downstream of a backward facing step by using a pulsating flow. International Journal of Heat and Mass Transfer, 51(7-8): 2075-2089.

Wang, X., and Zhang, N., 2005. Numerical analysis of heat transfer in pulsating turbulent flow in a pipe. International Journal of Heat and Mass Transfer, 48(19-20): 3957-3970.

Wantha, C., 2016. Effect and heat transfer correlations of finned tube heat exchanger under unsteady pulsating flows. International Journal of Heat and Mass Transfer, 99: 141-148.

Xu, C., Xu, S., Wei, S., and Chen, P., 2020. Experimental investigation of heat transfer for pulsating flow of GOPs-water nanofluid in a microchannel. International Communications in Heat and Mass Transfer, 110: 104403.

Yang, L.Li.M., and Zhang, Y., 2008. Numerical study of periodically fully-developed convection in channels with periodically grooved parts, Int. J. Heat Mass Transf., 51: 3057–3065.

Yang, Y.T., Wang, Y.H., and Tseng, P.K., 2014. Numerical optimization of heat transfer enhancement in a wavy channel using nanofluids, Int. Commun. Heat Mass Transf., 51: 9–17.

Yang, Y.T., Tang, H.W., Zeng, B.Y., and Wu, C.H., 2015. Numerical simulation and optimization of turbulent nanofluids in a three-dimensional rectangular rib-grooved channel, Int. Commun. Heat Mass Transf., 66: 71–79.

Zhu, X.W., Fu, Y.H., Zhao, J.Q., and Zhu, L., 2016. Three-dimensional numerical study of the laminar flow and heat transfer in a wavy-finned heat sink filled with Al2O3/ethylene glycol-water nanofluid, Numer. Heat Transf. Part A Appl., 69: 195–208.

Yang, B., Gao, T., Gong, J., and Li, J., 2018. Numerical investigation on flow and heat transfer of pulsating flow in various ribbed channels. Applied Thermal Engineering, 145: 576-589.

BIOGRAPHY

Harun ZONTUL graduated from Seyhan Ç.E.A.Ş. Anatolian High School. Then, he received his BSc and MSc degrees from the Mechanical Engineering Departments of Mersin University and Çukurova University respectively. He has been working as a research assistant at Çukurova University since 2014. He conducted researches about flow control methods, heat transfer enhancement techniques both numerically and experimentally.